Geochemistry of Camp Lake Zone, Lac des Iles Complex, Thunder Bay, N. Ontario

Beaumarchais Njipmo Ngoko

A thesis submitted in partial fulfillment of the requirements of the degree of Master of Science

Department of Geology

Lakehead University, Thunder Bay, Ontario

January 2026

Abstract

The Archean Lac des Iles suite is located just north of the Wabigoon-Quetico boundary, approximately 90 kilometers north of Thunder Bay in Northwestern Ontario. The suite includes discrete mafic and ultramafic complexes associated with sanukitoids, which were emplaced along deep-seated regional faults. Of these, only the Lac des Iles Complex hosts an economically significant palladium deposit at the Lac des Iles mine. The complex is divided into two parts: North Lac des Iles and South Lac des Iles. The North Lac des Iles mainly comprises ultramafic rocks such as websterite, clinopyroxenite, wehrlite, lherzolite, dunite, and peridotite. In contrast, the South Lac des Iles Complex is primarily composed of mafic rocks including gabbro, gabbronorite, norites, and melanorite and is the main host of the Roby, Offset, and Camp Lake zones which are the main economically important mineralized zones.

This study focused on the Camp Lake zone, the deepest part of the deposit, recently identified by exploration drilling. The host rocks of the Camp Lake mineralization primarily consist of gabbronorite and norite, exhibiting preserved cumulate textures with plagioclase and pyroxenes as the main primary phases. The pyroxenes predominantly comprise orthopyroxene with minor clinopyroxene, which are partially to completely replaced by amphiboles (chlorite, actinolite, and tremolite). The plagioclase is weakly to moderately altered by sericite and generally retains its original habit.

Magmatic sulfide contents in Camp Lake rocks have modal abundances from 0.5% to 3%, and are dominated by pyrrhotite, pentlandite, and chalcopyrite, with minor pyrite. Sulfide minerals often occur as blebs or disseminated grains intergrown with silicate minerals. Palladium enrichment is interpreted as magmatic, driven by sulfide saturation and high metal-silicate partitioning efficiency, with platinum group minerals (PGMs) hosted primarily in pentlandite and chalcopyrite. A new zircon U-Pb age was acquired for the mineralized Camp Lake rocks, yielding an emplacement age of 2690.56 ± 0.80 Ma, similar to that of the Roby and Offset deposits. Geochemical signatures, including depleted incompatible elements and positive εNd values, support a mantle-derived origin with minor crustal input. The Camp Lake Zone rocks are enriched in LREE (La/Sm_n ranging from 1.29 to 7.75, with a median of 2.90), have unfractionated HREE (Gd/Yb_n ranging from 0.56 to 1.49, with a median of 0.82), and negative Nb anomalies. These

values are similar to those of the Roby and Offset zones and are consistent with a subduction zone setting. Similar to the Roby-Offset deposits, PGE values in Camp Lake range between 1.0 g/t and 3.0 g/t, increasing with Cu and Ni content. However, Camp Lake is distinguished by higher proportions of pyrrhotite compared to chalcopyrite and lower Pd/Pt and Cu/Pd ratios than the other zones.

The Camp Lake Zone has low $\delta^{34}S$ values, ranging from (-1.1‰ to +0.3‰), whereas the Roby and Offset zones show wider variations ranging from (-0.37 to +3.28‰). This suggests that the sulfur in the Camp Lake Zone is of mantle origin. Sm–Nd isotopic compositions (εNd = +0.30 to +1.12) for the Camp Lake Zone is also slightly more positive than the Roby and Offset zones (εNd = -4.1 to 0.384). Overall, when compared with the more contaminated Roby-Offset zones, Camp Lake represents a transitional domain with greater geochemical uniformity, suggesting a continuum of magmatic processes and metallogenic evolution within the Lac des Iles Intrusive Complex.

Acknowledgements

I would like to express my deep gratitude to my research supervisor, Peter Hollings, for his patience, insightful guidance, and unwavering support throughout this project. His encouragement, constructive feedback, and commitment to helping me achieve my goals have been invaluable. I am sincerely thankful.

I warmly thank Dr. Lionnel Djon and Impala Canada for designing and funding this research project. I am also grateful to Dr. Djon and the entire team at the Lac des Iles mine for granting me access to the site, drill cores, pulps, and rejects all essential for the completion of this study.

A heartfelt thank you to Kristi Tavener and Dr. Jonas Valiunas for preparing the excellent thin sections, and to Dr. James Tolley for his guidance in preparing my isotopic samples and for his critical feedback, which helped strengthen the coherence of my argument.

This research was made possible through the financial support of Lakehead University, Impala Canada, and an Alliance grant from the Natural Sciences and Engineering Research Council of Canada (NSERC).

I would like to thank all the professors and students in the Department of Geology at Lakehead University for creating such a stimulating environment for learning and research. I am especially grateful to the wonderful friends I've made in the department and for their spontaneous participation in passionate geological discussions and much-needed moments of relaxation. A special thank you to Michael Nwakanma you're amazing.

Finally, I extend my heartfelt thanks to my family for their unwavering support. Leaving my loved ones to embark on this new chapter of my life was not easy, but their presence even from afar accompanied me throughout this journey. Without their support, I would never have been able to start this project, let alone bring it to completion.

Table of contents

List of figures

List of Tables

Chapter 1 - Introduction

Magmatic Ni–Cu–PGE sulfide deposits represent one of the most important sources of critical base and precious metals globally (Naldrett, 1999; Barnes et al., 1997; Lesher, 2019). These systems form when mafic to ultramafic magmas become saturated in sulfur, leading to the segregation of an immiscible sulfide liquid that preferentially incorporates chalcophile and highly siderophile elements from the silicate melt (Barnes et al., 1997; Lambert et al., 1998; Naldrett, 1999). The genesis of such deposits typically involves four key stages: generation of a metal-bearing magma, attainment of sulfide saturation, subsequent metal enrichment through melt–sulfide interaction, and crucially, the trapping and accumulation of sulfides to form economically significant concentrations in the upper crust.

Metal-bearing magmas are generally derived from high degrees of partial melting in the mantle and are emplaced in tectonic settings conducive to large-scale mafic magmatism, such as intracontinental rifts, mantle plumes, or continental arcs (Lambert et al., 1998; Barnes et al., 2005; Lesher, 2019). These magmas contain Ni, Cu, and PGE, but these elements remain dissolved in the silicate melt until a sulfide phase is introduced. Sulfide saturation occurs when the magma assimilates sulfur-rich crustal material or undergoes internal degassing, releasing volatile sulfur species such as H_2S or SO_2 during ascent and decompression (Ripley et al., 2002; Naldrett, 2004). In reduced magmatic settings, once sulfur solubility is exceeded, a dense sulfide liquid can separate from the melt, initiating metal partitioning. In more oxidized systems, however, sulfur may reside predominantly in the sulfate field, preventing sulfide liquid formation unless subsequent reduction processes occur. This interplay between oxidation state and sulfur speciation is critical, as illustrated at Norilsk, where sulfate-derived sulfur was reduced in coal-rich horizons to generate sulfide liquids capable of hosting metals.

The efficiency of metal transfer into the sulfide phase is governed by the R factor, which quantifies the mass of silicate melt equilibrated with a given mass of sulfide liquid (Lesher and Barnes, 2009; Lambert et al., 1998). High R values ($R > 10D$, where D is the partition coefficient) promote significant metal enrichment, explaining why some deposits are low in sulfide yet rich in PGE, whereas others are dominated by Ni-Cu (Barnes and Lightfoot, 2005; Naldrett, 2010).

Upon cooling, the sulfide liquid migrates into structural and stratigraphic traps, such as magma conduits, zones of flow deceleration, bedding planes, or cumulate horizons, where it crystallizes in a predictable sequence (Naldrett, 2004; Holwell and McDonald, 2010). Monosulfide solid solution (MSS) forms first, incorporating Ni and compatible PGE (Os, Ir, Ru), followed by intermediate solid solution (ISS), which concentrates Cu, Pd, Pt, and Au (Cabri, 2002; Holwell and McDonald, 2010). Further cooling leads to the recrystallization of MSS into pyrrhotite and pentlandite, and ISS into chalcopyrite. Residual sulfide liquid may also precipitate discrete PGE minerals such as sperrylite ($PtAs_2$), moncheite ($PtTe_2$), and michenerite (PdBiTe) (Cabri, 2002; Holwell and McDonald, 2010; Dare et al., 2010). These mineral assemblages reflect the internal evolution of the sulfide liquid, but they do not control the geometry of the resulting ore bodies. Instead, the physical behaviour of the sulfide melt and its interaction with magmatic plumbing systems give rise to a wide range of deposit types, including discordant pods, feeder-related lenses, and stratiform layers within layered intrusions (Barnes et al., 2005; Naldrett, 2010). More recent studies have emphasized the complex behavior of sulfides and metals during sulfide fractionation, including isotope fractionation processes and intracrustal differentiation. For example, copper isotope evidence highlights the role of sulfide segregation in continental crust formation (Liu et al., 2023), Pd fractionation has been constrained in sulfide-bearing intrusions (Wei et al., 2023), and experimental work has documented Ru isotope fractionation between metal, silicate, and sulfide melts (Grützner et al., 2021). These advances underscore that sulfide fractionation not only controls deposit morphology but also governs the distribution and isotopic signatures of chalcophile elements in magmatic systems.

A distinct subset of these deposits is characterized by low sulfide content and high concentrations of Pd and Pt. Classic examples include the Merensky Reef of the Bushveld Complex in South Africa, the J-M Reef of the Stillwater Complex in Montana, USA, and the Great Dyke in Zimbabwe. These PGE-dominant systems commonly occur as reef-like or stratiform horizons within differentiated intrusions, though their architecture and geochemical signature are strongly influenced by tectonic regime, magma evolution, and post-magmatic processes (Maier et al., 2007; Naldrett, 2010).

One of Canada's most prominent examples of these PGE rich deposits is the Lac des Iles Complex (LDIC), located ~85 km north of Thunder Bay, Ontario. The LDIC is hosted within mafic to

ultramafic rocks intruded into tonalitic crust near the boundary between the Wabigoon and Quetico subprovinces (Barnes and Gomwe, 2011). Since the onset of mining in 1993, over 4 Moz of Pd have been extracted from ~70 Mt of ore at an average grade of 2.3 g/t Pd (Implats, 2022). By 2024, total reserves and resources reached 5.8 Moz 3E (Pd + Pt + Au) at 2.60 g/t, including 0.6 Moz attributed to the emerging Camp Lake Zone (Implats, 2025).

The LDIC is a polyphase Neoarchean intrusion, dated at 2.7 Ga (Stone et al., 2003), comprising the North Lac Des Iles and the South Lac Des Iles complex Complex (SLDIC). While the northern portion includes more ultramafic stratified sequences, the southern complex is dominated by mafic lithologies. The SLDIC is subdivided into four lithological domains: gabbronorite, breccia, norite, and diorite, with the breccia–gabbronorite and breccia–norite contacts hosting the bulk of the economic mineralization (<5% sulfide; Decharte et al., 2018). Historic mining has been concentrated in the Roby and Offset Zones of the SLDIC, separated by the Offset Fault, whereas the Camp Lake Zone, located farther south and at greater depth, represents the newest exploration target.

Mineralization within the SLDIC is typified by steep geometries, low sulfide content, and strong association with magmatic brecciation. These zones are notably enriched in Pd and exhibit variable Cu/Pd and S/Se ratios, reflecting spatially heterogeneous magmatic and post-magmatic processes (Djon et al., 2018; Holwell et al., 2017). Many Archean Ni–Cu–PGE deposits are linked to plume-related magmatism in rift settings, such as the Norilsk–Talnakh deposits in Siberia, the Raglan deposits in the Cape Smith Belt of Quebec, and the Voisey's Bay intrusion in Labrador. In contrast, the LDIC has been interpreted as a product of continental arc magmatism (Brügmann et al., 1997; Hinchey et al., 2005; Barnes and Gomwe, 2011), although alternative models have suggested hybrid or plume-related origins.

The Camp Lake Zone, located at the southernmost extent of the SLDIC and at greater depth than Roby and Offset, provides an ideal setting to investigate the interplay between magmatic evolution, crustal contamination, and sulfide saturation. Its lithologies are broadly similar to those of the Roby and Offset Zones, but its deeper position and limited prior study make it particularly valuable for testing whether the metallogenic processes identified in the upper parts of the complex persist at depth. In this sense, Camp Lake offers a complementary perspective rather

than a distinct mineralogical signature, and its underexplored status highlights its importance as both a scientific target and a potential future exploration focus within the district. This thesis investigated the geology, petrology and geochemistry to provide a comprehensive overview of the Camp Lake intrusion. Key objectives included:

- Describing the mineralogical and textural features of Camp Lake rocks, distinguishing between primary and alteration-related assemblages;
- Interpreting major, trace, and isotopic geochemistry to infer magma origin, contamination processes, and compare with the Roby and Offset zones;
- Investigating sulfide saturation and Pd enrichment mechanisms, and assessing their implications for the broader metallogenic framework of the SLDIC.

Chapter 2 - Regional Geology

2.1 Superior Province

The Superior Province of Canada, located in northeastern North America, covers an area of over 1 572 000 km^2 (Fig. 2.1). and comprises most of eastern Canada, including parts of the provinces of Quebec, Ontario, and Manitoba, as well as parts of the northeastern United States (Thurston, 1991). The Superior Province is bordered by Paleoproterozoic orogenies to the north, west, and east (notably by the Churchill Province), and by the Southern Province to the south. At its southeastern edge, it is bounded by a Mesoproterozoic orogeny, the Grenville Province (Card and Ciesielski, 1986). Composed mainly of terranes organized into east-west trending belts, the Superior Province includes a variety of geological blocks, including granite-gneiss complexes, metasedimentary formations, and plutonic terranes. These geological structures reflect the complex history of continental accretion that occurred during the Kenoran orogeny, between 2.72-2.68 Ga (Card, 1990; Percival et al., 2006).

The Superior Province was originally divided into geological subprovinces based on lithological, geophysical, and structural data and geochronology (Goodwin, 1978; Thurston et al., 1991). In recent years, researchers have focused their studies on a classification system oriented towards subdivisions based in part on historical subprovince boundaries but also using more precise geochronology and contemporary interpretations of the structure and geophysical characteristics (Percival, 2007; Stott et al., 2010). A revised map of the Superior Province has been developed by Stott et al. (2010), which highlights the tectonic assemblages, domains, terranes, and superterranes (Fig. 2.1).

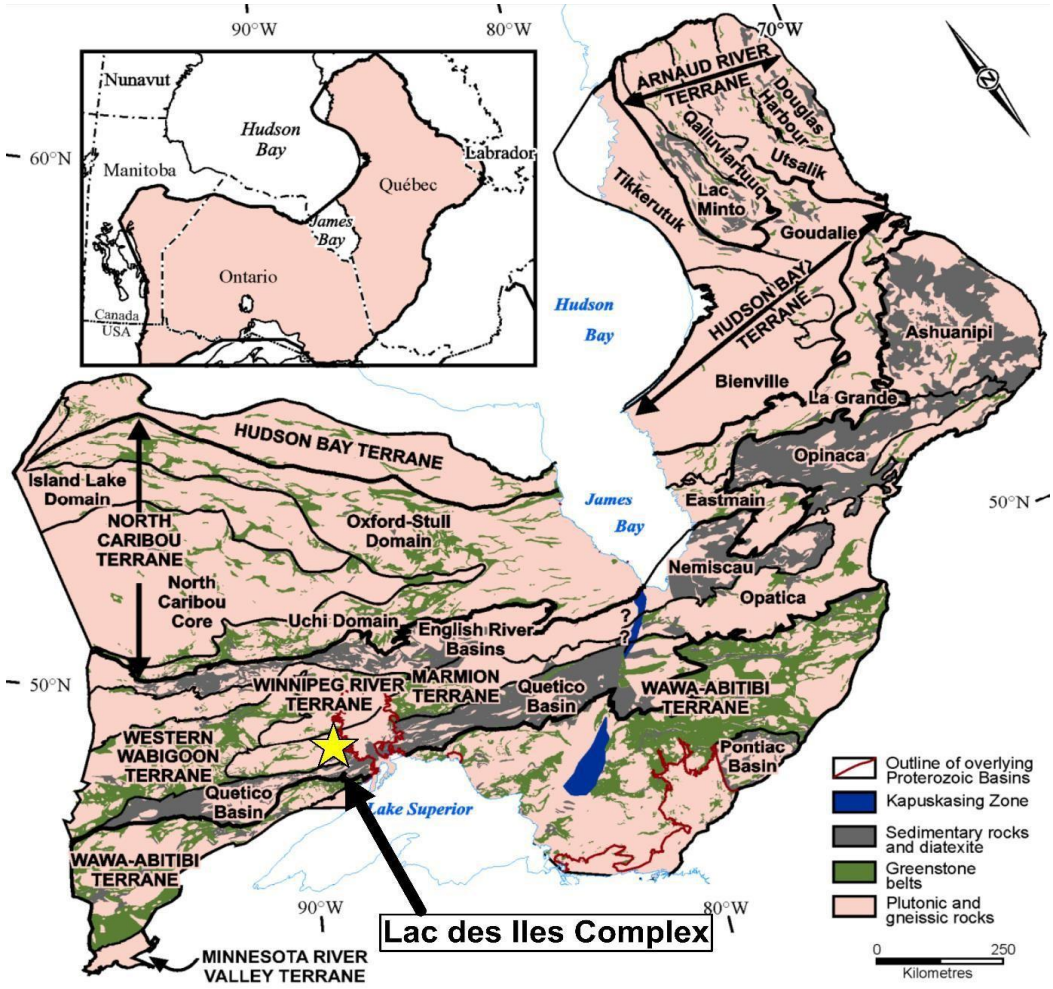

Figure 2.1 – Terrane map of the Superior Province showing the location of the Lac des Iles complex (modified from Stott et al., 2010).

A terrane is a tectonic region with distinct internal characteristics compared to its neighboring areas, as outlined by Stott et al. (2010). Conversely, a lithologically younger domain, is characterized by a clearly different composition, possessing younger crust or sharing a common geological base with a terrane, whereas a superterrane is a collection of several terranes that share a common accretion history and form a larger-scale geological block.

The subprovinces of the Superior Province have been defined and studied by several researchers. Those defined by Card and Ciesielski (1986) are still largely recognizable in the system developed by Stott et al. (2010). These include metasedimentary basins such as the Quetico and Opinaca, which are mainly composed of greenschist to amphibolite facies meta

turbidites and metagreywackes, and post-orogenic granitoid plutons (Card and Ciesielski, 1986; Percival et al., 2012). The volcano-plutonic units of the Superior Province, including the Wawa-Abitibi and Wabigoon terranes as well as the Uchi domain, are characterized by belts of greenschist-grade supracrustal rocks intricately interwoven with one another. These supracrustal sequences are spatially associated with syn- and post-orogenic felsic plutons (Thurston and Chivers, 1990; Stott, 1997; Percival et al., 2012). The Wabigoon terrane is dated between 2.7 and 3.0 Ga and is primarily composed of volcanic and plutonic rocks, such as basalts, andesites, and granitoids, as well as metamorphic rocks like gneisses and schists (Thurston and Chivers, 1990; Percival et al., 2012). The 2.6-2.8 Ga Abitibi terrane is primarily composed of volcanic and plutonic rocks such as basalts, andesites, komatiites, and granitoids; and host significant gold mineralization (Card and Ciesielski, 1986; Percival et al., 2012). The 2.7 Ga Winnipeg River terrane is characterized by assemblages of metasedimentary and metavolcanic rocks of greenschist to amphibolite grade, as well as by felsic and mafic intrusions (Card and Ciesielski, 1986).

The assembly of the Superior Province resulted from complex geological processes that took place over millions of years, primarily through crustal accretion during the Kenoran orogeny between 2.72 and 2.68 Ga (Stockwell, 1972; Stott, 1997; Percival et al., 2006). More recent studies have identified five major accretionary events during this orogeny (2.72-2.68 Ga), which show similarities in terms of magmatism, metamorphism, plutonism, deformation, and sedimentation (Percival et al., 2006). These accretionary events are marked by the collision and subduction of major volcano-plutonic terranes or groups of accreted terranes evolution (Percival et al., 2006).

2.2 Marmion terrane

The Marmion Terrane, a major component of the Wabigoon Subprovince (Fig. 2.2), is characterized by a suite of plutonic rocks including tonalites, granodiorites, and granites. According to geochronological studies and remapping, its evolution reflects the periodic accumulation of crustal and magmatic materials in an arc setting (Stone and Davis, 2006). Bordered by metasedimentary units of the Quetico Subprovince and metavolcanic assemblages of the adjacent Wabigoon Terrane, the Marmion Terrane forms an integral part

of the greenstone belt architecture of the region. The sedimentary protoliths include quartzites, pelites, and greywackes (Stott et al., 2010). The tectonic history of the Marmion Terrane is complex, marked by multiple episodes of subduction and collision that deformed and metamorphosed these rocks to greenschist–amphibolite facies conditions (Stone and Davis, 2006; Stott et al., 2010). The Marmion Terrane, a major component of the Wabigoon Subprovince within the Superior Province (Fig. 2.2), is characterized by a suite of plutonic rocks including tonalites, granodiorites, and granites. According to geochronological studies and remapping, its evolution reflects the periodic accumulation of crustal and magmatic materials in an arc setting (Stone & Davis, 2006). Bordered by metasedimentary units of the Quetico Subprovince and metavolcanic assemblages of the adjacent Wabigoon Terrane, the Marmion Terrane forms an integral part of the greenstone belt architecture of the region. The metasedimentary rocks include quartzites, pelites, and greywackes (Stott et al., 2010). The tectonic history of the Marmion Terrane is complex, marked by multiple episodes of subduction and collision that deformed and metamorphosed these rocks to greenschist–amphibolite facies conditions (Stone and Davis, 2006; Stott et al., 2010).

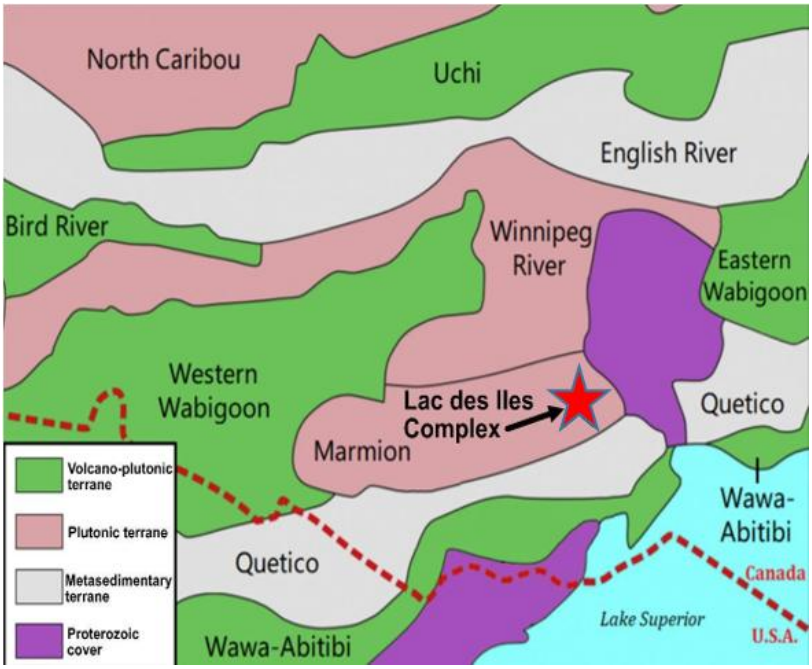

Figure 2.2 – Map of terrane subdivisions showing the location of the Marmion Terrane within the Superior Province (modified from Stott et al., 2010; Sotiriou et al., 2018). Location of the Lac Des Iles Complex also shown.

One of the distinctive features of the Marmion Terrane is the presence of syntectonic plutons, which cooled slowly in a compressive environment, producing adcumulate textures (Žák et al., 2017). The terrane is also known for its mineralization, particularly gold and platinum group metals, exemplified by deposits such as the Hammond Reef gold deposit, hosted in granodioritic to tonalitic plutons, and PGE occurrences associated with mafic–ultramafic intrusions within the terrane (Davis et al., 1990; Fralick et al., 2002; Dubé et al., 2010).

2.3 Lac des Iles suite

Located in the Thunder Bay mining district of Northwestern Ontario, the Lac des Iles suite is one of several Late Archean (2.68–2.69 Ga; Stone, 2003) mafic to ultramafic layered intrusive rocks, emplaced within the Marmion terrane, near its southern margin with the Quetico basin (Fig. 2.3; Brügmann et al., 1997; Stone and Davis, 2006). The Lac des Iles complex, together with the Buck, Demars, Dog River, Legris, Taman, Tib, and Wakinoo intrusions, form the Lac des Iles suite (Fig. 2.3). These intrusions contain magmatic sulfide mineralization that are rich in platinum group elements (PGEs), including Pd mineralization found in the South Lac Des Iles complex, which is host to an economically mineable deposit (Decharte et al., 2018). A variety of mafic rocks, such as gabbro, leucogabbro, hornblende gabbro, and norite, make up the intrusions of South Lac Des Iles. Ultramafic rocks are rare, except the stratified complex of North Lac Des Iles (Sutcliffe and Smith, 1988; Djon et al., 2017). The age of the South Lac Des Iles complex has been determined to be 2.68–2.69 Ga, whereas the North Lac Des Iles has been estimated to be 2687 ± 1.6 Ma (Heaman and Easton, 2006; Stone and Davis, 2006). The dates of other intrusions around Lac des Iles include Tib Lake, dated at 2733 ± 2 Ma, Buck Lake 2730 ± 4 Ma, Shelby Lake 2917–2728 Ma (Bain et al., 2023), Legris Lake 2690 ± 0.77 Ma (Bain et al., 2023) and Taman Lake 2735 ± 3 Ma (Good et al., 2000). The origin of the Lac des Iles suite has been the subject of discussion over the years, each aiming to explain the magmatic and geological processes that shaped the region.

Barnes et al. (1993) proposed that the Lac des Iles suite may have resulted from the partial melting of an enriched mantle. A distinct isotopic signature, suggesting that the initial magma was generated from a metasomatized mantle, likely under the influence of PGM-rich fluids. This model helps explain the abundance of Pd mineralization, a notable feature of LDIC deposit.

Stern et al. (1989) proposed an alternative model in which the entire Lac des Iles intrusive suite formed during the collision between the Quetico and Wabigoon subprovinces. In this interpretation, emplacement of the suite was broadly coeval with sanukitoid magmatism characteristic of subduction-related tectonic environments, linking its origin to regional collisional processes.

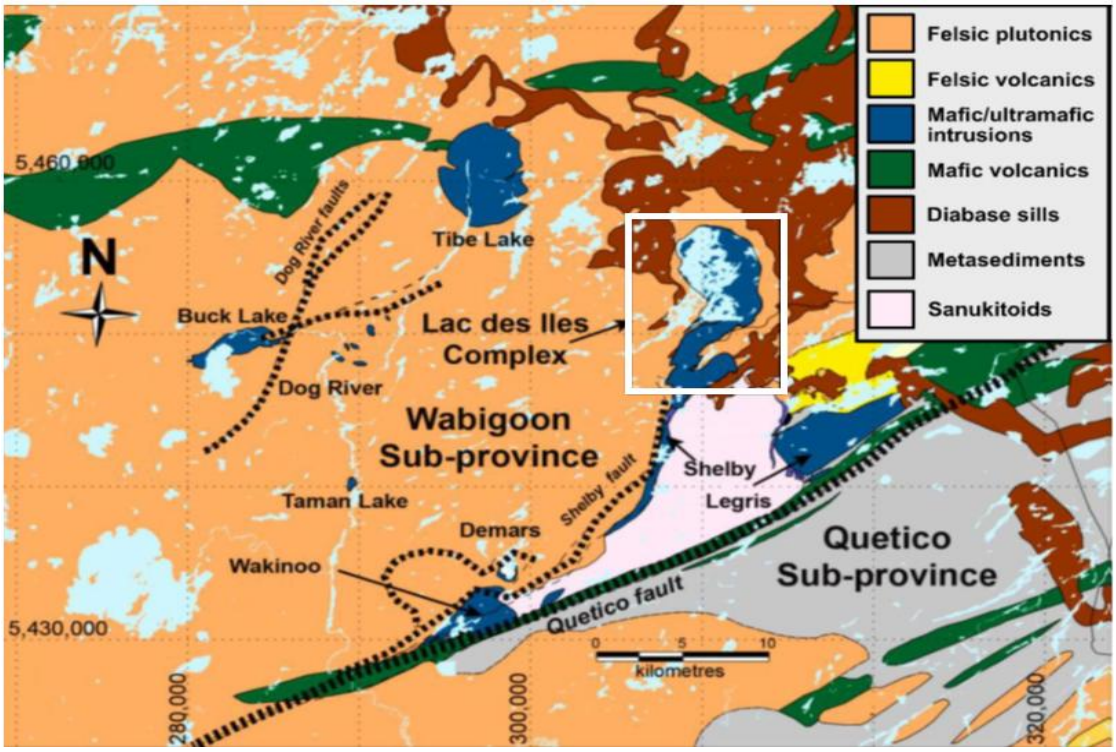

Figure 2.3 – Regional geology of the Lac des Iles suite intrusions (in dark blue) and Lac des Iles Complex in the white box (Modified from Djon et al., 2017).

Recent research indicates that the Lac des Iles magmatic suite is primarily composed of mafic to ultramafic rocks, with syntectonic intrusions dating from 2.7 to 2.8 Ga, typical of an island arc environment (Good et al., 2020). These mafic intrusions are associated with episodes of magmatic differentiation that resulted in significant Pd and platinum (Pt) mineralization (Barnes and Gomwe, 2011). The process of fractional crystallization, combined with interactions between the magma and the crust, facilitated the concentration of the precious metals (Good et al., 2020). In this context, the sulfide mineralization of the Lac des Iles suite is primarily magmatic in origin, derived from sulfide liquids exsolved from the evolving magma. Deep crustal structures such as the Quetico Fault (Fig. 2.3) acted as conduits that influenced magma emplacement and crustal

contamination, while later hydrothermal fluids may have locally modified or remobilized the sulfides (Stone and Davis, 2006; Barnes and Gomwe, 2011).

2.4 Lac des Iles Complex

The Lac des Iles Complex (LDIC) is the largest intrusive body within the Lac des Iles suite, comprising the North and South Lac Des Iles Complexes (Fig. 2.4) and covering approximately 9 km from north to south and 4 km from east to west (Buss et al., 2017). The Neoarchean Lac des Iles Complex was emplaced into tonalitic gneisses of the Marmion terrane (Tomlinson et al., 2003), located immediately north of the boundary between the Wabigoon and Quetico subprovinces (Figs. 2.2, 2.3). The complex, along with its associated intrusions, was emplaced concurrently with sanukitoid magmatism along pre-existing northeast-trending faults, within the structural collision zone between the Quetico and Wabigoon subprovinces (Djon, 2017). One of the earliest interpretations proposed by Good et al. (1989) suggested that the Lac des Iles Complex formed through fractional crystallization from a basaltic magma. This explains the compositional variation of the ultramafic to mafic rocks observed in the region, characterized by a progressive concentration of platinum-group elements (PGE) through magmatic differentiation. The North Lac Des Iles Complex is predominantly ultramafic with a minor component of mafic rocks, including clinopyroxenites, websterites, and gabbronorites (Brugmann et al., 1989; Lavigne and Michaud, 2001). The Mine Block Intrusion, now recognized as the Roby and Offset Zones, is texturally and compositionally complex, containing rock types such as anorthosite, leucogabbronorites, melanogabbronorites, chlorite-actinolite schists, and magnetite-rich gabbros (Lavigne and Michaud, 2001; Watkinson et al., 2002; Gomwe et al., 2011; Bautista, 2024). Lastly, the Camp Lake Zone, which is compositionally homogeneous, consists of hornblende gabbros and gabbronorites (Brugmann et al., 1989; Lavigne and Michaud, 2001; Michaud and Lavigne, 2003; Smith et al., 2024). Pd mineralization is found in magmatic breccias of the gabbronorite, as well as in chlorite-actinolite schists (Gomwe et al., 2011).

2.4.1 The North Lac Des Iles Complex

The North Lac des Iles Complex is an elongated composite intrusion composed of several low-dip stacked intrusions, with surface exposure extending approximately 6 km from north to south and 4.5 km from east to west (Fig. 2.4). The North Lac Des Iles Complex, primarily made up

of ultramafic rocks such as peridotites and websterites, forms distinct cyclic units (Sutcliffe and Sweeny, 1986). Also known as the Northern Ultramafic Center (Fig. 2.4), it hosts occurrences of weak stratiform platinum-group element (PGE) mineralization (Djon et al., 2017). Mapping and drilling have identified fourteen distinct cyclic units, each characterized by cumulate sequences derived from two different parental magmas (Djon et al., 2017). Type A units originate from a magma enriched in silica and incompatible elements, favoring the formation of orthopyroxenes, whereas Type B units, derived from a magma poorer in silica, are dominated by olivines and clinopyroxenes. These units exhibit cryptic stratigraphy, with variations in the magnesium content of olivines and pyroxenes, reflecting the fractional differentiation of magmas during the progressive cooling of the magma chamber (Djon et al., 2017). PGE mineralization in the North Lac Des Iles Complex is interpreted to have resulted from sulfide saturation triggered by dynamic fractional crystallization and multiple magma injections. The mineralized zones are found within websterite and gabbronorite horizons, containing disseminated sulfides, primarily pyrrhotite, chalcopyrite, and pentlandite, making up between 0.5% and 2% of the total volume. PGE, notably Pd, are enriched in these zones, often in the form of minerals such as palladium tellurides (Pd-Te) and bismuthotellurides (Bi-Te), (Djon et al., 2018).

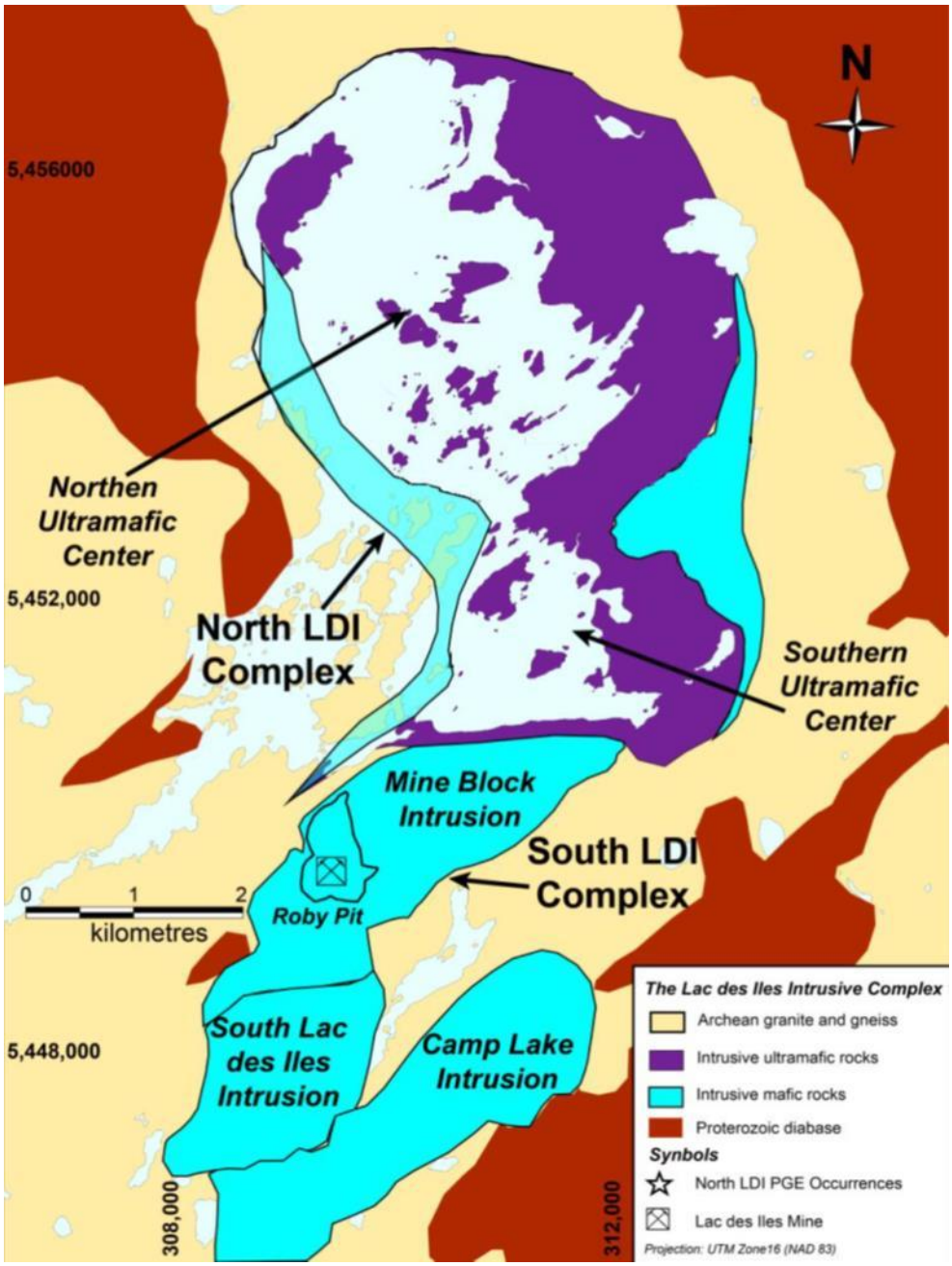

Figure 2.4 – Map of the Lac des Iles Complex showing the subdivision of the South Lac des Iles Complex into three discrete intrusions (modified from Djon, 2017).

2.4.2 The South Lac Des Iles Complex

The SLDIC is a multiphase mafic intrusive body emplaced into orthogneiss of intermediate composition (Gomwe, 2008), with an emplacement age of approximately 2.68 Ga (Stone & Davis, 2006). Its arcuate geometry and internal architecture are interpreted to be structurally controlled by a network of subvertical faults, including the north-trending Shelby Lake Fault (SF), the northeast-trending Roby Central Fault (RCF), and several subsidiary fault zones (Fig. 2.5). These structures not only influenced the shape of the intrusion but also played a key role in localizing mineralization. Most known mineral resources are concentrated along or near these fault zones, with the Roby Offset deposit situated at the intersection of SF and RCF (Impala Platinum Holdings Limited, 2022). The complex spans approximately 5.5 km north–south and 3.5 km east–west (Djon et al., 2017).

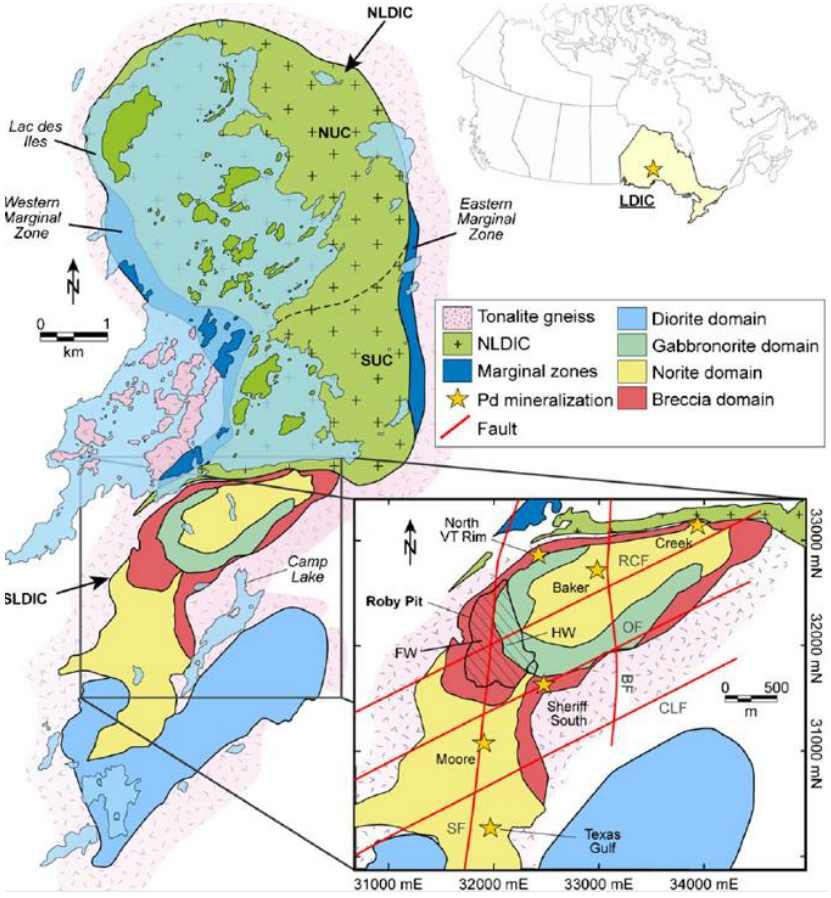

Figure 2.5 – Map of the South Lac des Iles Complex (SLDIC), with updated geologic subdivisions. NUC- Northern Ultramafic Center, SUC - Southern Ultramafic Center, RCF - Roby central fault, OF - Offset fault, BF - Baker fault, CLF - Camp Lake fault, SF - Shelby f fault, FW - Footwall, HW - Hanging wall. (modified from Smith et al., 2024).

In recent years, Impala Canada has proposed a revised geological model for the SLDIC, based on integrated geophysical, lithological, and geochemical datasets (Impala Platinum Holdings Limited, 2022). In this interpretation, the SLDIC is regarded as a single multiphase intrusion, subdivided into three principal structural zones: The Roby Zone, the Offset Zone, and the Camp Lake Zone. These subdivisions are delineated by major faults and geophysical contrasts, and differ significantly from earlier models (e.g., Brugmann et al., 1989; Gomwe et al., 2011), which instead distinguished broader lithological domains such as gabbronorite, breccia, norite, and diorite. The revised model highlights the critical role of fault systems, notably the Roby Central Fault and the Shelby Lake Fault, in controlling both the internal architecture of the complex and the localization of mineralization, with the Roby Offset deposit situated at the intersection of these major structures (Fig. 2.5).

The SLDIC comprises three distinct mafic zones: Roby Zone, Offset Zone and Camp Lake (Lavigne and Michaud, 2001; Fig. 2.6). Recent petrographic and geochemical studies conducted by Lac Des Iles Mine (LDIM) have revealed that most of the mafic rocks in the SLDIC, particularly those associated with Pd mineralization, are orthopyroxene-dominated norites (Impala Platinum Holdings Limited, 2023). In these norites, orthopyroxene is the primary ferromagnesian silicate cumulus mineral, whereas clinopyroxene, when present, occurs as the lowest-temperature intercumulus phase (Djon et al., 2010; Impala Platinum Holdings Limited, 2022). The distribution of the main rock units within the LDIC South Complex is depicted in Figure 2.5. Four major domains have now been identified within the SLDIC. The oldest, referred to as the gabbroic domain, comprises two units: a magnetite-rich gabbro (GAB Mt) and an equigranular gabbronorite (EGAB) enriched in plagioclase (Dechartes et al., 2018). The other domains include the norite domain, the breccia domain, and the diorite domain, each distinguished by their lithological characteristics and geophysical signatures (Fig. 2.5).

A significant magmatic event in the SLDIC led to the formation of the norite and breccia series (Brügmann et al., 1989; Sutcliffe, 1989; Lavigne and Michaud, 2001; Barnes and Gomwe, 2011). In highly altered zones, the norite series has undergone extensive alteration, resulting in a secondary mineral assemblage primarily composed of amphibole and chlorite, along with smaller amounts of talc, sericite, and epidote-group minerals. The main minerals

present are plagioclase and orthopyroxene, which make up the majority of the rock matrix. The norites often exhibit adcumulate or mesocumulate textures. In these slightly altered environments, amphibole is primarily interstitial and anhedral, and its composition tends toward hornblende (Barnes and Gomwe, 2011). In regions of higher-grade metamorphism, the altered norite is highly foliated, characterized by aligned chlorite grains that impart a pervasive schistosity (Gomwe, 2008). The section of the breccia and norite series, previously known as the "Mine block intrusion", now known as the Roby and Offset Zone (Fig 2.6), primarily consists of massive, variably textured gabbronorites and norites, ranging from leucocratic to melanocratic varieties. These zones also include metagabbronorites and chlorite-actinolite schist (Lavigne and Michaud, 2001; Barnes and Gomwe, 2011).

The breccia series shares a similar overall composition with the norite series but is generally more leucocratic. It exhibits significant textural heterogeneity, with highly variable grain sizes and widespread magmatic brecciation, characterized by a diverse range of lithic fragment sizes and geometries (Lavigne and Michaud, 2001; Decharte et al., 2018). In both the breccia and norite series. The olivine in the SLDIC, with a composition ranging from $Fo_{78.6}$ to $Fo_{81.8}$, is characteristic of crystallization from a hydrous basaltic-andesitic magma and these olivine grains display polymineralic melt inclusions and are partially serpentinized, with peritectic orthopyroxene rims and reactions involving amphiboles (Smith et al., 2024).

Sulfide mineralization in the SLDIC is disseminated in nature. Sulfide assemblages include pyrrhotite + chalcopyrite + pentlandite ± pyrite in fresh rocks, whereas in altered rocks chalcopyrite + pyrite ± millerite is more common (Djon and Barnes, 2012). Pd mineralization is primarily hosted in discrete platinum-group minerals (PGMs) within disseminated magmatic sulfides, including Pd-bearing arsenides, tellurides, and sulfides. It also occurs in solid solution within base metal sulfides such as pentlandite, and less commonly in millerite, though these represent secondary hosts (Hinchey et al., 2010; Djon and Barnes, 2012; Boudreau et al., 2014).

The Roby and Offset zones (Fig. 2.6) are steeply dipping areas, 50 to 400 meters wide, consisting of chlorite-actinolite schist and metagabbronorite with 0 to 3 wt% sulfides. These zones, though offset by a fault, are believed to have originally been part of a continuous

mineralized zone (Duran et al., 2016). The Pd mineralization in South Lac Des Iles complex Complex is mainly concentrated in the gabbronorite and norite domains (Smith et al., 2024). They account for the majority of the mineralization in the SLDIC (Decharte et al., 2018).

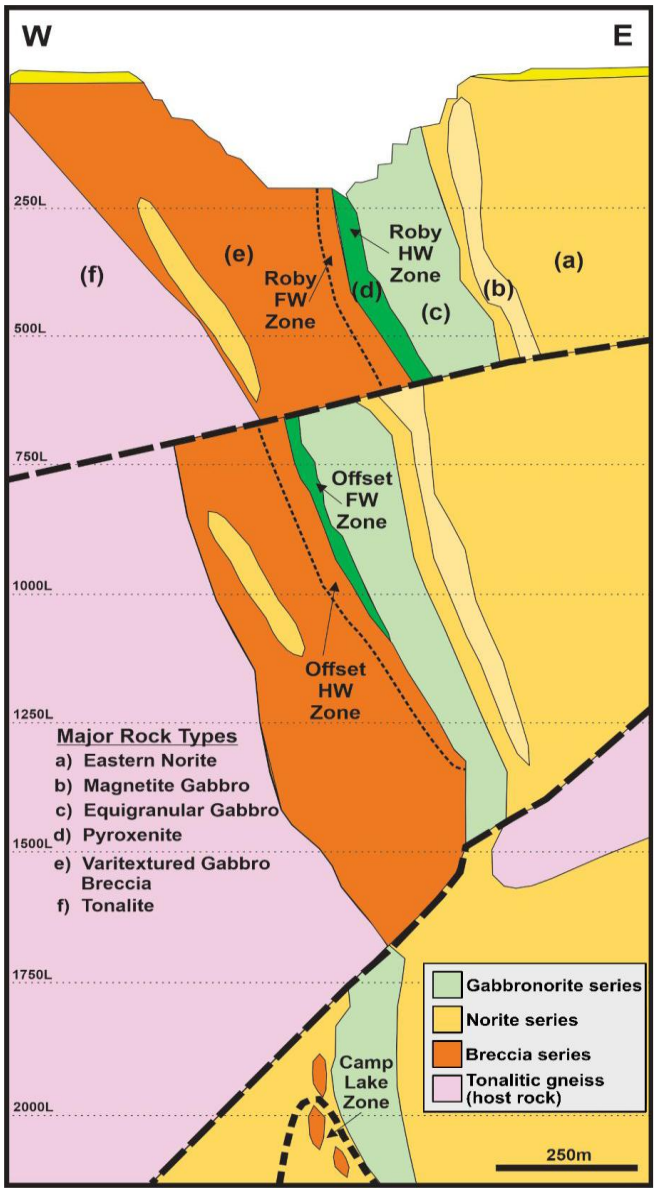

Figure 2.6 – North-looking cross-section showing the geological domains of the Roby and Offset zones and their surrounding lithologies (elevation in metres below surface). Image courtesy of Impala Canada.

The Camp Lake Zone is a mineralized area located beneath the Camp Lake fault, characterized by a southwest dip and a depth ranging from 456 m to 1012 m (Smith et al.,

2024; Fig. 2.6). In the Camp Lake Zone, the rock types include mafic to intermediate dykes, with contacts commonly marked by disseminated sulfides and magnetite veins.

Models have been developed to explain the formation of SLDIC and its geological characteristics; most of them include several stages of magmatism, and many involve some degree of PGE redistribution by hydrothermal fluid. For example, Brugmann et al. (1989) argued that the formation of the SLDIC resulted from magmatic differentiation associated with mafic and ultramafic intrusions. They also highlighted that tectonic events, combined with magma reinjection, contributed to the concentration of Pd and other precious metals. On the other hand, some authors (Lavigne and Michaud, 2001; Hinchey et al., 2005; Peck et al., 2016) have argued that the brecciation of the Lac des Iles deposit was triggered by the emplacement of successive magmatic pulses, with palladium enrichment occurring at depth and subsequently being redistributed to its present position during later stages of intrusion. Hinchey et al. (2005) and Barnes & Gomwe (2011) further emphasized that the formation of the SLDIC was strongly influenced by magmatic interactions with the surrounding rocks and by regional tectonic events. These processes played a key role in the concentration of precious metals, particularly palladium, by driving sulfide saturation in the evolving magma. The exsolved sulfide liquid efficiently scavenged palladium and other platinum-group elements from the silicate melt, leading to their incorporation into disseminated magmatic sulfides and discrete platinum-group minerals within the Lac des Iles Complex. The occurrence of the highest-grade Pd mineralization in chlorite-actinolite schist (Gomwe et al., 2011), but also the low sulfur content and the general lack of correlation between Pd and S in the SLDIC, has been used to suggest that relatively low-temperature hydrothermal fluids transported Pd into the schist after the complete crystallization of the SLDIC (Hinchey et al., 2005; Barnes and Gomwe, 2011). Other models suggest that PGE concentration in high chlorite-actinolite schist predates the low-temperature hydrothermal alteration, either by magmatic processes (Decharte et al., 2018) or by high-temperature hydrothermal processes (Schisa et al., 2015).

Open-pit mining operations at the Lac des Iles mine began in 1993, followed by the start of underground mining in 2006. The Roby and Offset zones have consistently been the main hubs of underground activity, with the Roby zone also having been historically mined at

the surface. Over the years, underground operations have expanded to several satellite deposits connected to the Offset Zone, including areas B2, B3, C, and the Camp Lake Zone. In parallel, intermittent open-pit mining has been carried out in the Twilight Zone, located immediately west of the Roby Zone and adjacent to the Sherriff Pit (Decharte et al., 2018).

As of June 30, 2022, the mine's cumulative production totaled 69.08 million tonnes, with an average grade of 1.91 g/t Pd and 0.14 g/t Pt, amounting to 4.28 million ounces of Pd and 329,300 ounces of Pt (Campbell et al., 2023). The Roby and Offset Zones, which are the primary sources of mineralization, show average Pd grades of 4 g/t across true widths ranging from 10 to 30 meters, with peak values exceeding 10 g/t over several meters. The Roby-Offset mineralized body remains open to the south and at depth, particularly in the Camp Lake Zone, which extends vertically for approximately 650 meters and reaches up to 100 meters in thickness at a depth of around 1,800 meters (Impala Canada, Lac des Iles Mine Property Technical Overview, 2023). Although the 2023 technical report does not provide a precise tonnage estimate, internal data from Impala Canada indicate a historical annual production exceeding 200,000 ounces of Pd. The proven and probable mineral reserves were estimated at 40.4 million tonnes, with grades of 1.90 g/t Pd, 0.18 g/t Pt, 0.14 g/t gold (Au), 0.06% nickel (Ni), and 0.06% copper (Cu). This corresponds to a total of 2.48 million ounces of Pd, 230,000 ounces of Pt, and 180,000 ounces of gold (Impala Platinum Holdings Limited, 2022).

Chapter 3 - Methods

3.1 Sampling

The Camp Lake Zone sampling campaign focused on two drill holes completed during the fall of 2022 and winter of 2023 (Fig. 3.1). Samples were collected systematically along the drill holes, not at fixed intervals, but to capture the full diversity of lithologies and structures identified during core logging by the mine. In total, 120 samples were collected for analysis.

Table 3.1 – Location of drill collars and orientation of drill core.

Drill hole	North	East	Elevation	Collar Dip	Collar Az	Length (m)
22-711	31,255.54	32,359.22	-566.00	-58.70	261.70	1,443.00
22-712	31,255.54	32,359.22	-567.00	-56.80	286.61	1,287.00

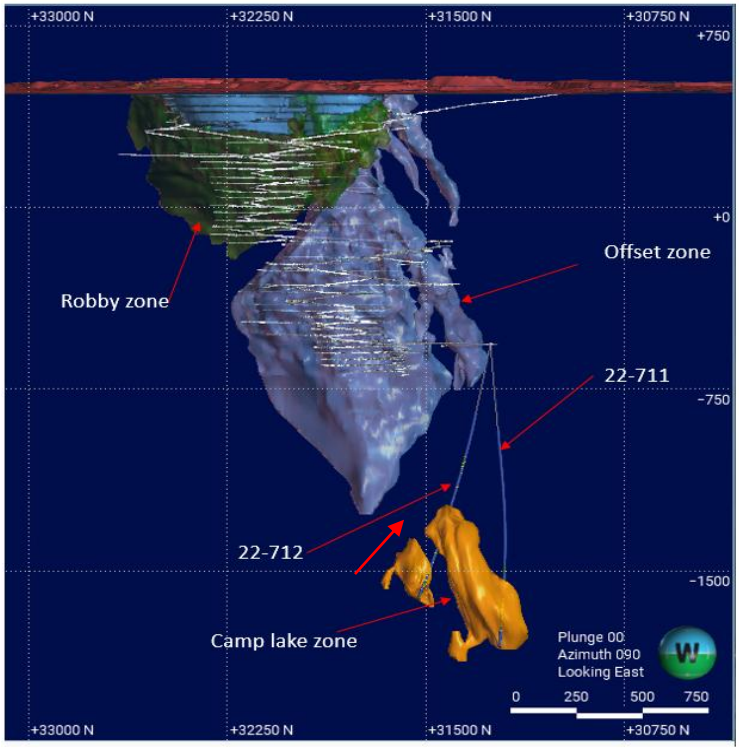

Figure 3.1 – Geological model of the Camp Lake Zone showing location of the drill holes 22-711 and 22-712 (Impala Canada, 2024).

3.2 Petrography

Petrography of silicate and sulfide minerals was carried out on hand specimens and polished thin sections. Samples were sent to the Lakehead University lapidary laboratory for preparation into polished thin sections. Thirty samples were selected to represent key lithologies encountered in the two drill holes. Petrographic analysis was conducted using an Olympus BX2M and Zeiss axioscope, and photomicrographs were captured using an Olympus SC180 camera at Lakehead University. Detailed petrographic descriptions of each thin section are provided in Appendix I.

3.3 Scanning electron microscopy (SEM)

Ten thin sections were selected for further analysis based on their palladium content and sulfide abundances. A scanning electron microscope (SEM) was used to identify and characterize platinum-group minerals (PGM). Polished thin sections were carbon-coated using an Edwards Auto 306 Carbon Coater 24 hours prior to analysis. All SEM work was carried out at the Lakehead University Instrumentation Laboratory (LUIL) using a Hitachi SU-70 Schottky Field Emission SEM equipped with an Oxford Aztec 80 mm/124 eV EDS detector. After insertion of the thin sections into the chamber, contrast, brightness, and working distance were manually optimized for each session. PGM were located through systematic manual scanning of each thin section at magnifications of 500× to 3000×, focusing on sulfide grains, silicate–sulfide contacts, and microfractures where PGM commonly occur. Mineral identification was confirmed using EDS spectra and elemental maps. The electron beam was calibrated against a metal-block standard at the start of each session and periodically thereafter, and the EDS system was calibrated using Pd or Pt standards to maintain an accuracy of ±1% for PGM analyses.

3.4 Whole Rock Geochemistry

Thirty samples from drill holes 22-711 and 22-712 were analyzed at the ALS Geochemistry laboratory in Thunder Bay using the Complete Characterization Package (CCP-PKG01) and the fire assay method for platinum-group elements (PGMICP23). The samples were first crushed to 70% passing <2 mm, after which a 250 g split was pulverized to 85% passing 75 µm. The CCP-PKG01 package includes whole-rock major element analyses, trace elements by fusion, volatiles by aqua regia digestion, and carbon and sulfur by combustion. Platinum-group elements were determined

by fire assay using a standard lead-oxide collection method followed by inductively coupled plasma atomic emission spectroscopy (ICP-AES). Full analytical results and detection limits are provided in Appendix II.

The CCP–PKG01 workflow integrates X–ray fluorescence (XRF) and inductively coupled plasma mass spectrometry (ICP–MS). Major oxides and trace elements were measured following lithium borate fusion, while carbon and sulfur were quantified by combustion. Base metals were analyzed using a four–acid digestion ($HF–HNO_3–HClO_4–HCl$). For PGE determination, the PGMICP23 method was applied: samples were fused with a flux to collect precious metals into a lead or nickel sulfide button, which was subsequently cleaned, dissolved, and analyzed by ICP–MS to achieve high–sensitivity measurements.

Whole-rock data were also used to support petrographic interpretations through CIPW normative calculations. Major oxide concentrations, recalculated on an anhydrous basis, were renormalized to 100% before computation. Normative minerals were calculated in IoGas–64 version 8.1, using the “CIPW Norm Calculation” module, which converts oxide weight percentages into molecular proportions and allocates them to idealized anhydrous mineral phases following the standard CIPW sequence. When only total Fe_2O_3 was reported, IoGas applied its default FeO–Fe_2O_3 partitioning parameters. The resulting normative assemblage included quartz, orthoclase, albite, anorthite, diopside, hypersthene, olivine, nepheline, leucite, apatite, ilmenite, magnetite, and hematite. See Appendix V for results of the calculations.

3.5 Sulfur isotopes

Sulfur isotope analyses were conducted on powders of pyrite, chalcopyrite, and pyrrhotite, separated by micro-drilling individual sulfide grains using a Jobmate drill equipped with a 2-mm diamond bit. Each analysis required at least 0.5 mg of material. The sulfide powder was collected on clean paper and transferred into glass vials. To minimize contamination, fresh latex gloves and paper were used for each sample, and the drill bit, balance, and preparation surface were cleaned between samples. Any potential contamination from the steel drill bit is considered negligible, as hardened steels typically contain only a few hundredths of a wt% S—well below 0.1 wt%—and sulfides are significantly more brittle than steel.

The sulfide powders were carefully weighed into tin capsules and combusted in a Costech ECS 4010 Elemental Analyzer coupled to a MAT 253 Stable Isotope Ratio Mass Spectrometer (EA-CF-IRMS) at the Department of Geological Sciences, Queen's University. The $\delta^{34}S$ values were standardized against the Vienna Canyon Diablo Troilite (VCDT) international reference material (Table 3.1) and are reported in delta (δ) notation in per mil (‰). Analytical reproducibility is ±0.3‰ (2σ). The measured values of international sulfur isotope standards (Table 3.2) closely match their published $\delta^{34}S$ compositions, confirming the high precision and reproducibility of the EA-CF-IRMS analyses.

Table 3.2 – Comparison between published $\delta^{34}S$ values of international reference materials (VCDT) and replicate analyses from this study, demonstrating instrument precision.

Standard ID	Published $\delta^{34}S$ (‰, VCDT)	This study (n=3)
NBS127	20.3 +/- 0.4	20.2 +/- 0.2
IAEA-SO-6	–34.1 +/- 0.2	-34.1 +/- 0.1
NBS123	17.1 +/- 0.3	17.5 +/- 0.3

3.6 Geochronology

U-Pb geochronology on zircon from a vari-textured gabbro of the Camp Lake Zone (Fig. 3.2) was carried out at the Jack Satterly Geochronology Laboratory, University of Toronto, to obtain a precise date of rock emplacement. The sample was crushed using a conventional jaw crusher and ground into a coarse powder using a hardened steel disk mill. Heavy minerals were separated by passing the concentrate over a shaking, riffled water table multiple times, followed by density separations with methylene iodide and paramagnetic separations with a Frantz isodynamic separator. The final selection of the sample involved hand-picking under a binocular microscope in alcohol to choose the freshest, least cracked, core- and inclusion-free grains of zircon.

The analytical techniques involved isotope dilution thermal ionization mass spectrometry (IDTIMS) following a process of chemical abrasion (CA), adapted from the method outlined by Mattinson (2005). Zircon grains underwent CA pre-treatment, initially undergoing annealing in quartz crucibles at a temperature of 900°C for two days. Subsequently, the annealed grains were subjected to etching in approximately 0.10 ml of concentrated hydrofluoric (HF) acid for several

hours within Teflon vessels at a temperature of 200°C. Altered portions of the crystals, which harbor isotopically disturbed lead, dissolve more rapidly than the annealed, unaltered crystal domains, particularly for zircons exhibiting low to moderate levels of radiation damage. The degree of etching varied, contingent upon the uranium concentration within the grains and the resulting extent of radiation damage.

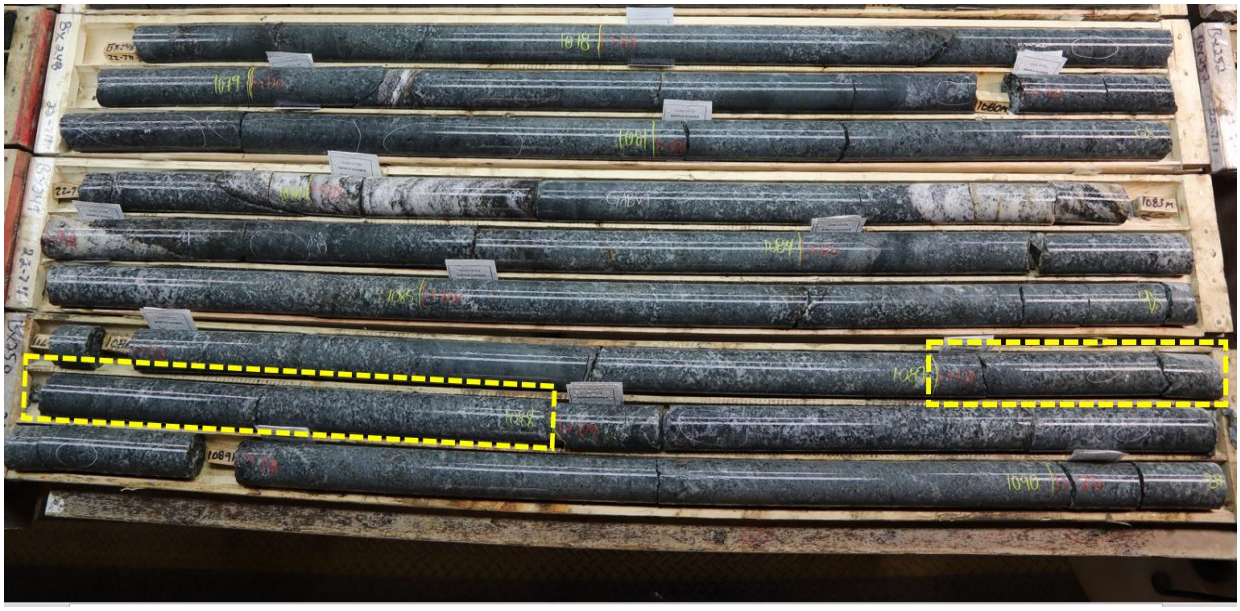

Figure 3.2 – Vari-textured gabbro from sample 22 711 gc 001 selected for U–Pb geochronology (1087–1088 m). Dashed yellow boxes highlight the intervals chosen for analysis.

Mineral fractions chosen for ID-TIMS analysis were weighed using estimated weights derived from scaled digital photomicrographs and the density of zircon. These estimates are expected to be accurate within approximately ±20%. This margin of error impacts the concentrations of uranium (U) and lead (Pb) but does not affect age determinations, which rely solely on isotope ratio measurements. After chemical abrasion, the samples were briefly washed and subjected to sonication (which helps improve sample homogeneity, guaranteeing more accurate isotopic measurement) in 7N HNO_3 for approximately 30 minutes before dissolution. For one fraction (Z1), a mixed ^{205}Pb-^{233}U-^{235}U isotopic spike (EARTHTIME 535) was added, while for two other fractions (Z2, Z3), a ^{205}Pb-^{235}U isotopic spike (JSGL/ROM tracer) was introduced into the dissolution capsules during sample loading. Zircon grains were dissolved using concentrated hydrofluoric acid (HF) in Teflon bombs at 195°C for 3-4 days, followed by drying and re-dissolution in 3N HCl overnight (Krogh, 1973). Uranium and lead were isolated using 50-microliter anion exchange columns with

HCl elutions, subsequently dried down, and loaded onto outgassed rhenium filaments with silica gel (Gerstenberger and Haase, 1997).

Pb and UO_2 underwent analysis using a VG354 mass spectrometer with a Daly collector operating in pulse counting mode. The detector's mass discrimination correction remained consistent at 0.07% per atomic mass unit (AMU). Additionally, thermal mass discrimination corrections of 0.10% per AMU were applied for Pb and U. Throughout the analytical period, the Daly system had a dead time of 15 nanoseconds for Pb, monitored using the SRM982 Pb standard.

Mass spectrometer data underwent reduction using proprietary software developed at University of Toronto (UtilAge and Integrated UtilAge programs), by D. Davis. Corrections were applied for the initial ^{230}Th disequilibrium in zircon to the $^{206}Pb/^{238}U$ ages, assuming a Th/U ratio in the magma of 4.2. All common Pb, below one pg, was attributed to procedural blank. Initial Pb from geological sources above 1 pg was adjusted utilizing the Pb evolution model of Stacey and Kramers (1975). Concordia curves were plotted, data regressions were conducted, and age results were averaged using the Isoplot 3.71 Add-In for MS Excel, developed by Ludwig (2009). The Concordia curve is depicted as a 'band,' incorporating uncertainties in the ^{235}U and ^{238}U decay constants; however, final age calculations do not include uncertainties in the U decay constants. Probabilities of fit would be expected to average 50% for random data with appropriately chosen analytical errors. Age errors and error ellipses are reported at the 2 sigma or 95% confidence level.

3.7 Sm-Nd isotopes

Ten samples were selected and prepared in the clean laboratory of the Isotope Geochronology and Geochemistry Research Centre (IGGRC) at Carleton University for samarium-neodymium (Sm-Nd) isotopic analysis. The selection aimed to capture the diversity of geochemical signatures in light rare earth elements (LREE) identified through whole-rock analyses. Rock powders were spiked with a ^{148}Nd-^{149}Sm isotopic tracer before being dissolved in a mixture of concentrated HF and HNO_3 acids. The resulting solution was then dried down, and the residues were sequentially dissolved in 7M HNO_3 followed by 6M HCl, before being fully evaporated.

The sample residues were dissolved in 1.5 ml of 2.5M HCl and loaded onto 14-ml borosilicate glass chromatography columns (Bio-Rad) containing 3.0 ml of Bio-Rad AG50W-X8 cation exchange

resin. The columns were washed with 3.5 ml of 6M HCl before rare earth elements were eluted using 9 ml of 6M HCl. REE fractions were dissolved in 0.26M HCl and loaded onto 2 ml pre-packed Ln resin columns (Eichrom Technologies, LLC, USA). Neodymium was eluted using 0.26M HCl, followed by samarium (Sm) elution using 0.5M HCl.

Nd isotopic ratios were measured using IGGRC's Thermo-Finnigan Neptune multi-collector inductively coupled plasma mass spectrometer (MC-ICP-MS). Isotopic ratios were normalized to $^{146}Nd/^{144}Nd = 0.7219$. The $^{143}Nd/^{144}Nd$ ratios were corrected for instrumental drift using sample-standard bracketing against the average JNdi-1 value of 0.512100, as measured by IGGRC's Thermo-Finnigan Triton TIMS. Isotopic results were then recalculated using the previously determined age of 2690 Ma for the Camp Lake Zone. The average value of the JNdi-1 reference material used for bracketing over the ten-month analysis period was $^{143}Nd/^{144}Nd = 0.512096 \pm 0.000013$ (2SD, n=104). Total procedural blanks were below 50 pg for Nd.

Chapter 4 - Results

4.1 Petrography

The Camp Lake mineralized zone is located at the contact of the footwall of the equigranular gabbro and is mainly associated with norite and, to a lesser extent, with the vari-textured gabbro (Fig. 4.1). These lithologies belong to the gabbroic and noritic domains of the SLDIC, thereby linking the Camp Lake mineralization to the broader intrusive framework described in the introduction. Thirty samples from two drill holes were selected for thin section preparation and petrographic analysis.

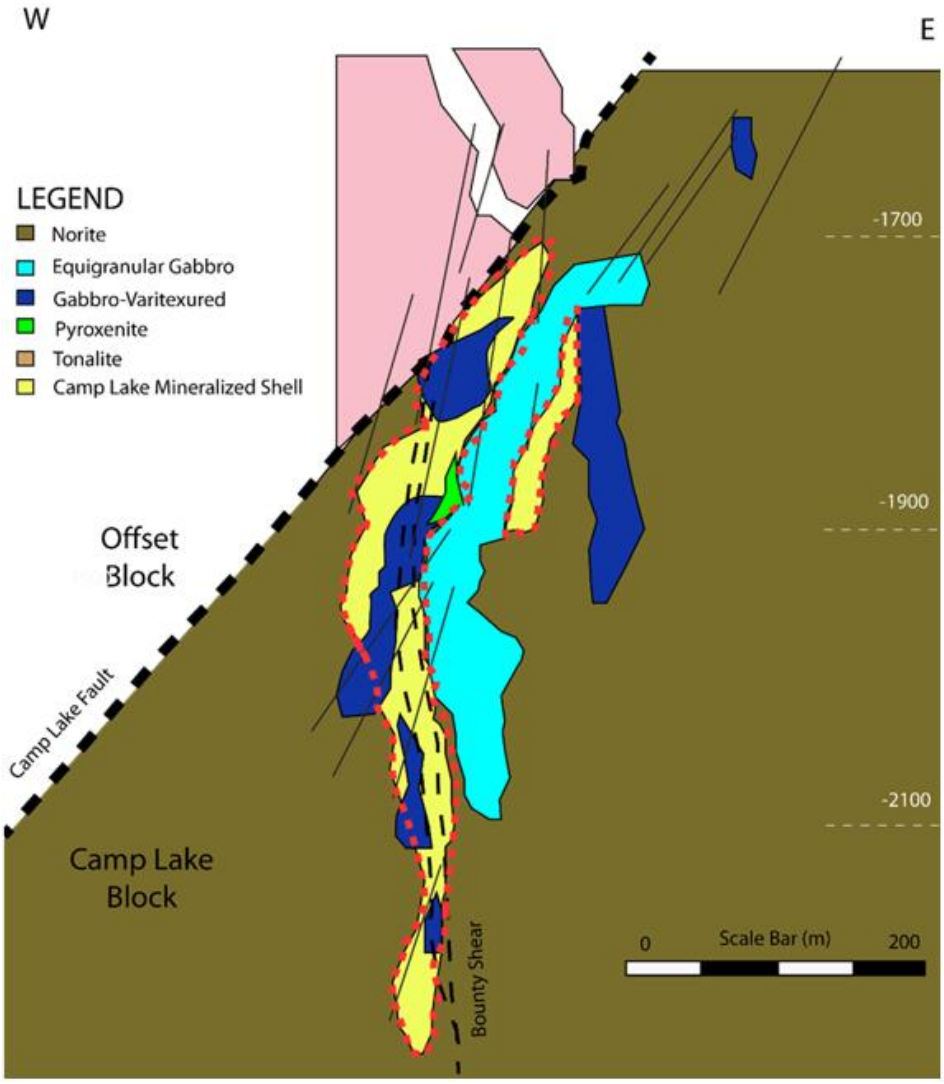

Figure 4.1 – Longitudinal sections showing Camp Lake mineralized zone, major rock types, and structures (Image courtesy of Lac Des Iles exploration department).

Almost all the rocks sampled from the Camp Lake Zone have undergone alteration, with intensity ranging from moderate to strong. Alteration commonly comprises tremolite-actinolite and chlorite, as well as plagioclase that has mostly been altered to sericite, with minerals displaying adcumulate textures and lacking uniform orientation. The majority of the rocks consist of gabbronorites, ranging from leucocratic gabbronorite to melanocratic gabbronorite, as well as some norites.

Figure 4.2– A) Varitextured gabbronorite at 1223.9 m, hole 22-712; B) Norite from 1249 m, hole 22-711.

Gabbronorites occur in two textural types, equigranular and varitextured (Fig. 4.2a). Equigranular samples show a relatively uniform grain size, with plagioclase, orthopyroxene, and clinopyroxene forming an interlocking mosaic. Varitextured gabbronorites display a heterogeneous grain-size distribution, where coarse-grained domains alternate with finer-grained or recrystallized patches, producing visible variations in the arrangement and relative proportions of plagioclase and pyroxenes.

Norites generally exhibit a massive texture, with occasional weak foliation defined by aligned plagioclase and orthopyroxene grains (Fig. 4.2b). Grain size is typically more uniform than in the varitextured gabbronorites, and clinopyroxene is less abundant or absent.

4.1.1 Gabbronorite

Due to the pervasive alteration that ranges from moderate to intense in almost all the selected samples, it was challenging to determine the original mineral proportions. Therefore, the CIPW-normative diagram was used to determine the mineralogical proportions and to better define the samples (Fig. 4.3).

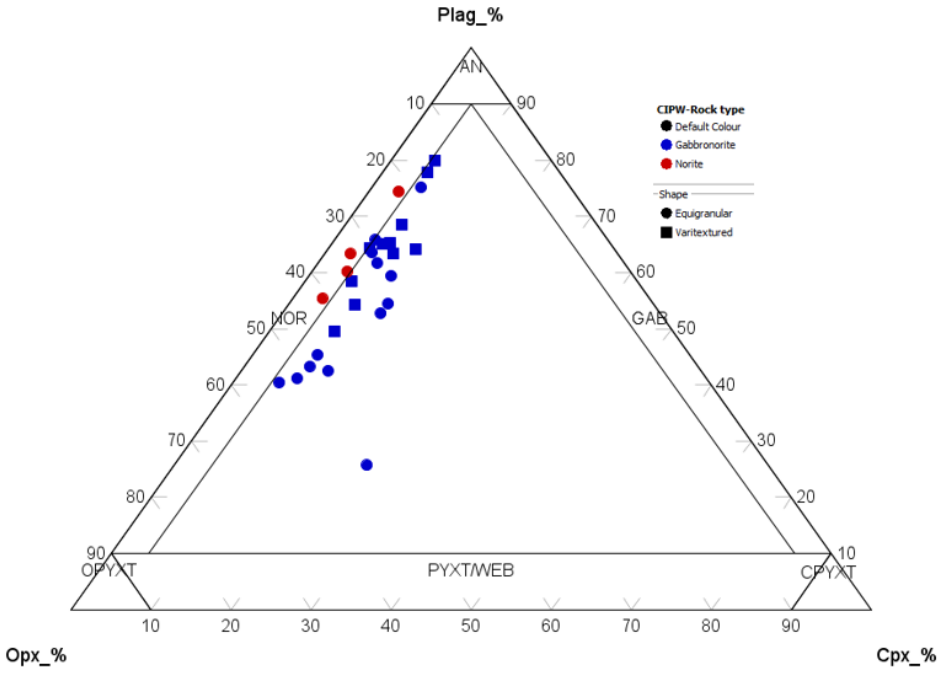

Figure 4.3 – CIPW Ternary diagram of orthopyroxene, clinopyroxene, and plagioclase normalized modal abundances for Camp Lake Zone rocks from this study (NOR: Norite, GAB: Gabbro, PYXT: Pyroxenite, WEB: Websterite, OPYXT: Orthopyroxenite, CPYXT: Clinopyroxene, Plag: Plagioclase.

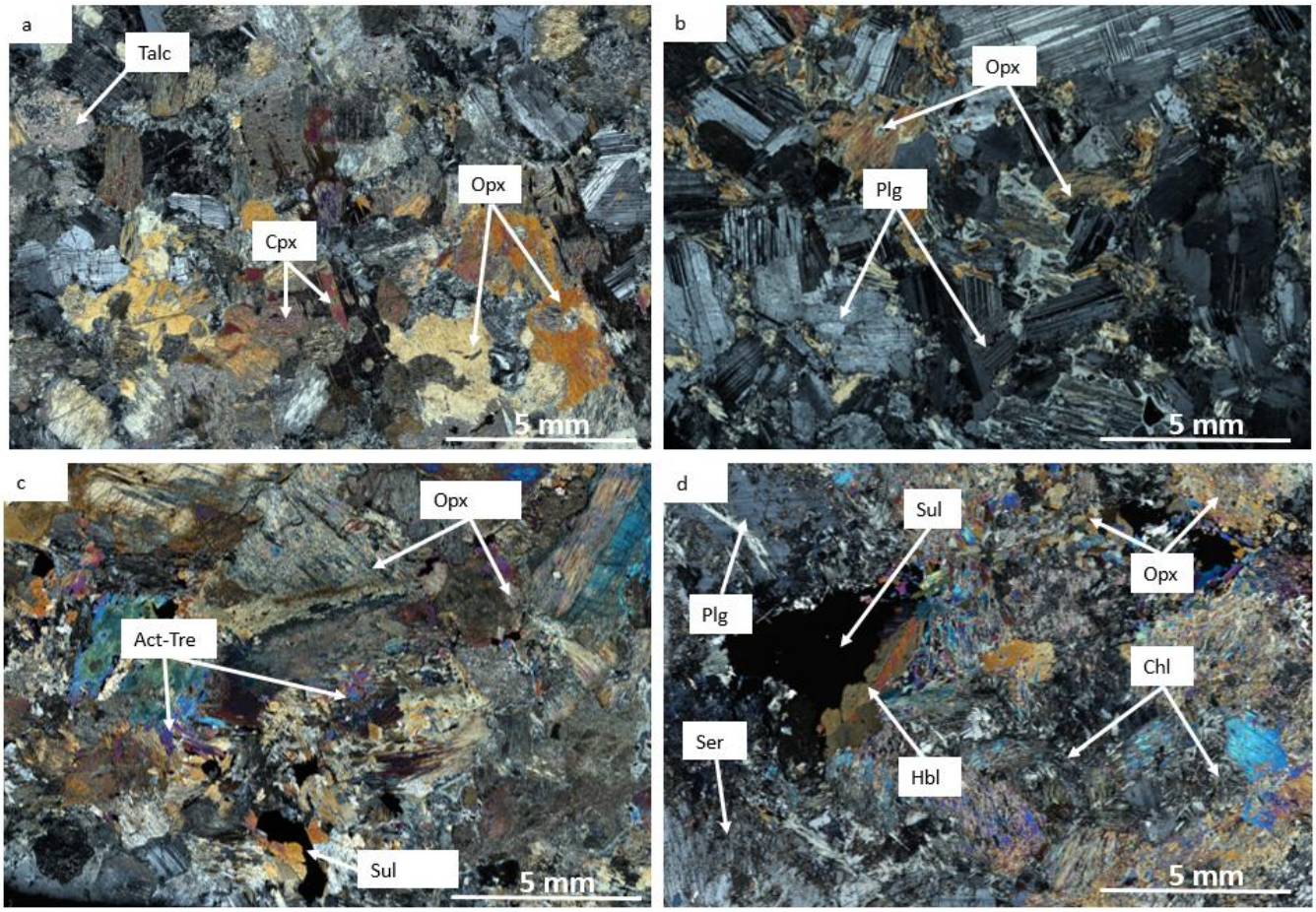

Figure 4.4 – Photomicrographs of gabbronorite in cross-polarized light of: a) clinopyroxene occurring as exsolution lamellae in orthopyroxene (Sample 22-711-012), b) Subhedral to anhedral grains of plagioclase with adcumulate texture (Sample 22-711-024), c) orthopyroxene and amphiboles with anhedral to subhedral forms (Sample 22-711-051), d) Seritization of plagioclase and uralitization of pyroxene (Sample 22-711-055). Cpx = clinopyroxene; Opx = orthopyroxene; Plg = plagioclase; Act= actinolite; Tre= tremolite; Hbl = hornblende; Chl = chlorite; Ser = sericite; Tlc = talc; Sul = sulfide.

The samples have adcumulate textures and are mainly composed of plagioclase (23□75%) and orthopyroxene (15-50%), with minor amounts of clinopyroxene (5□22%) occurring as exsolution lamellae in orthopyroxene (Fig. 4.4a, b). Hornblende, biotite, epidote and talc are present in trace amounts of less than 2% and appear with the sulfide minerals in interstitial phases (Fig. 4.4a). Moderate to intense uralitization of pyroxene is present in all the samples, as well as sericitization of plagioclase (Fig. 4.4c). The actinolite-tremolite crystals are well-developed, around clinopyroxene, along with pyroxene alteration by chlorite (Fig. 4.4c, d).

Plagioclase, varying from 23 to 75% in the modal abundance, is altered to sericite from moderate to strong based on the loss of ignition (LOI), which ranges from 1.96 for less altered rocks to 4.13 for more altered ones, and also to chlorite and epidote along the junctions between different grains and pyroxenes, as well as in fractured zones. The grain size varies from 0.1 to 5 mm with simple to polysynthetic twinning (Fig. 4.4.b).

The orthopyroxene exhibits anhedral to subhedral grains (0.1-4mm; Fig. 4.5a 22-712-016) and constitutes (50-15%) of the rock-forming minerals. The alteration of orthopyroxene occurs though the whole grain and sometimes at the edges and along the mineral fractures, with the

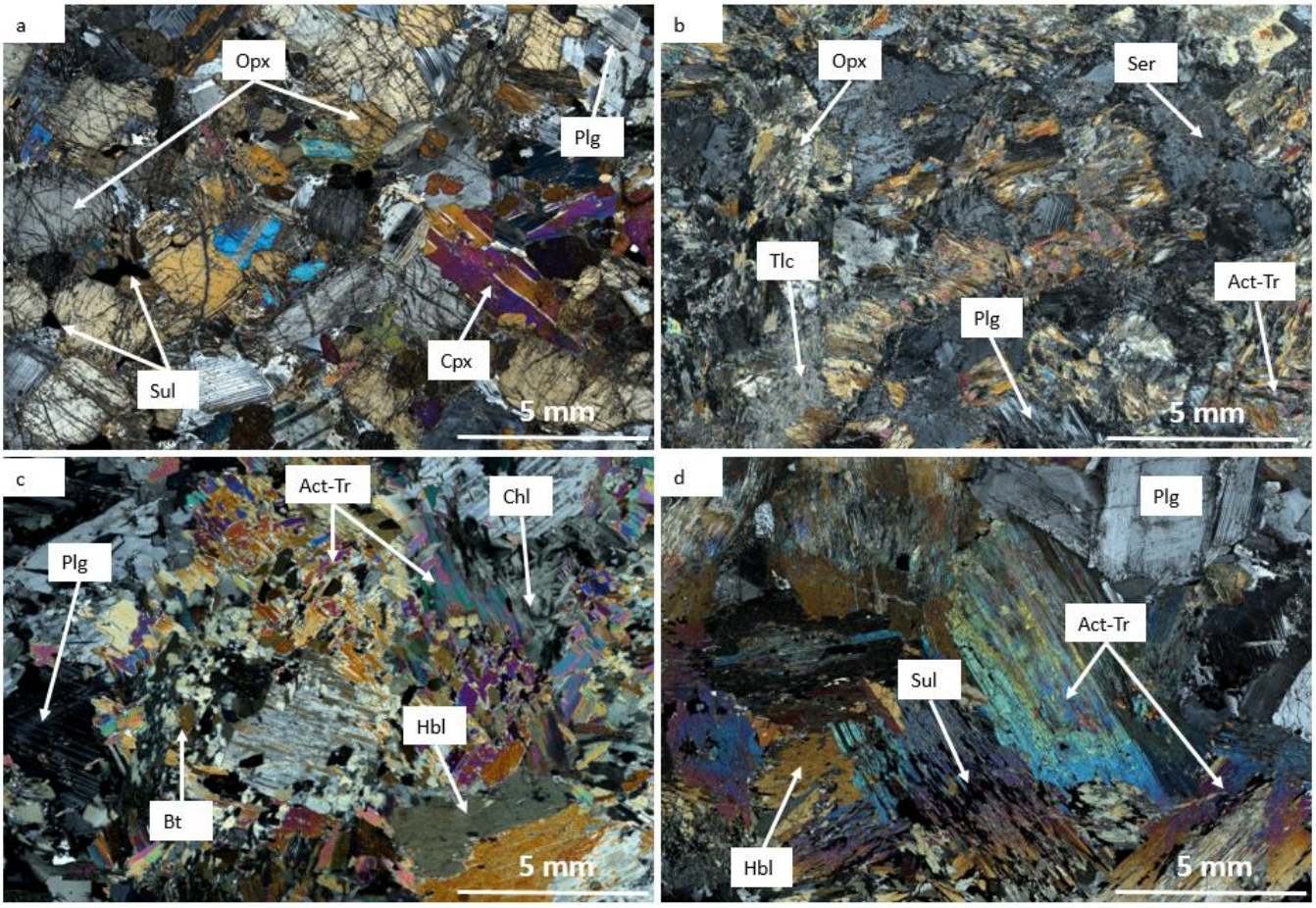

Figure 4.5– a) Weakly altered sample with dominant orthopyroxene and less clinopyroxene with minor plagioclase (Sample 22-712-016), b) Mix of subhedral granular altered pyroxene, hornblende, and plagioclase (locally altered by talc and epidote, Sample 22-712-001), c) Primary biotite and hornblende well-developed, secondary minerals such as chlorite and sericite. (Sample 22-711-022), d) hornblende, actinolite-tremolite with sulfide exolutions (Sample 22-711-029). Cpx = clinopyroxene; Opx = orthopyroxene; Plg = plagioclase; Hbl = hornblende; Chl = chlorite; Ser = sericite; Tlc = talc; Sul = sulfide.

majority of grains moderately to intensely altered to amphibole. The main products of pyroxene alteration are actinolite-tremolite, which constitute more than 90% of the pyroxene alteration, with minor traces of talc (Fig. 4.5b).

Hornblende and biotite are present in small quantities in the gabbronorite samples, representing up to 0.2% of the sample, and display only very slight alteration suggesting they may be primary (Fig. 4.5c, d). Hornblende, which appears as rims on actinolite and interstitially, is likely a primary phase initially surrounding clinopyroxene, with grain sizes ranging from 0.1 mm to 2 mm and shapes varying from subhedral to anhedral. Crystals of about 2 mm were observed. Biotite appears as slightly deformed laths up to 2 mm in length, as well as inclusions within orthopyroxene altered by tremolite-actinolite.

The sulfides present in the gabbronorite range from trace amounts up to ~5% and consist of typical magmatic assemblages including pyrrhotite, chalcopyrite, pentlandite, and pyrite, with minor magnetite. Pyrrhotite is the dominant sulfide phase (Fig. 4.6a, b; 22-711-037 & 712-055). The shapes of the sulfides vary from anhedral to subhedral; they range from disseminated to coarse grains with grain sizes from 0.1–3 mm and are associated silicates (Fig. 4.6). The edges of the sulfide blebs in contact with the primary igneous minerals are slightly rounded, indicating

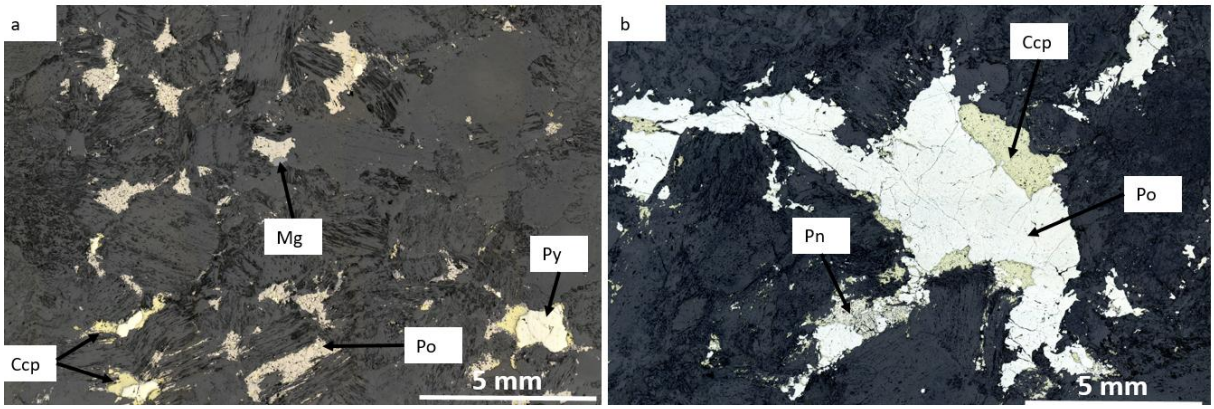

Figure 4.6– Reflected light Photomicrographs of common sulfides occurrences in gabbronorite: Figure a) Subpoikilitic sulfide is an even mix of pyrrhotite, intergrown and rimmed by chalcopyrite, pyrite with minor amounts of magnetite (Sample 22-711-037), b) Coarse sulfide grain typically composed of pyrrhotite with fine intergrowths of chalcopyrite and pentlandite in the interior and margins (Sample 22-712-055. Ccp = chalcopyrite; Po = pyrrhotite; Py = pyrite; Pn = pentlandite; Mg = magnetite.

equilibrium conditions, in contrast, the boundaries of the sulfides are interlocked with secondary minerals (such as amphibole and chlorite), indicating conditions of textural disequilibrium.

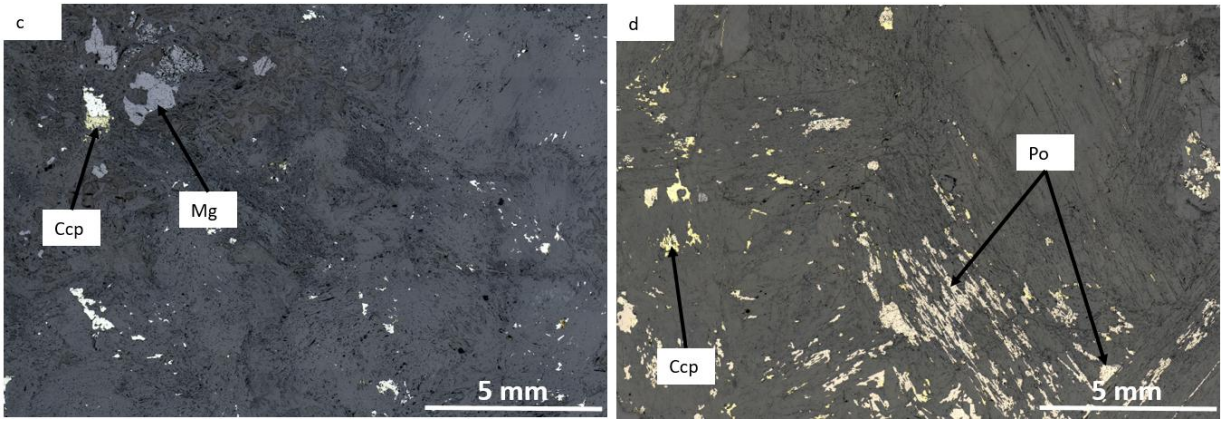

Figure 4.6 cont. – Reflected light photomicrographs of common sulfides occurrences in gabbronorite: c) Fine disseminated chalcopyrite, pyrrhotite and magnetite surrounding altered plagioclase and pyroxene (Sample 22-712-061), d) Medium to fine anhedral sulfide grains composed of chalcopyrite pyrrhotite with exolutions in silicate (Sample 22-711-029). Ccp = chalcopyrite; Po = pyrrhotite; Pn = pentlandite; Mg = magnetite.

4.1.2 Norite

As with the gabbronorite, it was also challenging to determine the original mineral proportions for the norite. Therefore, the CIPW-normative diagram was used, four samples fall within the norite field (Fig. 4.3). The samples have a massive texture and were sometimes weak foliated, with relatively homogeneous crystals ranging from fine to medium grains (Fig. 4.2b). Plagioclase is the most common silicate mineral in the norite, ranging in abundance from 50 to 70%. The plagioclase crystals are anhedral to subhedral, ranging from 0.1–3mm. Most of the crystals vary from equant to tabular forms (Fig. 4.7a), with almost no cryst.als exhibiting lath shapes, consequently they exhibit heterogeneous variation across the samples, indicating a significant variation in plagioclase composition. More than 50% of plagioclase grains exhibit simple or polysynthetic twinning with moderate to intense alteration, sometimes with minor to significant fractures within some grains filled with alteration minerals.

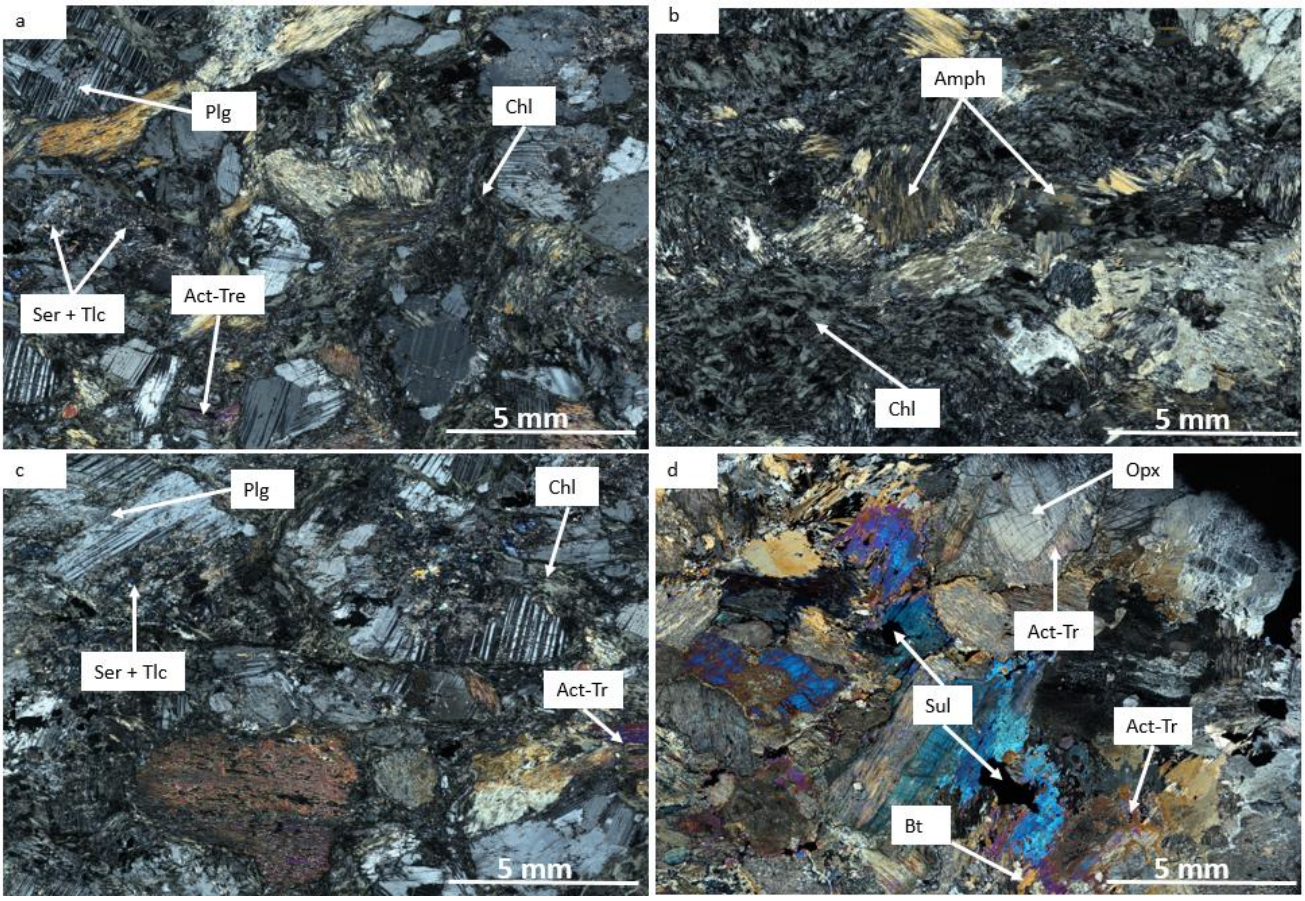

Figure 4.7 – Photomicrographs in cross-polarized light of common silicates occurrences in norite: a) Slightly variable to relatively homogeneous plagioclase and pyroxene sizes, with weak to moderate alteration for plagioclase and pyroxene (Sample 22-712-017), b) Moderate to strong chlorite uralitization of pyroxene, accompanied by chlorite alteration and sericitization of plagioclase (Sample 22-712-036), c) Plagioclase crystals with anhedral to subhedral shapes exhibit simple or polysynthetic twinning with significant sericite alteration. Additionally, some fractures, ranging from slight to significant, within certain grains are filled with alteration minerals (Sample 22-712-017), d) Subhedral to anhedral pyroxene crystals have undergone uralitization by actinolite-tremolite, with actinolite-tremolite zoning (Sample 22-712-041). Amph = amphibole; Opx = orthopyroxene; Plg = plagioclase; Hbl = hornblende; Chl = chlorite; Ser = sericite; Tlc = talc; Sul = sulfide.

In the four analyzed samples, only one sample had plagioclase altered to less than 20%, whereas in the others, the alteration could reach up to 90%, with crystals showing fractures filled with alteration minerals (Fig. 4.7).

The pyroxenes occur as subhedral to anhedral crystals, with occasionally elongated to tabular forms (Fig. 4.7a, d). Their size varies from 0.1–3mm, and generally, the crystals tend to be clustered together. The pyroxenes are dominantly orthopyroxene, up to 95% orthopyroxene, and about 5% clinopyroxene. Pyroxenes make up about 25–40% of the norite samples. The alteration

of orthopyroxene ranges from moderate to strong in all samples, sometimes showing deformation in samples where the alteration is more intensely, with chlorite and actinolite as the main alteration products (Fig. 4.7a). Clinopyroxene is present in all samples at proportions up to 5%. The crystal sizes of clinopyroxene range from 0.1–4mm with subhedral to anhedral shapes. However, due to alteration, it is sometimes difficult to determine their exact shapes as the alteration has given them irregular forms (Fig. 4.7c, d).

Biotite and hornblende are present in small quantities in the norite samples, representing up to 1–3% of the sample. Biotite appears as slightly deformed laths up to 2 mm in length, as well as inclusions within orthopyroxene altered by tremolite-actinolite. Hornblende, with subhedral to anhedral grains, are found as rims on actinolite, with a grain size ranging from 0.1 to 2 mm. It is likely a primary phase originally surrounding clinopyroxene (Fig. 4.7c, d).

Significant quantities of sulfides, reaching up to about 5%, are present in the norite. The observed sulfide assemblages are typical of common magmatic assemblages, including pyrrhotite, chalcopyrite, pentlandite, and pyrite. The sulfides appear in anhedral to subhedral forms, with grain sizes ranging from fine to coarse, from 0.1 to 3 mm (Fig. 4.8a). The sulfides are primarily found in the interstitial phases of silicate minerals, as anhedral granular masses (Fig. 4.8b). Sulfide minerals are frequently observed as aggregates composed of pyrrhotite, chalcopyrite, and pyrite subhedral to anhedral grains (Fig. 4.8a). In general, the sulfides display pronounced textural heterogeneity and phase intergrowths, consistent with multi-stage crystallization. For example, Figure 4.8b illustrates a sulfide-enriched domain, mainly composed of pyrite and chalcopyrite, embedded within a silicate matrix. Trace amounts of magnetite approximately 0.3% occur in the gangue as very finely disseminated grains or at boundaries between sulfide and silicate grains.

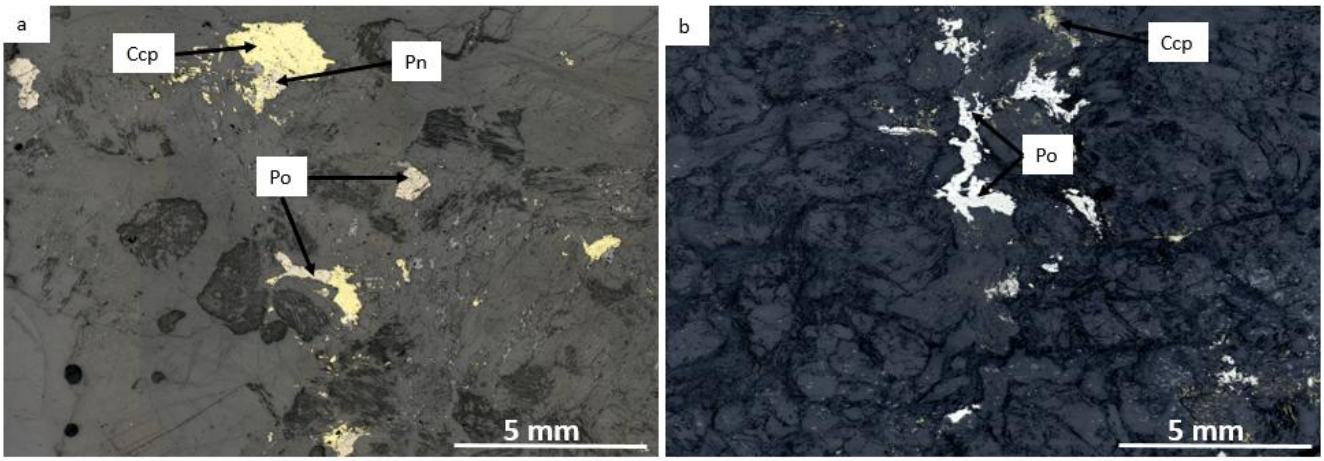

Figure 4.8 – Reflected light Photomicrographs of common sulfides occurrences. a) typical of common magmatic assemblage in norite, including pyrrhotite, chalcopyrite, pentlandite (Sample 22-711-041), b) pyrrhotite and chalcopyrite present in the interstitial phases of silicate minerals (Sample 22-712-017).

4.2 Platinum-group minerals

Two hundred and ten PGM grains were identified during SEM analyses on polished thin sections (Table 4.1). Following this analysis, they were grouped by element affinity, resulting in six PGM groups, ranked in decreasing order of abundance: (Pd-Pt) Te (Tellurides: Moncheite, Kotulskite), (Pd-Pt) As (Arsenides: Sperrylite, Palladoarsenide), (Pd-Pt) BiTe (Bismuth-Tellurides: Michenerite, Merenskyite), (Pd-Pt) S (Sulphides: Braggite, Cooperite), (Pd-Pt) Sb (Antimonides: Sudburyite, Geversite, Stibiopalladinite), and (Pd-Pt) Al (rare phases), with platinum being the only native element observed in the polished sections of the analyzed samples. Native platinum is dominant in all samples and is present in almost all observed sulfide assemblages, except for two samples. The (Pd-Pt) Te group is the most dominant across all samples, while the (Pd-Pt) Al group is the least represented.

The sizes of the PGM were broadly homogeneous across the analyzed samples, ranging from 0.1 to approximately 30 microns for the largest grain analyzed (Fig. 4.9a, b). To establish the relationships between sulfides and PGM, the sulfide or silicate in which the PGM was located was described, except in cases where multiple PGM were found in the same sulfide or silicate, where they were reported only once (Fig. 4.9). From the SEM analyses, the majority of PGMs were found either in silicates located near sulfides or at the margin between sulfides and silicates, or in sulfides (Fig. 4.9a, c).

Table 4.1 – Samples selected for SEM and PGM characterization. Samples from the Camp Lake Zone, taken from drill holes 22-711 and 22-712. Abbreviations: Ccp = chalcopyrite, Mg = magnetite, Pn = pentlandite, Po = pyrrhotite, Py = pyrite.

Sample	Pd (ppm)	Assemblage
22-711-041	6.96	Ccp-Po-Pn-Py+Mg
22-712-044	5.06	Po-Ccp-Py+Mg
22-712-016	4.86	Ccp-Po-Pn-Py+Mg
22-711-055	4.67	Po-Ccp-Py+Mg
22-712-017	4.4	Py-Ccp-Po+Mg
22-711-045	4.38	Po-CCp-Pn-Py
22-711-029	3.67	Po-Ccp-Py
22-711-032	3.36	Ccp-Po-Py
22-712-055	3.19	Po-CCp-Pn-Py
22-711-031	3.11	Po-Ccp

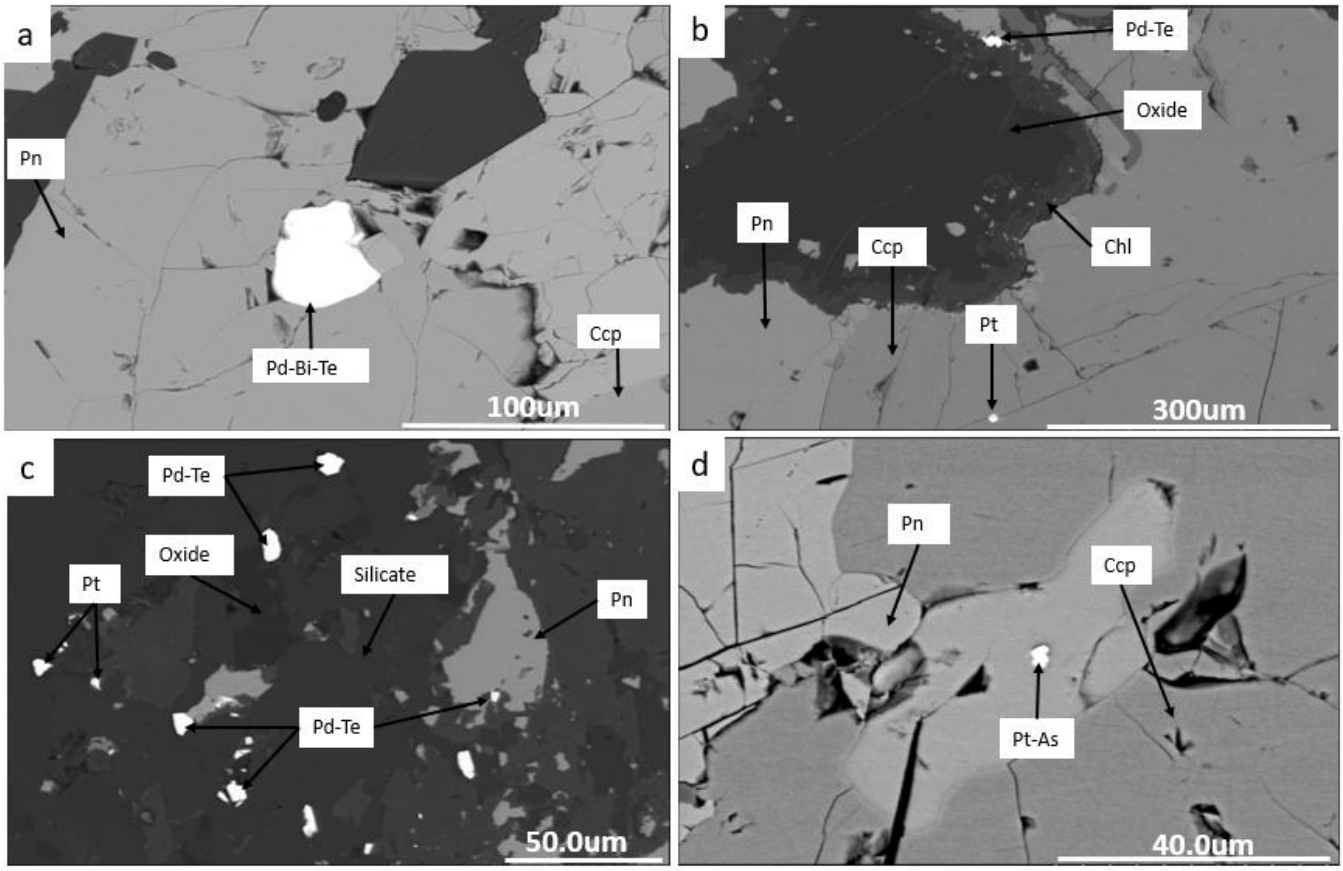

Figure 4.9 – SEM images of platinum group minerals: a, b, c, Backscattered electron images showing representative mineralization of PGMs in the Camp Lake Zone. The host material is gabbronorite and norite with alteration minerals (chlorite, actinolite-tremolite, talc), (d) Gabbronorite (sample 22-712-044) showing the presence of PGM (Pt-As) in inclusion with pentlandite and chalcopyrite at the margins. Pn = pentlandite; Ccp = chalcopyrite; Pt = platinum; Pt-As = platinum–arsenic mineral; Pd-Bi-Te / Pd-Te = palladium–bismuth–tellurium and palladium–tellurium minerals; Chl = chlorite.

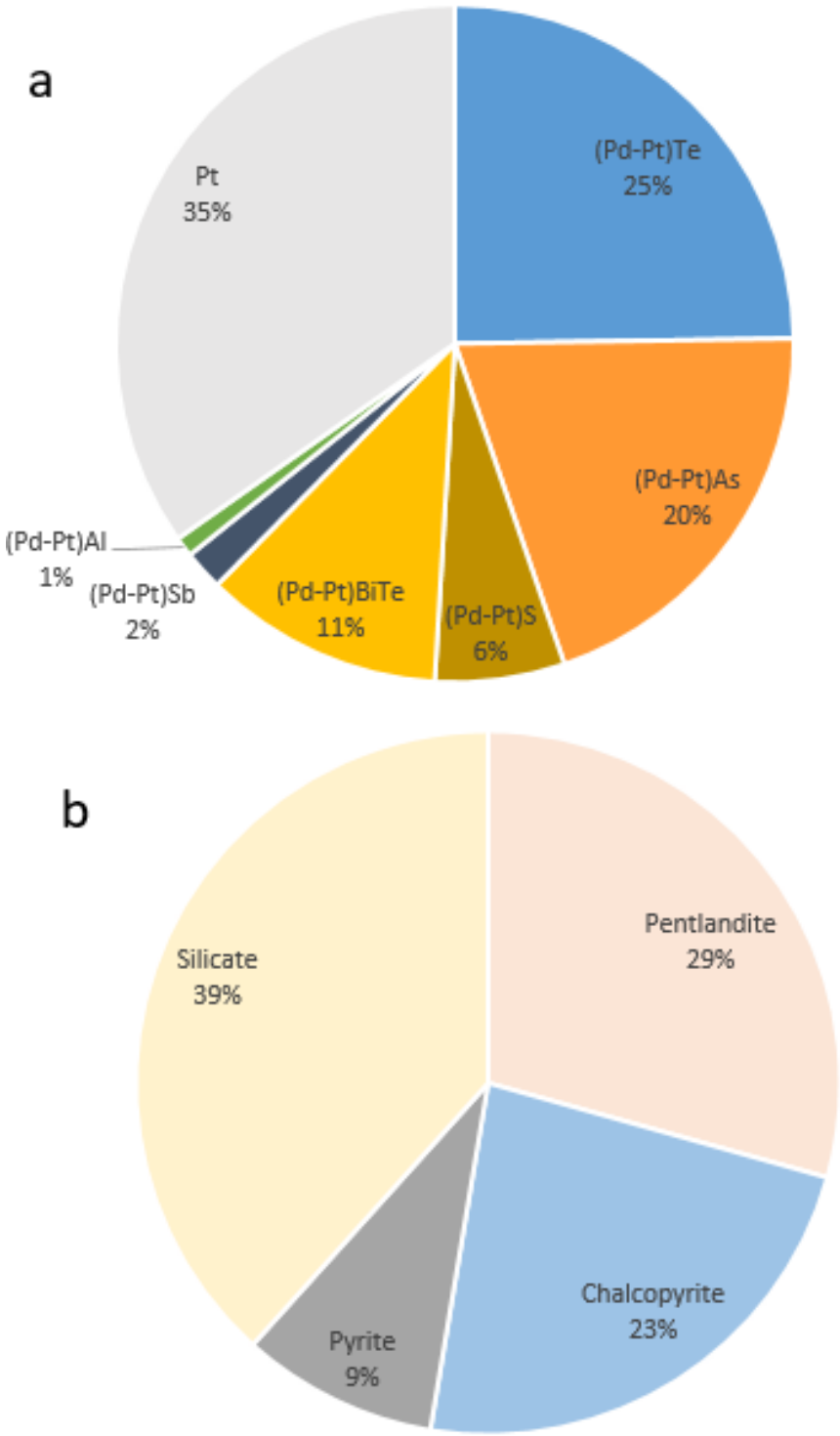

Figure 4.10 – a. Pie chart showing abundance of different PGM assemblages based on number of grains identified. b. Statistical diagram of textural relationships between PGM-Base Metals Sulfide (BMS)-Silicates.

4.3. Whole rock geochemistry

Al_2O_3 contents range from 7% to 22% and decrease systematically with increasing MgO (Fig. 4.11). This trend is observed in both lithologies, although norites display greater scatter at lower MgO. Na_2O values (0.5–2.5%) also decrease gradually as MgO increases. CaO shows a similar behavior, ranging from 5.5% to 11.5% and declining with higher MgO. In contrast, Fe_2O_3 increases steadily from 2% to 17% with increasing MgO, a trend that is more pronounced in high-MgO norites. MnO (0.075–0.225%) likewise shows a positive correlation with MgO.

The gabbronorites display a general enrichment in light rare earth elements (LREE) with relatively flat heavy rare earth element (HREE) patterns, whereas the norites show broadly similar profiles with slightly lower overall concentrations and flatter trends (Fig. 4.12a). Consequently, the LREE and HREE are similar between these two rock types. The La/Sm_N values in the norite range from 2.58 to 7.54, whereas the Gd/Yb_N values range from 0.70 to 0.88. In contrast, in gabbronorite, the La/Sm_N values range from 1.29 to 7.76, and the Gd/Yb_N values range from 0.56 to 1.49. Negative Nb anomalies are present in all samples and are typically quite pronounced. Positive Eu anomalies are present in all samples except for one norite sample that shows a slight negative Eu anomaly, also negative Zr-Hf anomalies present in most samples. Figure 4.12b displays the full suite of primitive-mantle–normalized trace-element curves for all gabbronorite and norite samples, together with the mean profile for each rock type. The individual curves are plotted collectively to show the complete range of variability across the analyzed elements, while the averaged profiles offer a clear visual reference for the overall trend within each group.

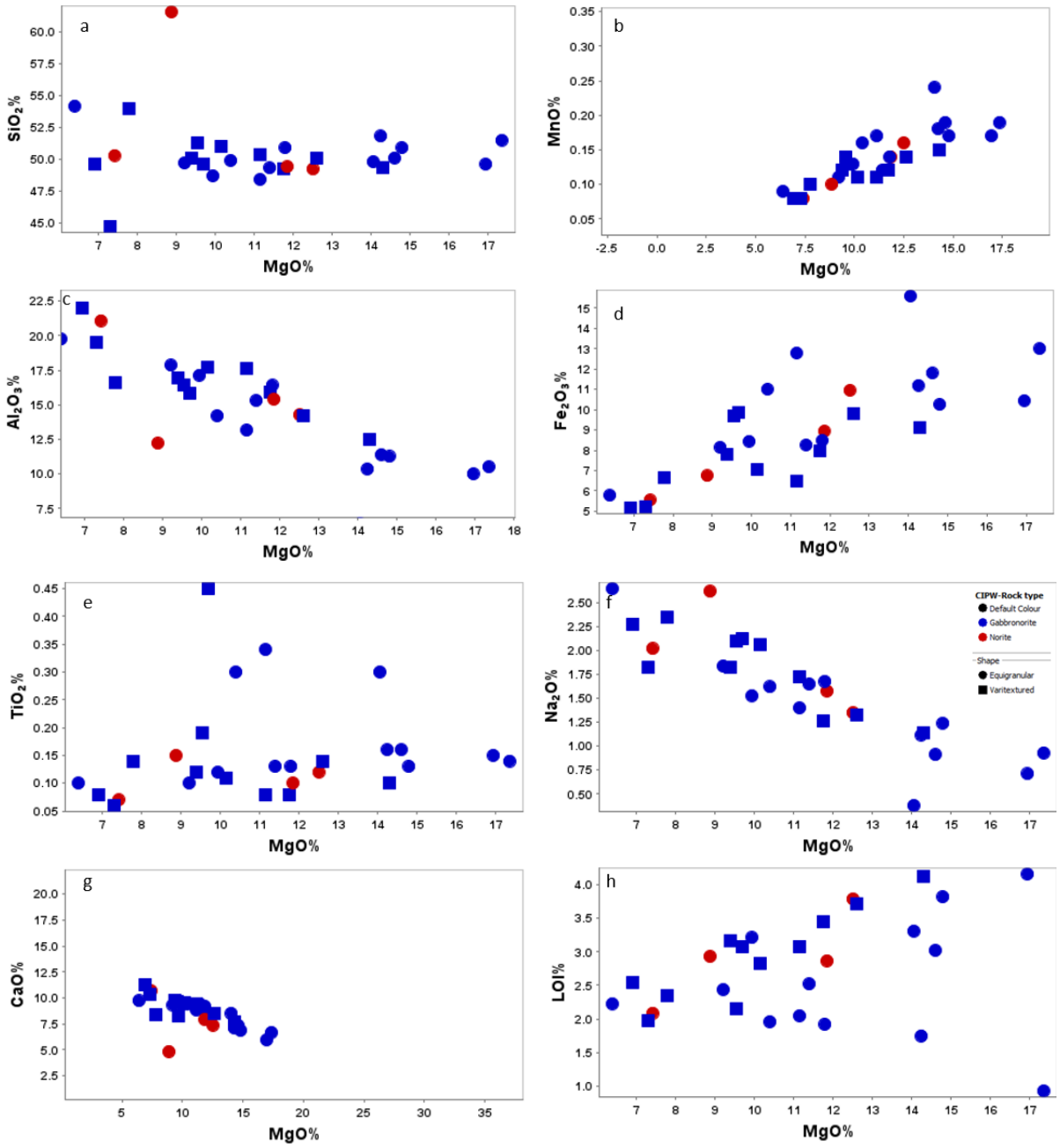

Figure 4.11 – Plots of selected major and minor element oxides as a function of MgO (wt %) showing the composition of norite and gabbronorite samples from the Camp Lake Zone.

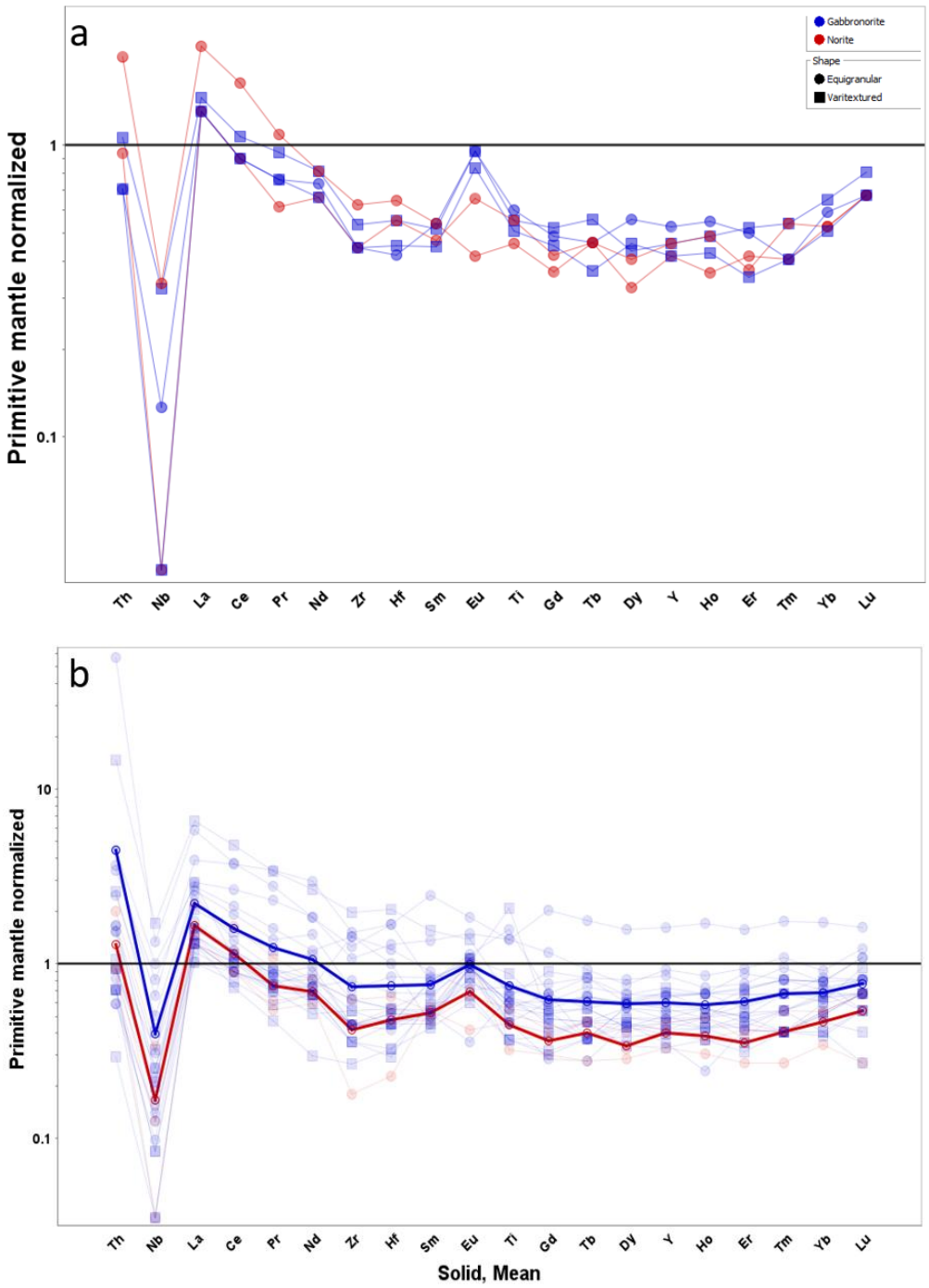

Figure 4.12 – a) Primitive mantle-normalized plots of representative samples of gabbronorite and norite from Camp Lake Zone. b) Complete set of primitive mantle–normalized spider diagram for all gabbronorite and norite samples, along with the mean profile calculated for each rock type. The individual sample patterns are shown together to illustrate the full range of variability across the analyzed elements, and the averaged curves provide a visual reference for the central tendency of each group. Normalizing values from Sun and McDonough (1989).

4.4. Sulfur isotopes

Twelve samples were selected to represent the two rock types (gabbronorite and norite), together with a range of sulfide assemblages and alteration styles. In hole 22-711, sulfur contents range between 0.1% and 0.5%, reaching a maximum around 1250 m in depth. For borehole 22-712, although only three samples were taken, sulfur contents remain stable at ~0.4%.

The associated mineral assemblages include combinations of chalcopyrite, pyrite, pyrrhotite, magnetite, and pentlandite. Sulfur isotopic results, expressed in $\delta^{34}S$ ‰ relative to the VCDT standard, range from +0.3 ‰ to -1.1 ‰ (Table 4.2). For example, a pyrite sample at 1014.85 m in hole 22-711 has a $\delta^{34}S$ value of +0.3 ‰, whereas a pyrrhotite sample at 1140.49 m shows -1.0 ‰. At 1215.39 m, two chalcopyrite samples record $\delta^{34}S$ values of -0.8 ‰ and -0.7 ‰. At 1249.11 m, a chalcopyrite sample shows -0.9 ‰, while a pyrrhotite sample at the same depth has -0.7 ‰. Additional values include -0.4 ‰ for pyrite at 1279.29 m and chalcopyrite at 1308.64 m. In

Table 3.2 – Results of sulfur isotope analysis.

Sample ID	Depth (m)	Rock type	Assemblage	Analysed Mineral	$\delta^{34}S$ ‰ (VCDT)
22-711-010	1014.85	Gabbronorite	Ccp-Py-Mg	Pyrite	0.3
22-711-029	1140.49	Gabbronorite	Ccp-Pn-Po	Pyrrhotite	-1.0
22-711-037	1215.39	Gabbronorite	Ccp-Po-Py-Pn-A	Chalcopyrite-A	-0.8
22-711-037	1215.39	Gabbronorite	Ccp-Po-Py-Pn-B	Chalcopyrite-B	-0.7
22-711-041	1249.11	Gabbronorite	Ccp-Po-Py-Mg	Chalcopyrite	-0.9
22-711-041	1249.11	Norite	Ccp-Po	Pyrrhotite	-0.7
22-711-045	1279.29	Gabbronorite	Ccp-Po-Py	Pyrite	-0.4
22-711-048	1308.64	Gabbronorite	Ccp-Po	Chalcopyrite	-0.4
22-712-017	881.57	Norite	Ccp-Po-Pn-Py	Pyrite	-0.1
22-712-050	1193.14	Gabbronorite	Ccp-Py	Pyrite	-0.2
22-712-055	1224	Gabbronorite	Ccp-Py	Chalcopyrite	-0.9
22-712-055	1224	Gabbronorite	Ccp-Po-Py	Pyrite	-1.1

borehole 22-712, samples taken between 881.57 m and 1224 m yield $\delta^{34}S$ values ranging from -0.1 ‰ to -1.1 ‰ across pyrite and chalcopyrite.

4.5 Geochronology

The results of the ID-TIMS U-Pb dating on a coarse-grained gabbro (22-711-gc-001) are presented in Table 4.3. The photomicrographs in transmitted light of representative zircons, selected for pretreatment and analysis, are shown in Figures 4.13a and b. The results in the form of a Concordia U-Pb diagram are displayed in Figure 4.13c.

The processing of this sample yielded a moderate amount of weakly magnetic heavy mineral concentrates, comprising a variety of zircon grains ranging from colorless to medium brown, and from prismatic to slightly rounded shapes. Most of the recovered zircons were transparent, whereas a subpopulation shows spots with hematite coatings. Three of the highest quality and clearest zircon grains were selected for chemical abrasion and further analysis (Fig. 4.13b).

The analytical results of the zircon fractions Z1 to Z3 are presented in Table 4.3 and Figure 4.13c. All fractions reveal low to moderate uranium concentrations (~160–270 ppm) and a uniformly high Th/U ratio (~0.73-0.83), characteristic of fractionated mafic magmas. The U-Pb data from these single grain analyses cluster around concordia (-0.2 to +0.4% discordance), with nearly constant $^{207}Pb/^{206}Pb$ ages between 2690.5 and 2690.6 Ma. Collectively, these data produce a weighted mean $^{207}Pb/^{206}Pb$ age of 2690.56 ± 0.80 Ma, interpreted as a robust estimate of the timing of emplacement and primary crystallization of the Camp Lake Zone. Complete results of geochronology analyses are provided in Appendix III.

Table 4.3 – Zircon U-Pb isotopic data for coarse gabbronorite from the Camp Lake Zone.

Fraction	Description	U (ppm)	Pb^{T} (Pg)	Pb_c (Pg)	Th/U	$^{206}Pb/^{204}Pb$	$^{206}Pb/^{238}U$	±2σ	$^{207}Pb/^{235}U$	±2σ	**Ages (Ma)**						
											$^{207}Pb/^{206}Pb$	±2σ	$^{207}Pb/^{235}U$	±2σ	$^{207}Pb/^{206}Pb$	±2σ	Disc(%)
22-711-GC-001*																	
Z1[§]	1 clr, cls, el, partly fctd short pr	174	219.16	5.12	0.831	2281	0.519035	0.000983	0.184136	0.000167	2695.1	4.2	2692.5	2.1	2690.5	1.5	-0.2
Z2[†]	1 cls, skel, frag	270	166.22	1.10	0.732	8125	0.516121	0.001036	0.184148	0.000166	2682.7	4.4	2687.2	2.3	2690.6	1.5	0.4
Z3[†]	1 clr, cls, skel, frag	159	199.89	0.45	0.817	23372	0.518321	0.000969	0.184152	0.000145	2692.1	4.1	2691.2	2.2	2690.6	1.3	-0.1

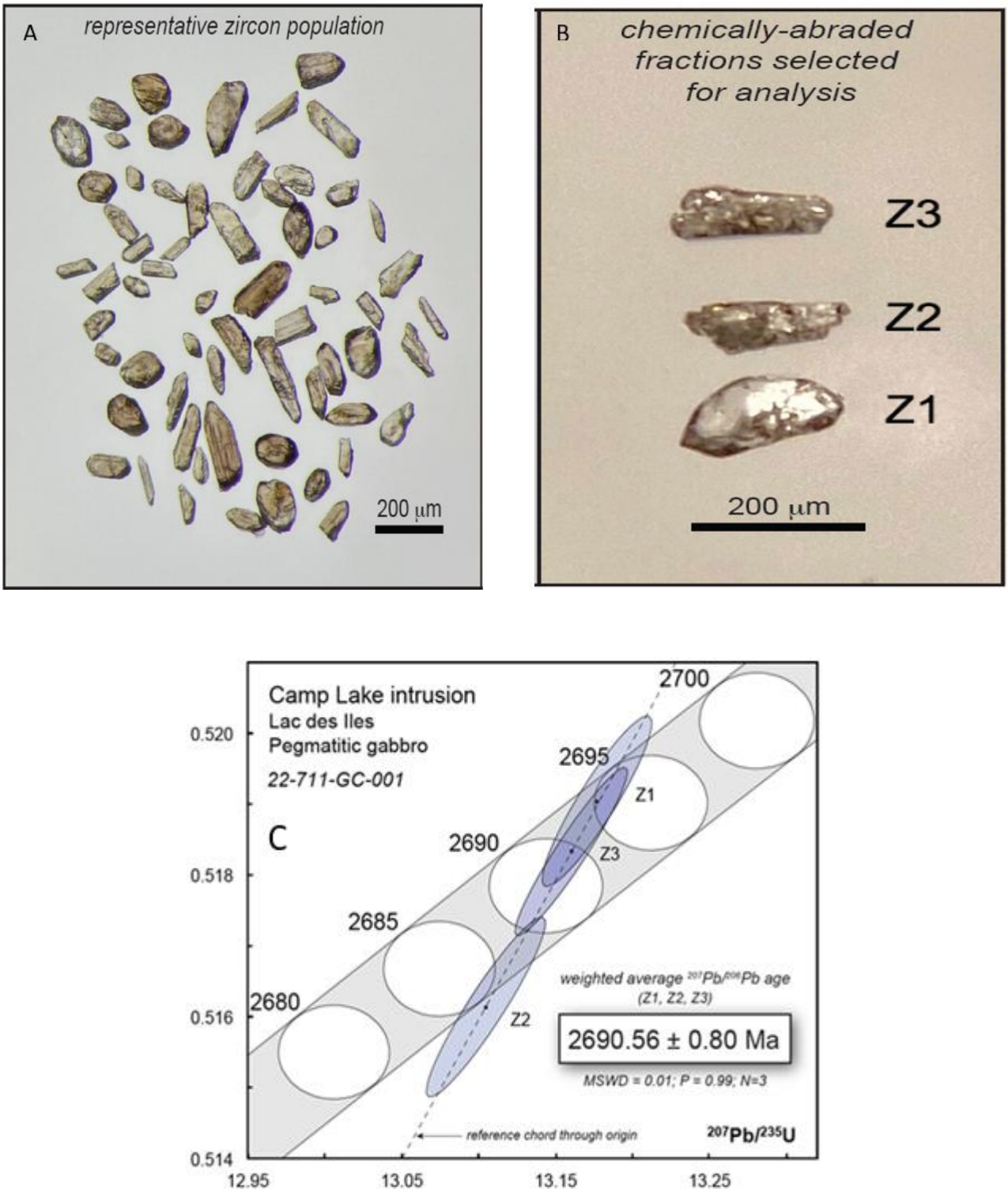

Figure 4.13– A) Representative zircon population B) analyzed fractions, C) Concordia diagram showing analytical results and age for Camp Lake Zone gabbro sample.

4.6 Neodymium isotopes

Neodymium isotopic analysis was conducted on ten samples, with results presented in Table 4.4. The samples were selected to represent the two main rock types, varying palladium concentrations, and differences in the concentration and distribution of rare earth elements.

Samples originated from drill holes 22-711 and 22-712, which exhibit low geochemical variability, allowing for more consistent and representative analytical results. Isotopic ratios of $^{143}Nd/^{144}Nd$ and $^{144}Nd/^{145}Nd$ were measured (full results are provided in Appendix IV), and εNdt values were calculated using an age of 2690 ± 0.80 Ma, determined through the geochronological analysis conducted in this study following the method described by DePaolo (1981). The εNd values range from +0.30 to +1.12. No systematic variability was observed among the samples calculated at age of 2690 ± 0.80 Ma in either drill hole, suggesting isotopic homogeneity within each borehole.

Table 4.4 – εNd results for samples from Camp Lake Zone.

Sample number	Depth(m) from	Depth(m) to	Nd (ppm)	Sm (ppm)	εNd
22-711-005	951.71	951.84	2.736	0.8431	0.509380441
22-711-022	1068.45	1068.61	1.124	0.2846	0.329423388
22-711-032	1165.65	1165.8	1.578	0.3344	0.710315595
22-711-037	1215.23	1215.39	2.834	0.6802	0.296919604
22-712-001	501	501.2	1.172	0.3136	0.684867569
22-712-005	700.1	700.25	0.9932	0.2474	1.002701175
22-712-017	881.47	881.57	0.7698	0.1885	1.124471109
22-712-044	1147.88	1148	1.845	0.4449	0.663755743
22-712-048	1223.9	1224	0.5022	0.1271	0.525309638
22-712-061	1286.08	1286.19	2.922	0.5316	0.751787133

Chapter 5 - Discussion

The Camp Lake Zone of the Lac des Iles Complex is one of three main zones of the South Lac Des Iles complex Complex (SLDIC). The three zones (Roby, Offset, and Camp Lake) are divided by two E-NE faults, known as the Offset and Camp Lake faults (Smith et al., 2024; Peterzon, 2025; Fig. 5.1). At 1.8 km depth, the Camp Lake Zone is the deepest part of the SLDIC.

Samples were collected with the aim of addressing two primary objectives: to characterize the Camp Lake Zone and to compare it with the Roby and Offset zones. Using petrography, whole rock geochemistry, geochronology, and radiogenic and stable isotopes, this chapter will discuss the characteristics of the Camp Lake host rocks and their relationship with the rest of the SLDIC.

5.1 Geochronology

A U-Pb TIMS zircon crystallization age of 2690.56 ± 0.80 Ma was obtained for the emplacement of the Camp Lake Zone (Fig. 5.1). The three zircon grains analyzed (Fig. 4.14) exhibit minimal discordance (–0.2% to +0.4%), moderate uranium concentrations (160–270 ppm), and elevated Th/U ratios (0.73–0.83), features that are characteristic of zircons crystallized from differentiated mafic magmas (Pietranik et al., 2022).

Comparable U-Pb zircon ages have been reported for other major intrusions of the Lac des Iles Complex: 2689.0 ± 1.0 Ma for the Roby and Offset zones (Stone, 2010); 2687.0 ± 1.6 Ma for the North Lac Des Iles Complex; 2690.59 ± 0.77 Ma for the Legris Lake intrusion (Bain et al., 2023); and 2689.9 ± 0.7 Ma for the Dog Lake intrusion (Bain et al., 2023). Collectively, these ages fall within a narrow range of 2688–2691 Ma, suggesting that the intrusions were emplaced during a single, regionally extensive magmatic event. The new age for the gabbronorite series of the Camp Lake Zone falls within this range and is within the error of the age for the Roby and Offset zones.

This time window corresponds to the 2.696–2.690 Ga accretionary event (Stone, 2010), which is associated with the tectonic amalgamation of the Wawa-Abitibi and Quetico terranes. The new age for the Camp Lake Zone confirms its temporal equivalence with the other major intrusions of the Lac Des Iles Complex and strongly supports its inclusion in the same magmatic episode responsible for the broader Lac Des Iles intrusive suite. This highlights a narrow range in the age of the mafic intrusions of the complex and underscores the regional significance of the 2.696–2.690 Ga magmatic activity.

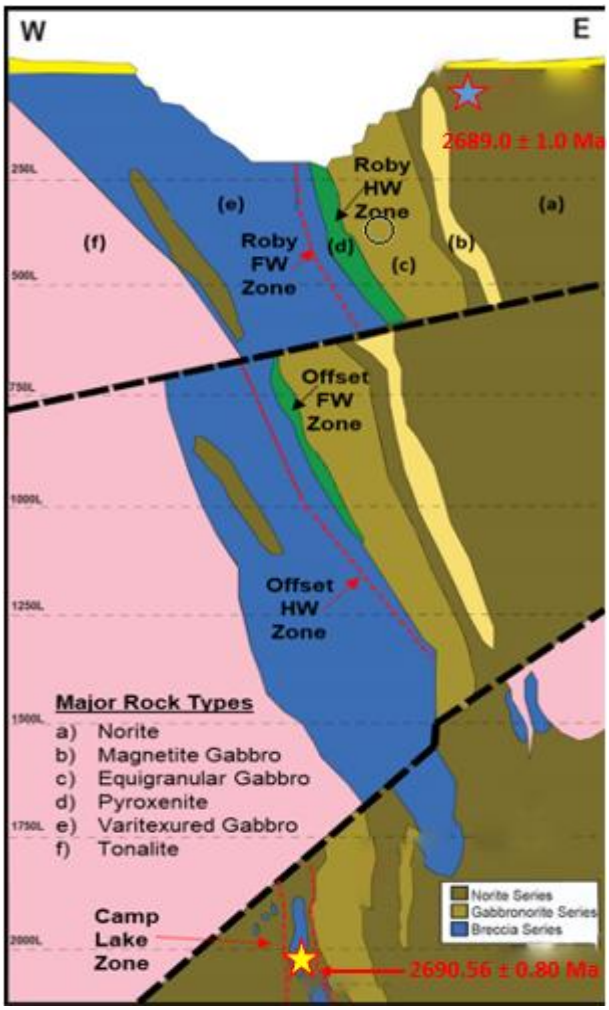

Figure 5.1 – Cross section of geological domains of the Roby, Offset, and Camp Lake Zone lithologies, looking north of the South Lac Des Iles Complex. The stars represent the areas where samples were collected for geochronology purposes (modified from Impala Canada, 2024).

5.2. Geological Characteristics and Alteration Processes in the Camp Lake Zone

The mineralogical and textural characteristics of the Camp Lake Zone reflect a combination of primary magmatic features and extensive post-magmatic modification. The dominance of plagioclase and orthopyroxene (Fig. 4.4), together with the coexistence of equigranular and varitextured gabbronorites, indicates crystallization from an evolved gabbronoritic magma and suggests local variations in cooling rates and magma replenishment. Similar textural variability has been documented in other mafic intrusive systems where dynamic magma chamber processes, including recharge and in situ crystallization, generate heterogeneous cumulate frameworks (Ahmed, 2022). These features are broadly comparable to those observed in the Roby and Offset zones, reinforcing the interpretation of a shared magmatic lineage within the SLDIC.

Within this primary framework, disseminated sulfides, mainly pyrrhotite, chalcopyrite, pentlandite, and minor pyrite occur as interstitial grains with anhedral to subhedral shapes (Fig. 4.6). Their intergrowth textures and close association with intercumulus silicates (Fig. 4.7d), indicate crystallization from a magmatic sulfide liquid under slow cooling conditions, consistent with the behavior of sulfide liquids in other mafic intrusions. Comparable textures have been reported in recent studies of intrusion-related magmatic systems, where sulfide droplets become trapped between growing silicate minerals during late-stage crystallization (Ahmed, 2022). The similarity between Camp Lake and the Roby and Offset zones suggests that the primary sulfide assemblage across the SLDIC formed under broadly comparable magmatic conditions.

Superimposed on these magmatic features is a significantly stronger hydrothermal overprint than that observed in the other zones of the SLDIC. Alteration intensities ranging from 5 to 90% and the pervasive replacement of orthopyroxene by actinolite–tremolite reflect extensive fluid–rock interaction under greenschist-facies conditions (Šegvić et al., 2022). Recent work on mafic intrusions has shown that such high-temperature alteration commonly develops during cooling, as hydrothermal fluids circulate through fracture networks and grain boundaries (Pochon et al., 2023). The concentration of alteration along

microstructural weaknesses at Camp Lake is consistent with models of short-lived but intense hydrothermal circulation around cooling intrusions (Abbey et al., 2024). Compared with the Roby and Offset zones, where alteration tends to be more localized, the Camp Lake Zone represents a more extensively modified end-member within the intrusive complex.

5.2.a. Assessment of hydrothermal alteration and reconstruction of pre-alteration mineralogy

Alteration intensity does not follow a simple lithological pattern. Although varitextured gabbronorites commonly show patchy recrystallization, the most altered sample in the dataset is an equigranular gabbronorite. Because alteration style varies at the thin-section scale, pre-alteration mineralogy was reconstructed using preserved igneous domains rather than lithology alone.

Primary minerals were identified where grains retained euhedral to subhedral outlines, straight or gently curved boundaries, polysynthetic twinning in plagioclase, and coherent grain-size relationships. Exsolution lamellae were rare and not used as diagnostic criteria. Reconstructed mineralogy relied on pseudomorphic replacement relationships, including plagioclase → sericite ± epidote, orthopyroxene → actinolite–tremolite ± chlorite ± minor talc, and clinopyroxene → amphibole ± chlorite. No olivine was observed.

Reconstruction followed a consistent workflow: (1) estimation of observed modal abundances, (2) identification of secondary minerals and their primary precursors, (3) evaluation of replaced volumes using grain outlines and textural continuity, (4) reassignment of replaced volumes to primary minerals, and (5) renormalization to 100%. Reliability is highest in samples with well-preserved igneous textures and lowest in strongly amphibolitized domains.

5.2.b. Applicability and limitations of CIPW norms

Given the pervasive alteration, it was necessary to evaluate whether whole-rock major-element chemistry remained sufficiently robust to support CIPW normative

calculations. CIPW norms were used only to approximate the primary igneous mineral assemblage and not to infer melt compositions, as the method assumes an anhydrous, unaltered system.

Alteration can redistribute CaO, MgO, FeO, and Na_2O, potentially affecting normative proportions. However, comparison between the most altered sample (22-712-039; LOI = 4.16) and the least altered sample (22-712-016; LOI = 0.93) shows strong internal consistency in normative plagioclase and pyroxene proportions. In the most altered sample, plagioclase represents 37.37% and pyroxenes 55.00%; in the least altered sample, plagioclase represents 38.74% and pyroxenes 55.30%. This close correspondence demonstrates that major–element chemistry retains sufficient integrity despite variable modification, validating the cautious use of CIPW norms as a complementary tool to petrographic observations. See Appendix V for the comparison.

5.2.c. Hydrothermal modification of sulfide textures

Hydrothermal overprint also affects the sulfide assemblage. Interlocking boundaries between sulfides and secondary amphibole or chlorite indicate textural disequilibrium and metasomatic re–equilibration (Fig. 4.4d). Such features are consistent with recent observations that hydrothermal circulation around mafic intrusions can modify primary sulfide textures and redistribute chalcophile elements (Jian et al., 2024). Although the primary sulfide framework remains recognizable, the degree of overprinting at Camp Lake suggests that post–magmatic processes played a substantial role in modifying sulfide textures, more so than in the Roby and Offset zones, where sulfide textures are generally better preserved.

Taken together, these observations highlight a magmatic evolution broadly comparable to that of the Roby and Offset zones, followed by a more intense hydrothermal overprint that has partially obscured primary textures. This combination of preserved magmatic features and extensive secondary alteration provides essential context for interpreting the behavior of chalcophile elements in the Camp Lake Zone and naturally leads into the examination of PGE distribution in the following section.

5.2.2. Distribution and Behavior of PGE in Camp Lake Zone

The distribution of PGEs in the Camp Lake Zone reflects the combined influence of primary magmatic sulfide fractionation and later hydrothermal modification, consistent with the petrographic framework established earlier. The strong association between PGE and sulfide minerals particularly pentlandite, chalcopyrite, and pyrite (Fig. 5.2) is evident in the mineralogical proportions, where approximately 61% of PGM occurrences are hosted in sulfides (pentlandite 29%, chalcopyrite 23%, pyrite 9%), while 39% occur within or along silicate minerals. This distribution mirrors the dual magmatic–hydrothermal overprint documented in the silicate assemblage.

The predominance of Pd-rich phases in the Camp Lake Zone, with Pd-bearing tellurides, arsenides, and bismuthides collectively representing more than half of the identified PGM (Fig. 4.10a), is consistent with global observations that Pd remains in the sulfide liquid until lower temperatures, promoting the formation of late-stage Pd-rich compounds (Mansur et al., 2020; Karykowski and Maier, 2017). In contrast, Pt, observed here as native metal and accounting for 35% of the PGM assemblage, typically partitions into monosulfide solid solution (MSS) or crystallizes earlier at higher temperatures (Holwell and McDonald, 2010; Kiseeva et al., 2017). This difference in behavior explains the relative scarcity of Pt-rich minerals and the dominance of Pd-rich species in the Camp Lake Zone.

The strong affinity of Pd for pentlandite (Fig. 5.3a), reflected in the high proportion of PGM hosted in this mineral, aligns with recent studies showing that Pd is readily incorporated into pentlandite during MSS exsolution and subsolidus re-equilibration (Mansur et al., 2021; Holwell et al., 2019). The lack of correlation between Pd and chalcopyrite (Fig. 5.3b), also observed in the Camp Lake whole rock, is consistent with the incompatibility of Pd in ISS and chalcopyrite structures (Locmelis et al., 2020). It should be noted, however, that the dataset is based on whole-rock PGE analyses rather than in-situ measurements of sulfide phases, and the percentages of phases were inferred from petrographic observations combined with bulk geochemical data rather than direct mineralogical quantification. These relationships therefore reinforce the interpretation that Pd enrichment in pentlandite is a robust magmatic signature, while the distribution

of PGM in silicates reflects later fluid-assisted redistribution.

The presence of PGM along silicate–sulfide boundaries and within chlorite-rich alteration zones (Fig. 5.2) is particularly significant in light of the strong hydrothermal overprint documented petrographically. Such textures are characteristic of systems where low-temperature fluids mobilize semi-metals (Te, Bi, Sb) and redistribute Pd at the microscale (Holwell et al., 2019; Dare et al., 2014). The Camp Lake Zone, with its pervasive actinolite–tremolite and chlorite alteration, provides ideal conditions for this type of remobilization. The occurrence of rare Pd–Sb and Pd–Al phases further supports the involvement of hydrothermal processes, as similar species have been reported in altered mafic intrusions such as Marathon and Platreef (Maier et al., 2021).

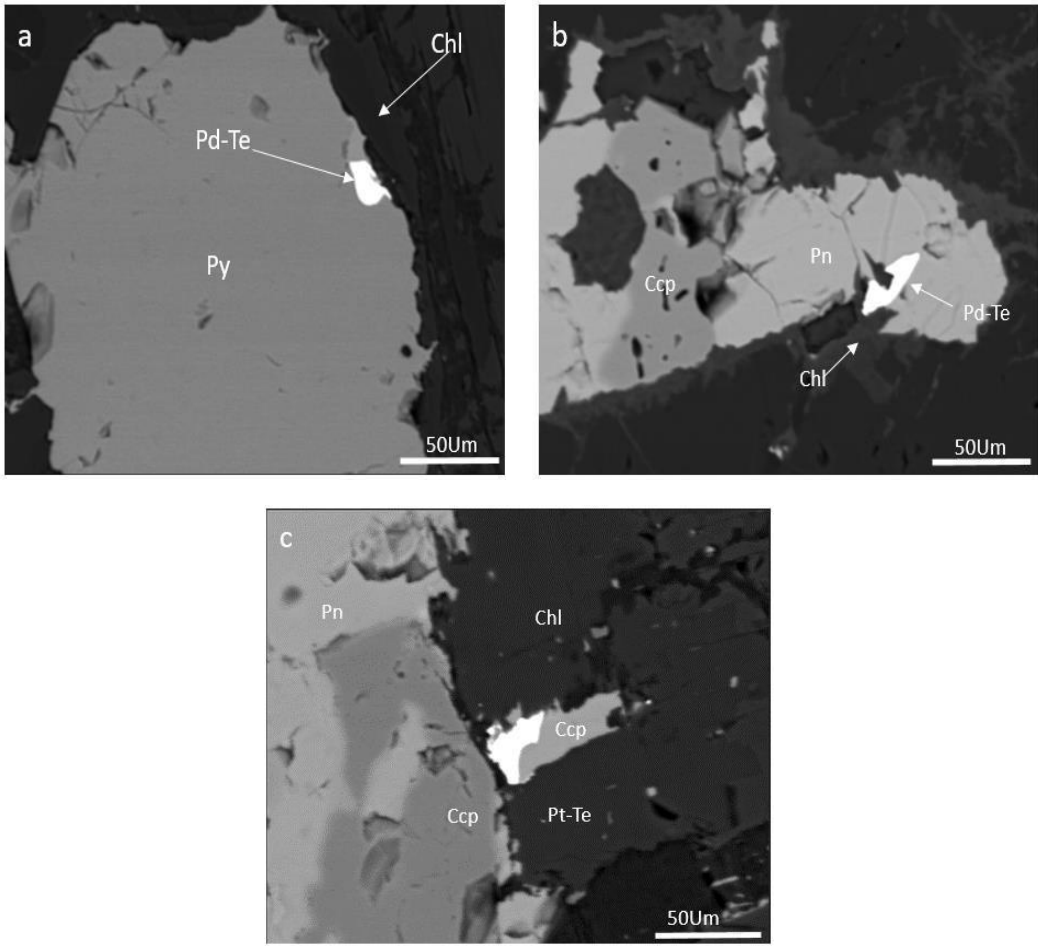

Figure 5.2– a, b, c, Backscattered electron images showing gabbronorite (sample 22-712-055) with preferential concentration of PGMs into copper, iron and nickel bearing sulfide phases with pyrite (Py), pentlandite (Pn) and chalcopyrite (Ccp).

When compared to the Roby and Offset zones, the Camp Lake Zone exhibits a similar magmatic control on PGE distribution but a more pronounced hydrothermal modification. In the Roby Zone, Pd is also largely hosted in pentlandite and late-stage PGM, but the preservation of primary textures is generally better (Smith et al., 2024). The stronger alteration at Camp Lake likely enhanced the redistribution of Pd and semi-metals, increasing the proportion of PGM occurring within silicates (39%) relative to sulfides (Fig. 4.10b). This contrasts with the Offset Zone, where PGM are more tightly constrained to primary sulfide assemblages.

Overall, the PGE mineralogy of the Camp Lake Zone reflects a hybrid system in which primary magmatic sulfide fractionation established the initial Pd–Pt distribution, while subsequent hydrothermal alteration modified and redistributed these elements. The statistical distribution of PGM among sulfides and silicates, combined with the dominance of Pd-rich phases, aligns with contemporary models of PGE behavior during MSS/ISS crystallization, sulfide fractionation, and low-temperature remobilization. These findings place the Camp Lake Zone within the broader class of Pd-rich magmatic sulfide systems and highlight the importance of both magmatic and post-magmatic processes in shaping its PGE signature.

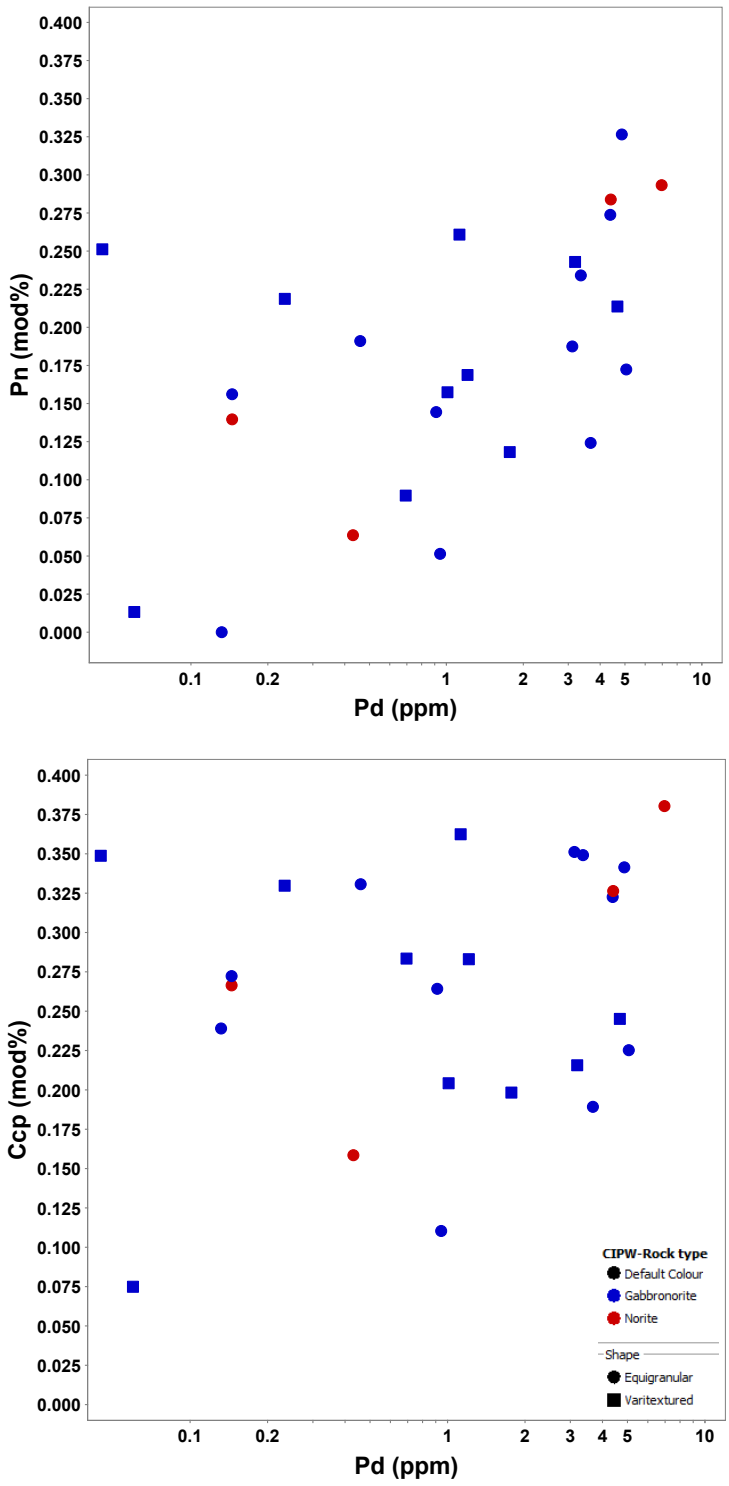

Figure 5.3– Bivariate plots showing a) palladium concentration (Pd, ppm) versus pentlandite abundance (Pn, %) and b) palladium concentration (Pd, ppm) versus chalcopyrite abundance (Ccp, %) for all samples from the Camp Lake Zone.

5.3 Geochemical Signatures and Magmatic Evolution of Camp Lake

Whole-rock geochemistry of the Camp Lake Zone obtained from drill holes 22-711 and 22-712 show downhole variations in major element concentrations (Fig. 5.4a, 5.4b). In hole 22-712, SiO_2 concentration decreases with depth, whereas MgO, Fe_2O_3, and TiO_2 increase. These trends reflect the increasing abundance of Fe- and Mg-rich mineral phases, such as pyroxenes and amphiboles. In contrast, concentrations of Al_2O_3 and CaO remain relatively stable with depth, suggesting a consistent abundance of plagioclase, in agreement with petrographic observations. The parallel behavior of Al_2O_3 and CaO supports a magmatic environment where plagioclase crystallization plays a central role in chemical differentiation (Wilson, 1989; Rollinson, 1993).

This interpretation is further supported by the CaO vs Al_2O_3 diagram (Fig. 5.5), which shows a strong correlation between these two oxides in both the gabbronorites and norites. Most samples follow a compositional trajectory between albite (ab) and anorthite (an), the two main end members of plagioclase feldspar. This indicates that plagioclase plays a central role in controlling the distribution of CaO and Al_2O_3, and that fractional crystallization strongly influenced the evolution of these rocks. The data are clearly distinct from the fields of pyroxenes (orthopyroxene and clinopyroxene), suggesting that these minerals contributed little to the overall CaO and Al_2O_3 content. Finally, the slightly higher Al_2O_3 content observed in some norites indicates the presence of more sodic plagioclase or a higher modal abundance of plagioclase in these rocks compared to gabbronorites, which is consistent with petrographic observations.

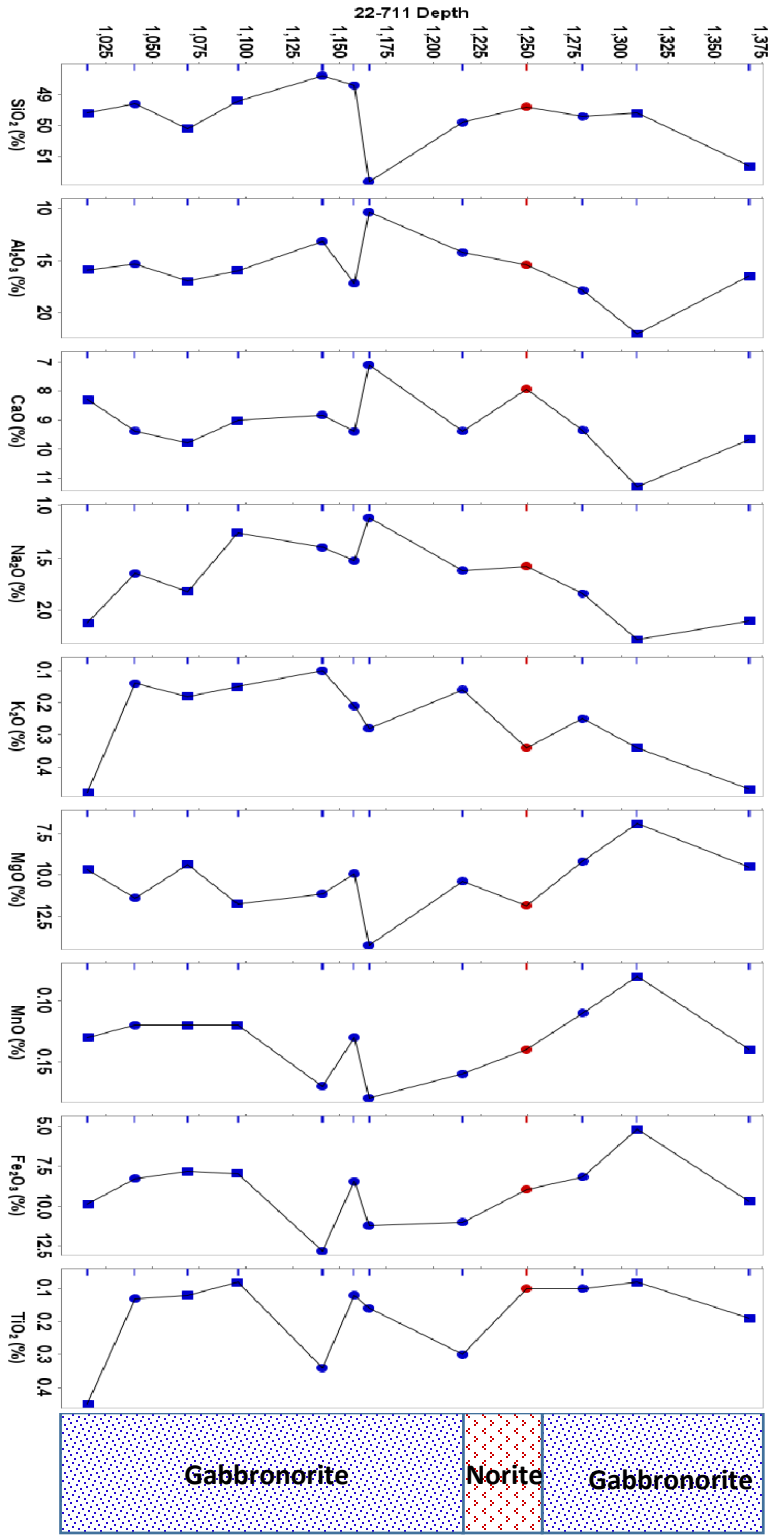

Figure 5.4a– Downhole plots of major element chemistry of the gabbronorites and norite of the Camp Lake Zone, from hole 22-711.

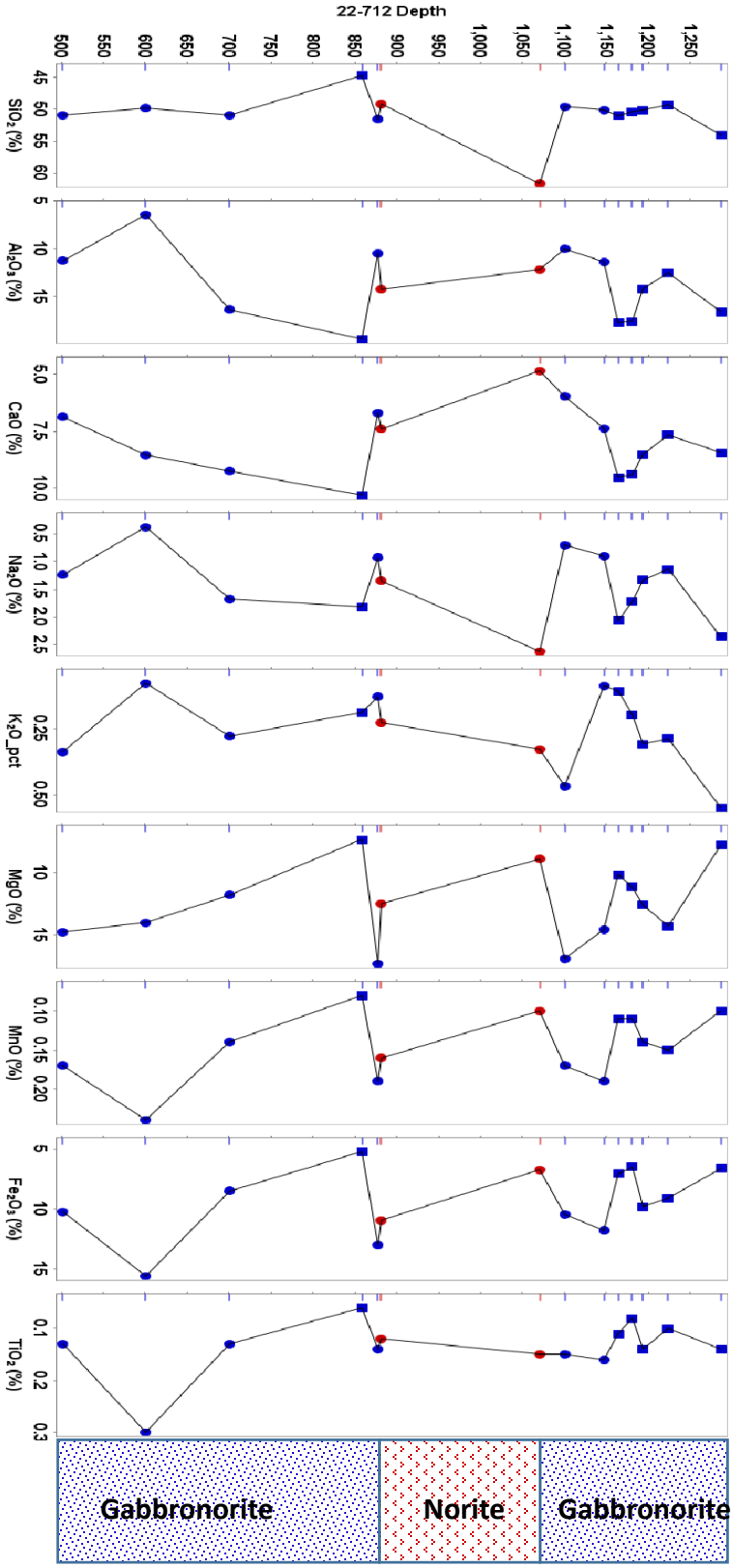

Figure 5.4b– Downhole plots of major element chemistry of the SLDIC gabbronorites and norites of the Camp Lake Zone, hole 22-712.

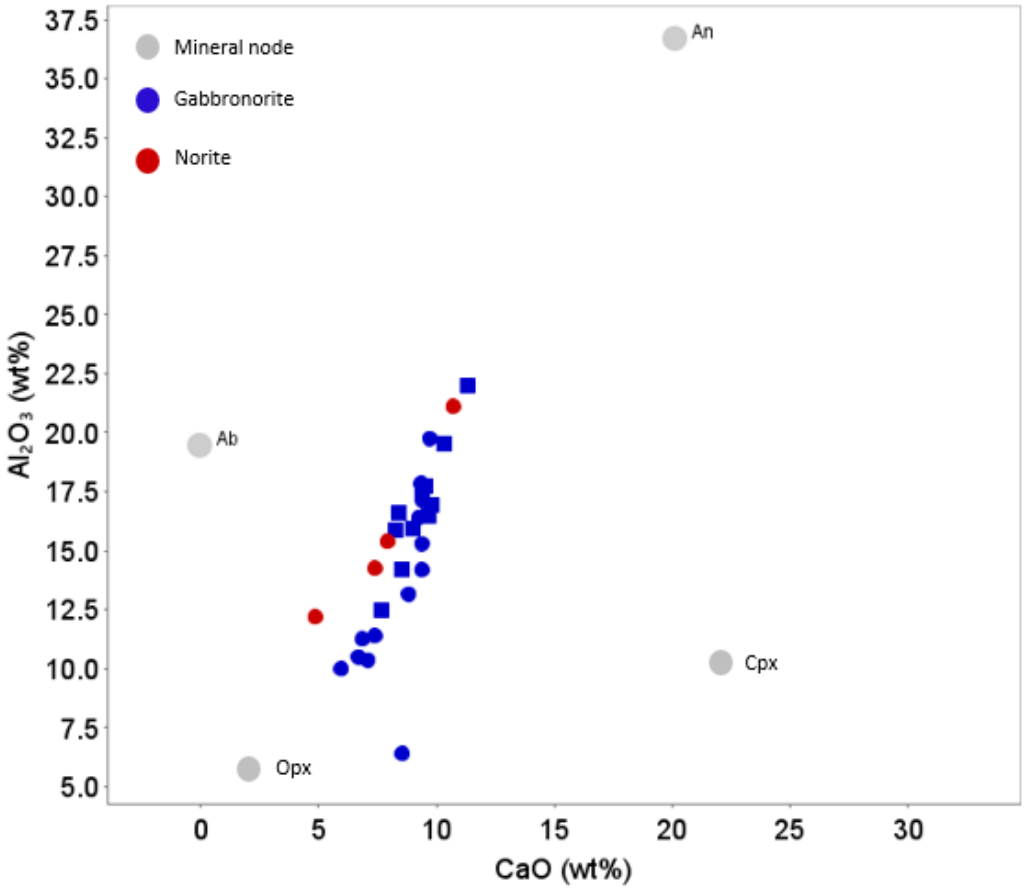

Figure 5.5 – Geochemical plot of Camp Lake rocks showing Al_2O_3 vs CaO (wt%), as well as representative mineral compositions of orthopyroxene (Opx), clinopyroxene (Cpx), albite (Ab), and anorthite (An). The plot shows a cluster of samples close to the albite and orthopyroxene. Mineral compositions from IMDEX ioGAS-64, version 8.1.1.

Additional constraints on the magmatic affinity of the Camp Lake rocks are provided by the Jensen cation plot (Fig. 5.6), where samples plot in the field of andesite high Mg basalt and komatiite. This increase in MgO corroborate with the downhole increase in MgO and Fe_2O_3 and indicates that the Camp Lake magma followed a calc-alkaline differentiation pathway dominated by pyroxene ± plagioclase fractionation. Importantly, the samples do not shift toward the high-Ti–Fe apex, suggesting that Fe-Ti oxide fractionation was limited and that TiO_2 depletion reflects only minor early titanomagnetite or ilmenite crystallization.

The low TiO_2 content observed in the Camp Lake samples may also reflect early precipitation of Ti-bearing phases such as titanomagnetite or ilmenite, which efficiently remove Ti from the melt. However, the primitive mantle–normalized spider diagrams (Fig.

5.7) show that Camp Lake samples are not depleted in incompatible elements relative to the Roby and Offset zones. Instead, Camp Lake displays slightly higher abundances of several incompatible elements (e.g., Th, Nb, La, Ce, Nd, Zr, Hf, Y) and a less pronounced Nb anomaly. The Camp Lake patterns are also flatter and less fractionated, whereas the SLDIC samples from Roby and Offset show stronger inter-element variability and more pronounced anomalies (Fig. 5.7). These features suggest that the Camp Lake magma may have been derived from a more incompatible-element–enriched mantle source, or that it experienced less extraction of enriched melt during earlier differentiation stages. The smoother shape of the Camp Lake patterns further supports a more homogeneous magmatic evolution compared with the other SLDIC zones. These observations are

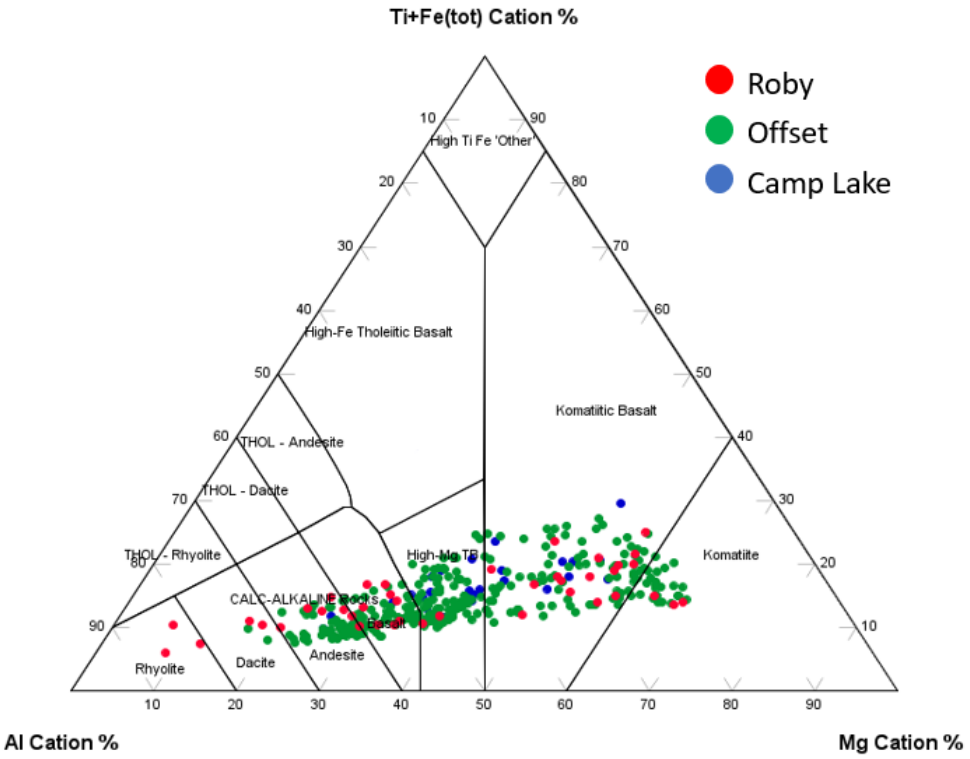

Figure 5.6 – Jensen Cation Plot Illustrating Magmatic Affinities of the Roby, Offset, and Camp Lake Zones.

consistent with open-system behaviour involving intercumulus liquid loss or moderate crustal assimilation (Pearce, 1982; Irvine, 1975).

The averaged primitive mantle–normalized spider diagrams for the Roby, Offset, and Camp Lake zones (Fig. 5.7), reveal broadly comparable geochemical patterns, characterized by a systematic negative Nb anomaly and by pronounced LREE enrichment

relative to HREE (Fig. 5.7). All three zones exhibit subparallel REE profiles with relatively flat HREE, indicating a coherent behaviour of incompatible elements across the SLDIC. The LREE enrichment is further supported by the primitive mantle–normalized La/Sm_n ratios, which are similarly elevated across the complex (3.27 for Roby, 3.73 for Offset, and 4.23 for Camp Lake). Despite this overall similarity, the amplitude of enrichment differs, with Camp Lake representing the most enriched end-member, Roby the most depleted, and Offset occupying an intermediate position.

The negative Nb anomaly common to all three zones constitutes a major geochemical signature of the SLDIC. This deficit is characteristic of a mantle source that has been previously metasomatized in a subduction-related environment, where HFSE are selectively depleted. The anomaly may be further enhanced by early magmatic fractionation involving oxidized phases that can influence the Nb budget, as well as by felsic crustal assimilation, both of which can reinforce Nb depletion (Pearce, 2008; Jenner, 2017; Barnes et al., 2020). The presence of this anomaly in all three zones suggests derivation from a common parental magma or from a mantle source already modified prior to emplacement of the complex.

The combined REE–HFSE signatures — LREE enrichment, weakly fractionated HREE, negative Nb anomaly, and slight Eu anomalies — indicate a mantle source enriched in incompatible elements, consistent with a lithospheric mantle that experienced prior metasomatism. Differences in enrichment amplitude between the zones are best explained by local variations in differentiation, retention of incompatible elements in residual liquids, or variable proportions of cumulate and intercumulate material, rather than by major differences in mantle source composition.

Overall, the similarity of the geochemical signatures among Roby, Offset, and Camp Lake confirms that they belong to a single regional magmatic system, whose evolution was locally modulated by internal intrusive processes. This geochemical organization aligns with recent models for PGE-bearing mafic intrusions, in which a subduction-modified, incompatible-element–enriched mantle source feeds a common parental magma, whose signatures are subsequently modulated by small-scale magmatic evolution processes (Barnes & Ripley, 2016; Barnes et al., 2020; Holwell et al., 2021; Maier et al., 2021).

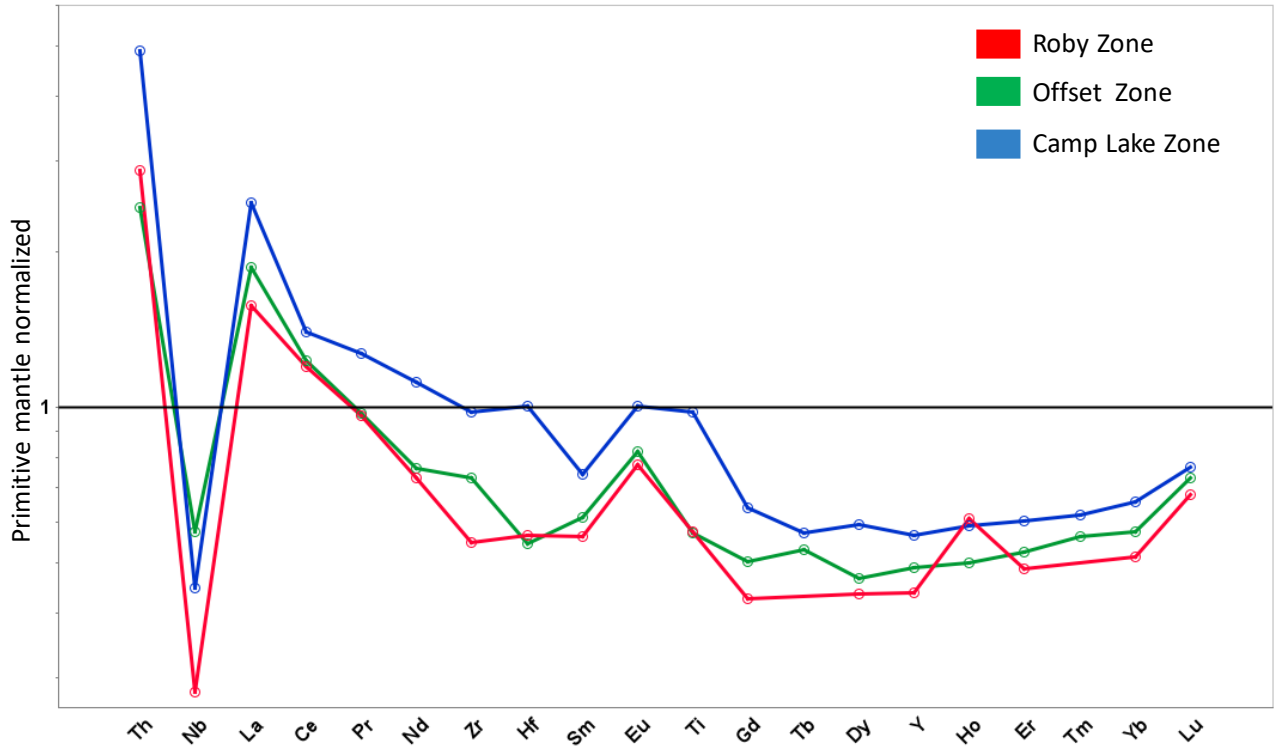

Figure 5.7 – Spider diagram of geochemical variations in gabbronorites and norites from the SLDIC: Primitive mantle-normalized averages (Sun and McDonough, 1989) for the Roby, Offset and Camp Lake Zones.

5.3.1 Mantle Source Characteristics and Crustal Interaction

A detailed analysis of whole-rock geochemistry allows for the characterization of the mantle source of the Camp Lake magma, the identification of potential crustal or metasomatic influences, and the reconstruction of its differentiation processes. This interpretation is based on an integrated approach using incompatible trace-element ratios which constrain the nature of the mantle reservoir and help evaluate the extent of crustal contamination or subduction-related metasomatism.

The mean of Th/Yb (1.14) and Nb/Yb (0.97) ratios show that most Camp Lake samples plot well above the MORB–OIB array of the normalize Pearce (2014) diagram (Fig. 5.8). Using this diagram Camp Lake Zone samples fall within or near the continental-arc domain. The systematic offset of the Camp Lake samples relative to the MORB–OIB trend indicates either interaction with Th-enriched crustal materials or derivation from a mantle

source previously modified by subduction-related fluids or melts. Such an interpretation is consistent with a metasomatized lithospheric mantle, a feature commonly documented in Archean terranes influenced by ancient subduction processes (Hawkesworth et al., 1995; Pearce, 2014).

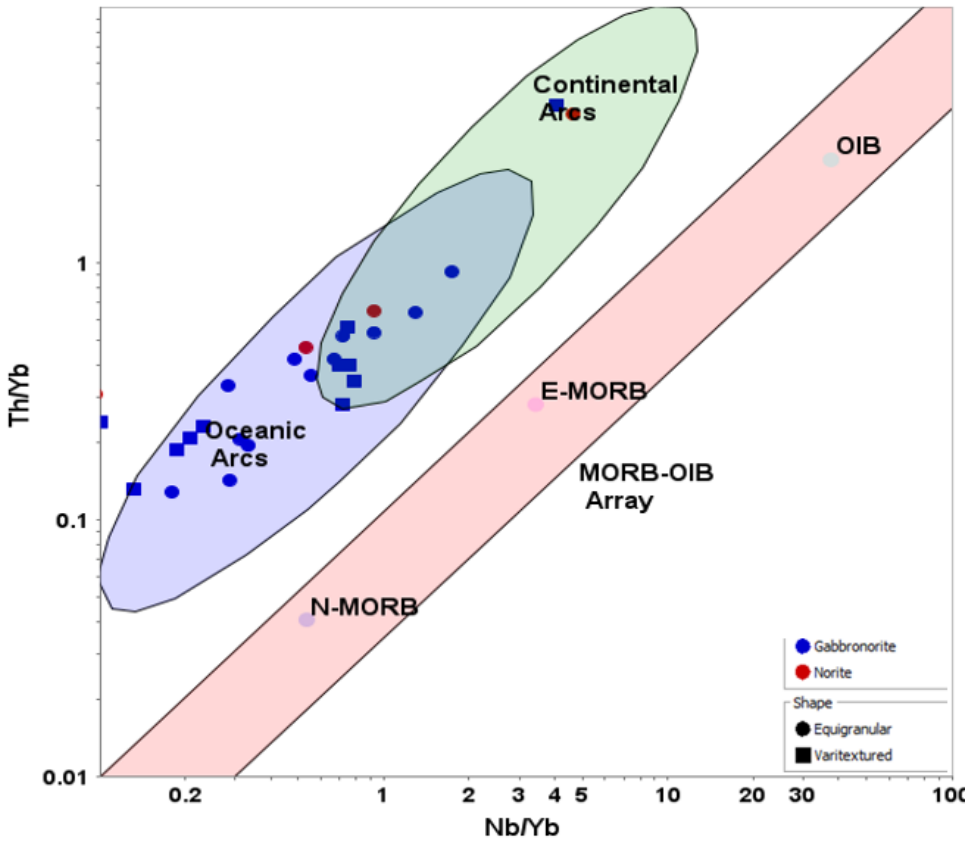

Figure 5.8– Discrimination diagram of Th/Yb vs Nb/Yb for Camp Lake samples, compared to the fields of MORB (N-MORB, E-MORB), OIB, and average Archean continental crust. The trends indicate an enriched mantle source with moderate crustal input. Normalized from Pearce 2014.

Beyond their position on the Pearce (2014) diagram, the Camp Lake samples display an incompatible-element systematics that further supports derivation from an enriched lithospheric mantle source. The Th/Yb ratios, ranging from 0.13 to 15.55 with an average of 1.17, combined with comparatively lower Nb/Yb values (0.10 to 4.65, average of 0.92), indicate a mantle reservoir that had already incorporated incompatible-element-rich components prior to melting. Such enrichment is commonly attributed to ancient subduction-related metasomatism, during which Th-bearing fluids or melts percolate through the lithospheric mantle, leaving a long-lasting imprint on its trace-element budget. This type of metasomatic overprint is widely documented in Archean cratonic

settings and is considered a key mechanism for generating the enriched signatures observed in many mafic and ultramafic intrusions (Hawkesworth et al., 2017; Mole et al., 2020; Brown et al., 2022; Wang et al., 2020; Yang et al., 2022).

The broad range of Th/Yb and Nb/Yb ratios within the Camp Lake dataset also suggests a degree of chemical heterogeneity in the mantle source, consistent with recent models describing the Archean lithospheric mantle as a mosaic of enriched and depleted domains inherited from successive cycles of subduction, accretion, and refertilization (Johnson et al., 2019; Fiorentini et al., 2021). Thus, the Camp Lake data point to a mantle that is not only variably enriched but also intrinsically heterogeneous at the scale of the SLDIC, in agreement with modern views of Archean lithospheric mantle evolution.

The (Cu/Zr) vs (La/Sm) primitive mantle diagram (Fig. 5.9) illustrates that most samples cluster within a domain characterized by moderate LREE enrichment and sulfide accumulation, indicative of a magmatic system that retained its chalcophile element budget, with moderate crustal assimilation (Ripley and Li, 2013). A few outliers, depleted in Cu and enriched in La, reflect episodes of contamination that triggered early sulfide saturation and subsequent segregation.

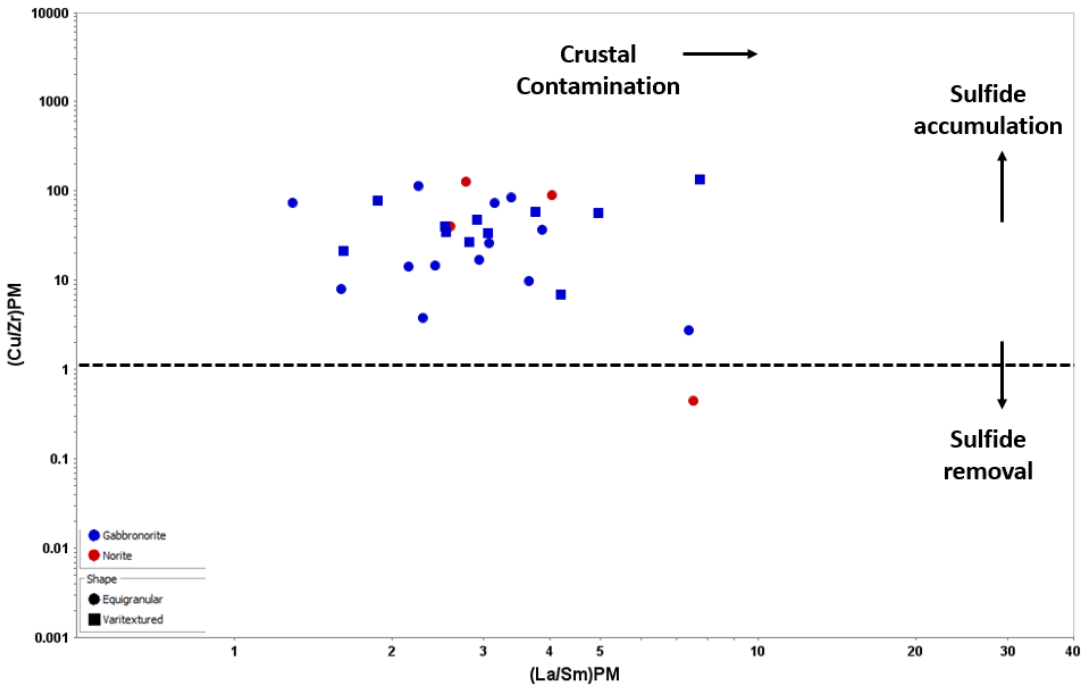

Figure 5.9 – Primitive mantle normalized Cu/Zr ratio versus La/Sm for the samples from Camp Lake Zone. Normalized to primitive mantle (values from Sun and McDonough (1995).

Overall, the geochemical data suggest that the Camp Lake magma originated from an enriched mantle reservoir, which could have been modified by subduction-related fluids, with isolated episodes of crustal contamination identifiable in a small number of samples.

To corroborate and strengthen the observations, Sm-Nd isotopic analysis can be used to evaluate crustal contributions in magmatic systems, particularly when integrated with trace element geochemistry. At Camp Lake, the initial $^{143}Nd/^{144}Nd$ ratios recalculated to the crystallization age (2690 Ma) are remarkably consistent, ranging from 0.50917 to 0.50920. This narrow spread reflects an isotopically coherent source, with no major disturbance from isotopically distinct crustal materials. εNd values for juvenile magmas at 2.7 Ga range between +2 to +4; this positive value represents a depleted mantle source (Jahn et al., 2001). The εNd(t) values, which range from +0.30 to +1.12 (Tab. 4.2), are compatible with a slightly depleted mantle source, characteristic of a reservoir that had previously undergone extraction of melts enriched in incompatible elements (Jahn et al., 2001).

Trace-element data provide complementary insight. The Th/Yb ratios (0.13 to 15.55; average 1.17) and Nb/Yb ratios (0.10 to 4.65; average 0.92) display a structured variability that reflects the inheritance of an enriched lithospheric mantle prior to melting. This distribution is consistent with the ancient addition of incompatible-element-rich components to the mantle, a process widely attributed to deep metasomatic episodes (Hawkesworth et al., 2017; Wang et al., 2020; Yang et al., 2022; Brown et al., 2022). Recent studies further emphasize that such enrichment may result from repeated cycles of mantle refertilization involving the infiltration of fluids or melts derived from ancient subduction zones (Johnson et al., 2019; Fiorentini et al., 2021; Liu et al., 2023; Zhang et al., 2024, Pei et al., 2025).

Two isolated gabbronorites and one norite exhibit higher Th/Yb values (Fig. 5.10), which may reflect localized variations in the degree of mantle enrichment or minor interactions between the magma and the surrounding rocks. Their limited number, however, suggests that they do not represent the dominant behavior of the system.

Overall, the convergence between Nd isotopes and Th/Yb vs Nb/Yb ratios indicates that the Camp Lake magma was derived from an enriched mantle source modified by fluids associated with ancient subduction processes. Following emplacement, the magma evolved primarily through internal differentiation and fractional crystallization, with only

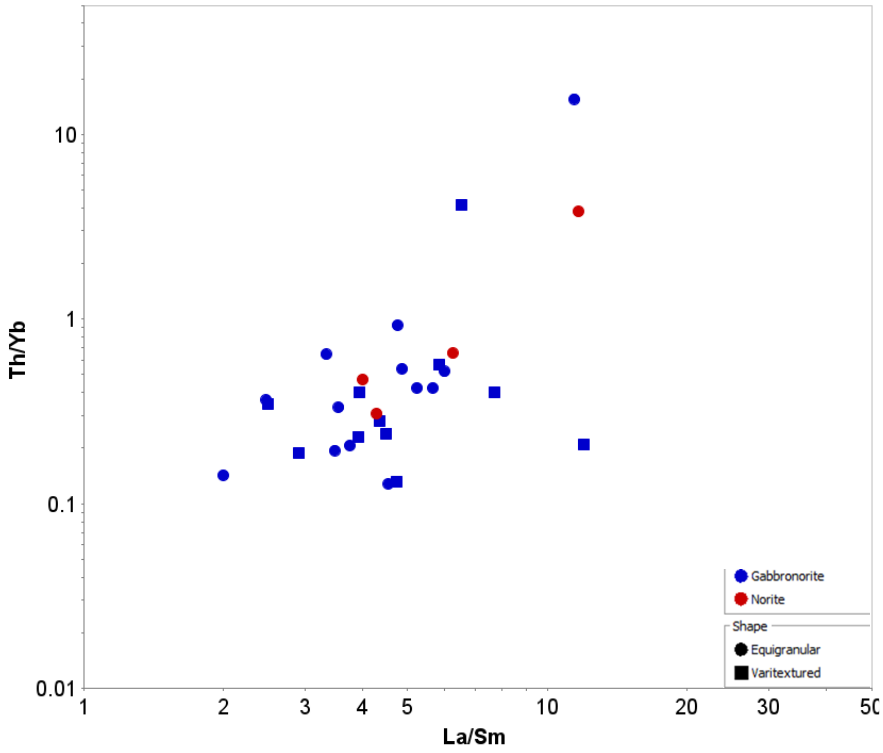

Figure 5.10– Variations in La/Sm and Th/Yb ratios in norites and gabbronorites of Camp Lake Zone.

limited crustal influence.

This isotopic and geochemical coherence confirms the essentially mantle-dominated character of the Camp Lake magmatic system. At Camp Lake, the absence of such isotopic anomalies suggests that crustal contamination, if present, has remained localized and limited, as previously discussed in the section referencing three isolates samples of Figure 5.10. This conclusion is further supported by La/Sm ratios (median of 4.52) and Th/Yb ratios (median of 0.38), which reflect a moderately enriched mantle source (Pei et al., 2025). A few outlier samples with Th/Yb > 4 and La/Sm > 10 (Fig. 5.10) may represent localized interactions with crustal materials or a particularly enriched mantle source. However, their rarity suggests they do not reflect the overall behavior of the system.

The comparison of the three zones reveals a coherent yet structured geochemical

gradient, reflecting variable degrees of mantle enrichment, metasomatic overprinting, and crustal interaction. When the mean incompatible trace-element ratios for each zone are plotted on the Th/Yb – Nb/Yb discrimination diagram of Pearce (2014), the three

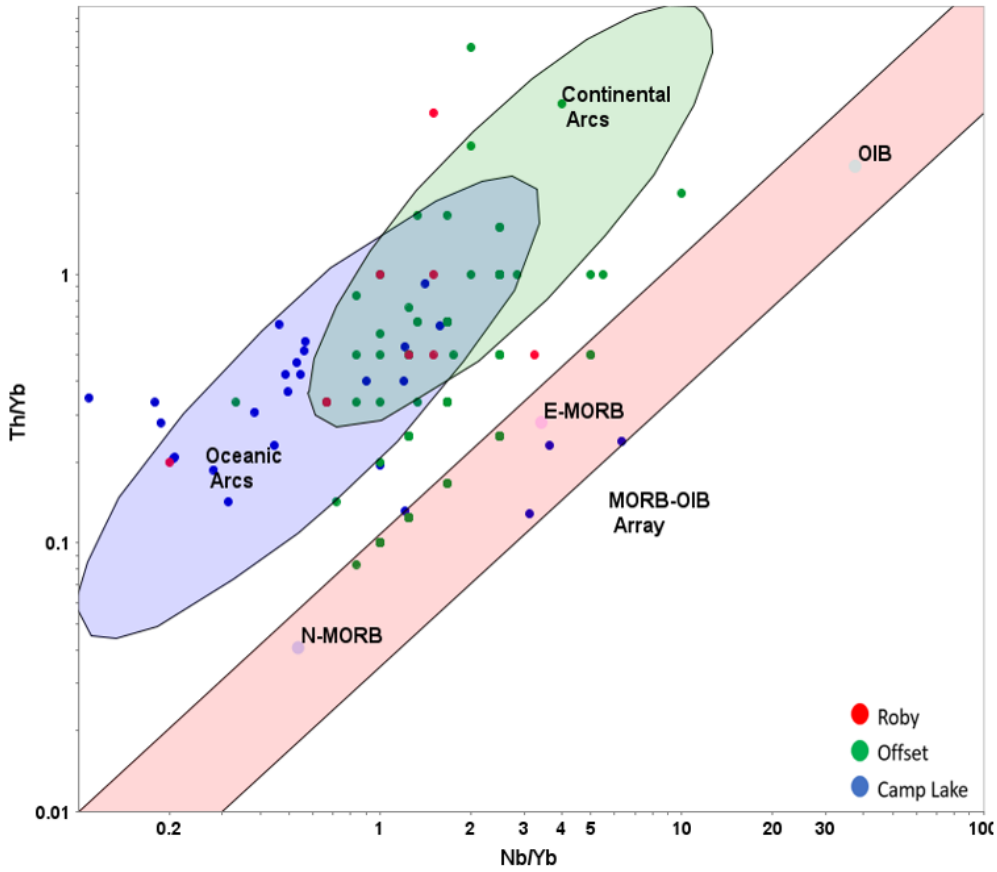

Figure 5.11– Discrimination diagram of Th/Yb vs Nb/Yb for Roby, Offset and Camp Lake samples, compared to the fields of MORB (N-MORB, E-MORB), OIB, and average Archean continental crust. Normalized from Pearce 2014.

datasets define partially overlapping but clearly distinguishable fields (Fig. 5.11). Despite their differences, all three zones plot above the MORB – OIB array, collectively indicating derivation from a lithospheric mantle source modified by ancient subduction processes.

Among the three, Camp Lake exhibits the strongest enrichment, with the highest mean Th/Yb ratio (1.14) and the lowest mean Nb/Yb ratio (0.97). This combination places Camp Lake closest to the continental-arc domain of the Pearce diagram (Fig. 5.11), consistent with derivation from a mantle reservoir enriched by subduction-derived fluids or melts. Roby, with intermediate mean values (Th/Yb = 0.93; Nb/Yb = 1.28), reflects a mantle source that is enriched but to a lesser degree, preserving a mixed signature between enriched and moderately depleted domains. Offset, by contrast, plots closest to

the MORB–OIB trend, with the lowest Th/Yb (0.65) and the highest Nb/Yb (1.86), indicating that it sampled the least enriched portion of the lithospheric mantle.

This geochemical gradient is further supported by isotopic evidence. At Camp Lake, the narrow range of initial $^{143}Nd/^{144}Nd$ ratios (0.50917–0.50920) and the slightly positive εNd(t) values (+0.30 to +1.12) indicate a coherent, mantle-dominated source with minimal crustal assimilation. In contrast, Offset displays negative εNd(t) values ranging from –3.47 to 0.384 (Jonsson, 2023), indicating significant crustal involvement during magma evolution (Fig. 5.12). Although Roby lacks a complete isotopic dataset in the consulted databases, its trace-element signature suggests a mantle source less enriched than Camp

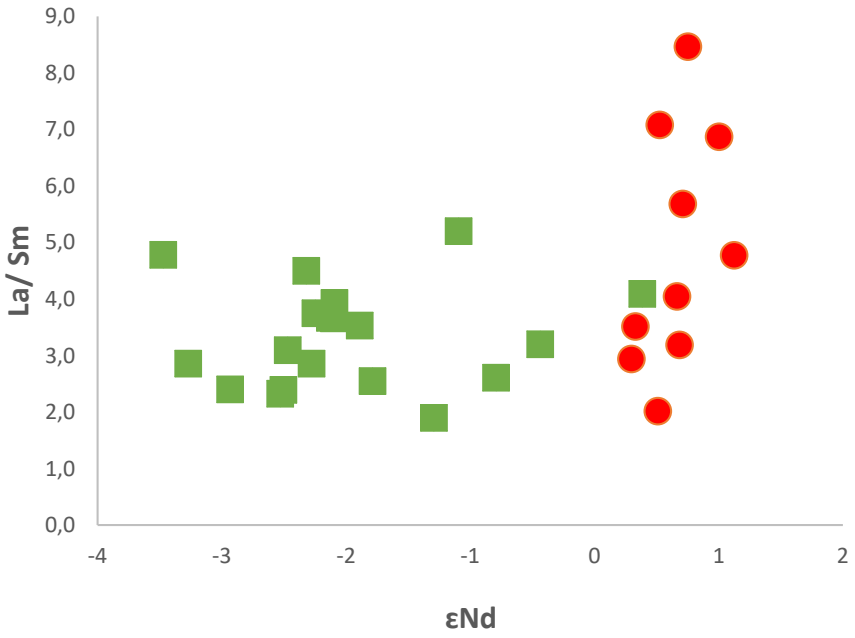

Figure 5.12– Contrasting εNd signatures highlighting mantle source variations between previous studies and the current dataset. Red circles represent samples from the Camp Lake Zone, while green squares correspond to data from the Offset Zone (Jonsson, 2023).

Lake, along with crustal contamination at variable scales.

Additional insight is provided by normalized (Cu/Zr)PM ratios, which track sulfide saturation and potential crustal interaction (Fig. 5.13). Offset shows the highest mean (Cu/Zr)PM (63.14), consistent with efficient sulfide retention and minimal crustal influence. Roby, with the lowest mean value (28.93), reflects partial sulfide removal and a more open-system behavior, in agreement with its isotopic evidence for crustal

assimilation. Camp Lake again occupies an intermediate position (48.10), indicating limited modification of its chalcophile element budget and localized crustal interaction.

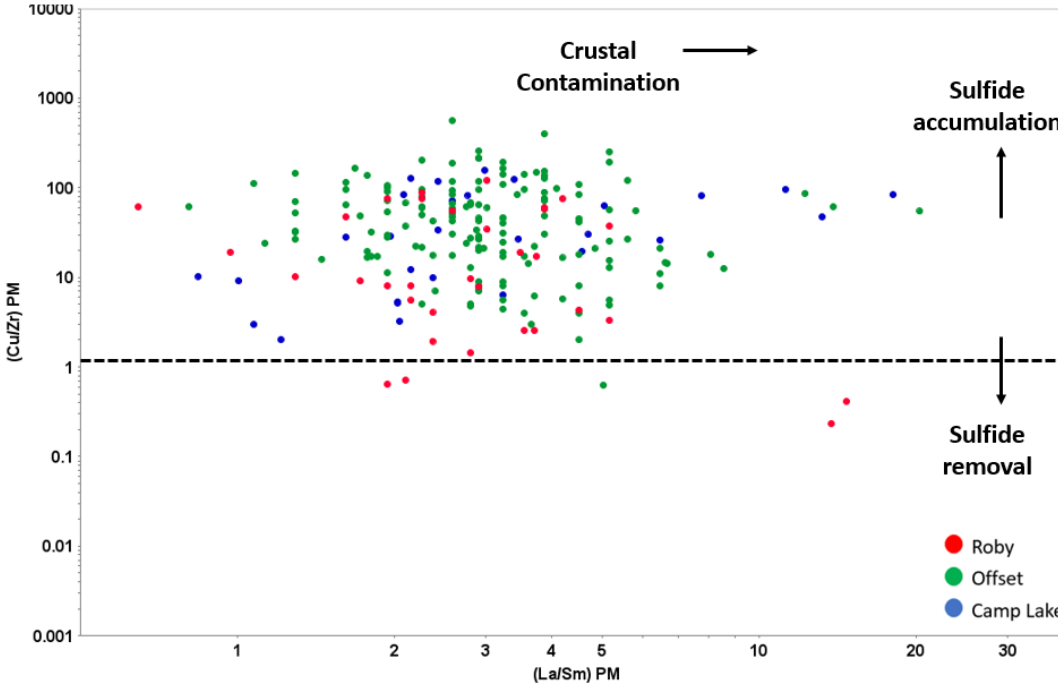

Figure 5.13– Primitive mantle normalized Cu/Zr ratio versus La/Sm for the samples from Roby, Offset and Camp Lake Zones. Normalized to primitive mantle (values from Sun and McDonough (1995).

5.3.2 Controls on Sulfur Origin and Ni-Cu-PGE Mineralization

The downhole plot (Fig. 5.14) shows the abundance and ratio of Pt and Pd with increasing depth in the drill holes studied. At Camp Lake, the mineralizing processes consistently favored Pd enrichment over Pt, regardless of rock type. This trend is best explained by primary magmatic processes: high R-factor conditions promote strong partitioning of Pd into sulfide melts relative to Pt, leading to Pd-rich sulfide assemblages even at low sulfur concentrations. Moreover, monosulfide solid solution (MSS) preferentially incorporates Pd over Pt during crystallization, such that fractional removal of MSS further enhances Pd enrichment in the residual system (Mungall et al., 2005; Barnes et al., 2020). However, the Pd/Pt ratios observed at Camp Lake (7.46) are relatively low when compared to other zones of the SLDIC such as Roby (~12) and Offset (~13.60) (Djon et al., 2012). These high ratios exceed what can be expected in a typical magmatic NI-Cu-PGE deposits and suggests possible pre-enrichment of the silicate magma in Pd, likely through the extraction of Pd from early-formed sulfides in the deeper parts of the magmatic

plumbing system (Maier et al., 1998). The observation of these high ratios in all main zones of SLDIC suggests that this pre-enrichment could have been widespread throughout SLDIC.

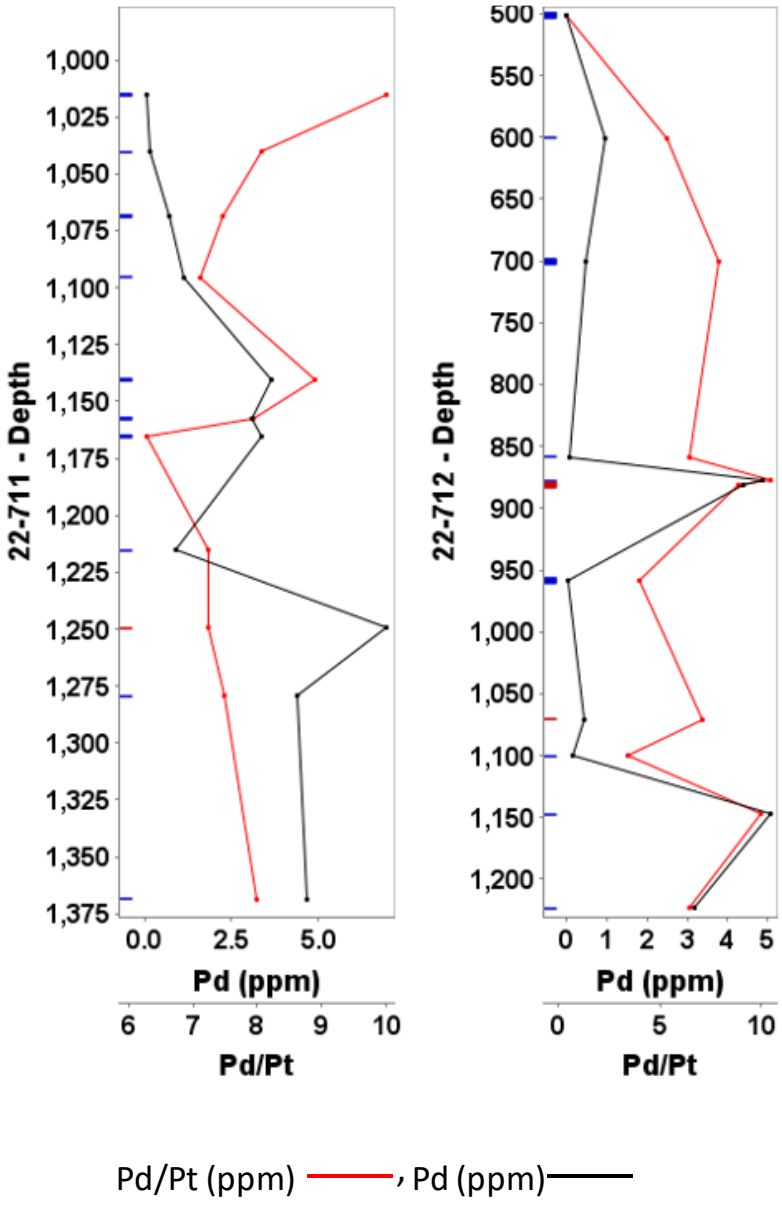

Figure 5.14 – Downhole plots of Pd/Pt ratio and Pd variation of Camp Lake drill holes 22-711 and 22-712.

Sulfur isotopic data ($\delta^{34}S$, Fig. 5.15), combined with S/Se and Cu/Pd ratios (Fig. 5.16a) and Pd concentrations (Fig. 5.16b) from drill holes 22-711 and 22-712, provide further insight into the genesis of the mineralization. $\delta^{34}S$ values ranging from -1‰ to

+0.3‰ fall within the typical range for the upper mantle, excluding any significant crustal sulfur contribution (Farquhar and Wing, 2003; Seal, 2006). This isotopic homogeneity, together with the limited $\Delta^{33}S$ (range from -0.02 to -0.11) variation reported in the literature for the South Lac Des Iles complex area (Jonsson, 2023), supports a mantle-derived sulfur source. Downhole plots reveal that Pd peaks (ranging from 5.06 to 6.96 ppm) coincide with the lowest Cu/Pd and S/Se ratios, particularly in drill hole 22-711 between 1225 and 1275 m depth (Fig. 5.17).

This association indicates that Pd concentration is closely linked to Cu and S abundance, reflecting the strong control exerted by sulfide saturation and metal partitioning during magmatic differentiation. Such relationships are consistent with systems where sulfides efficiently scavenge Pd, a process that can be enhanced under

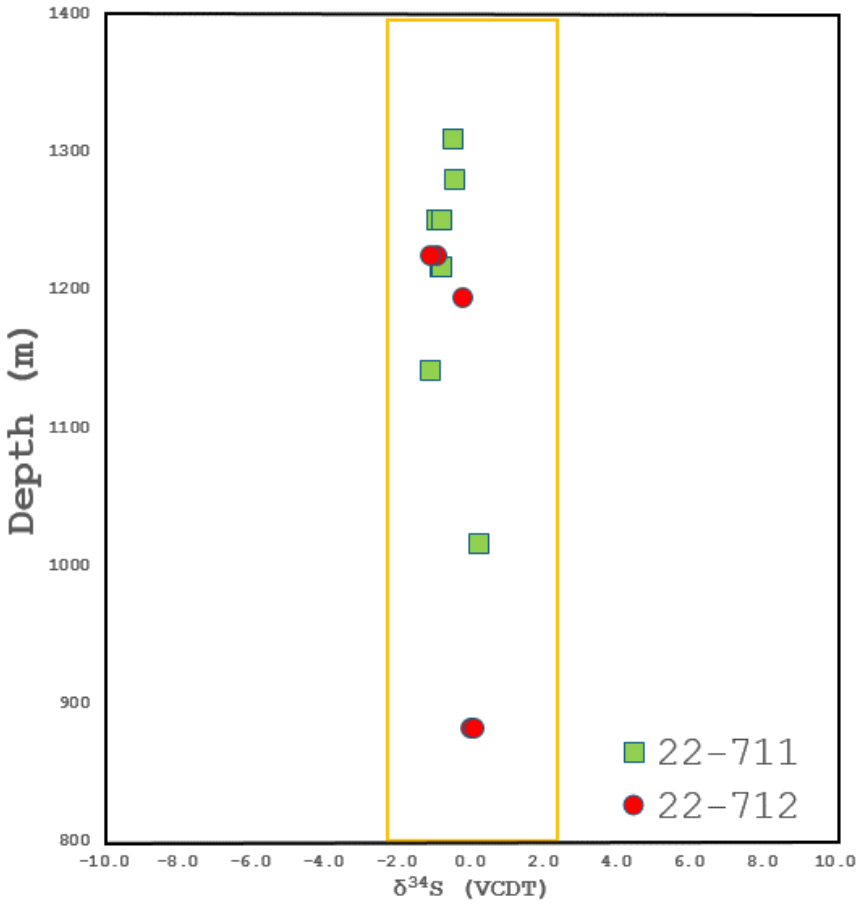

Figure 5.15– Bivariate diagram of $\delta^{34}S$ vs depth of all analyzed samples. Yellow box is the mantle range (Sun and McDonough, 1989).

high R-factor conditions, although the correlation itself primarily reflects sulfide affinity rather than R-factor alone (Maier et al., 1998).

S/Se ratios range between 915 - 4207, most are below the mantle reference range (2850 - 4350), represented in Figure 5.16b by the light grey area. While such low S/Se ratios may partly reflect sulfur degassing (Eckstrand & Hulbert, 1987), they can also result from the addition of sulfur under high R-factor conditions, where sulfides equilibrate with large volumes of silicate melt and S increases more rapidly than Se (Queffurus & Barnes, 2015; Smith et al., 2017). The absence of correlation between loss on ignition (LOI) and S, Cu, S/Se, or Cu/Pd contents suggests that secondary processes have minimal influence on the observed geochemical variations, rather the correlation reflects the influence of magmatic sulfide segregation (Fig. 5.18), this observation is different from what was reported for the other zones such as the strong correlation of chlorite-actinolite alteration with PGE distribution in Roby zone (Gomwe, 2008). In contrast, at the Camp Lake Zone evidence of a primary magmatic origin is supported by the strong correlation between Cu and Ni (Fig. 5.19).

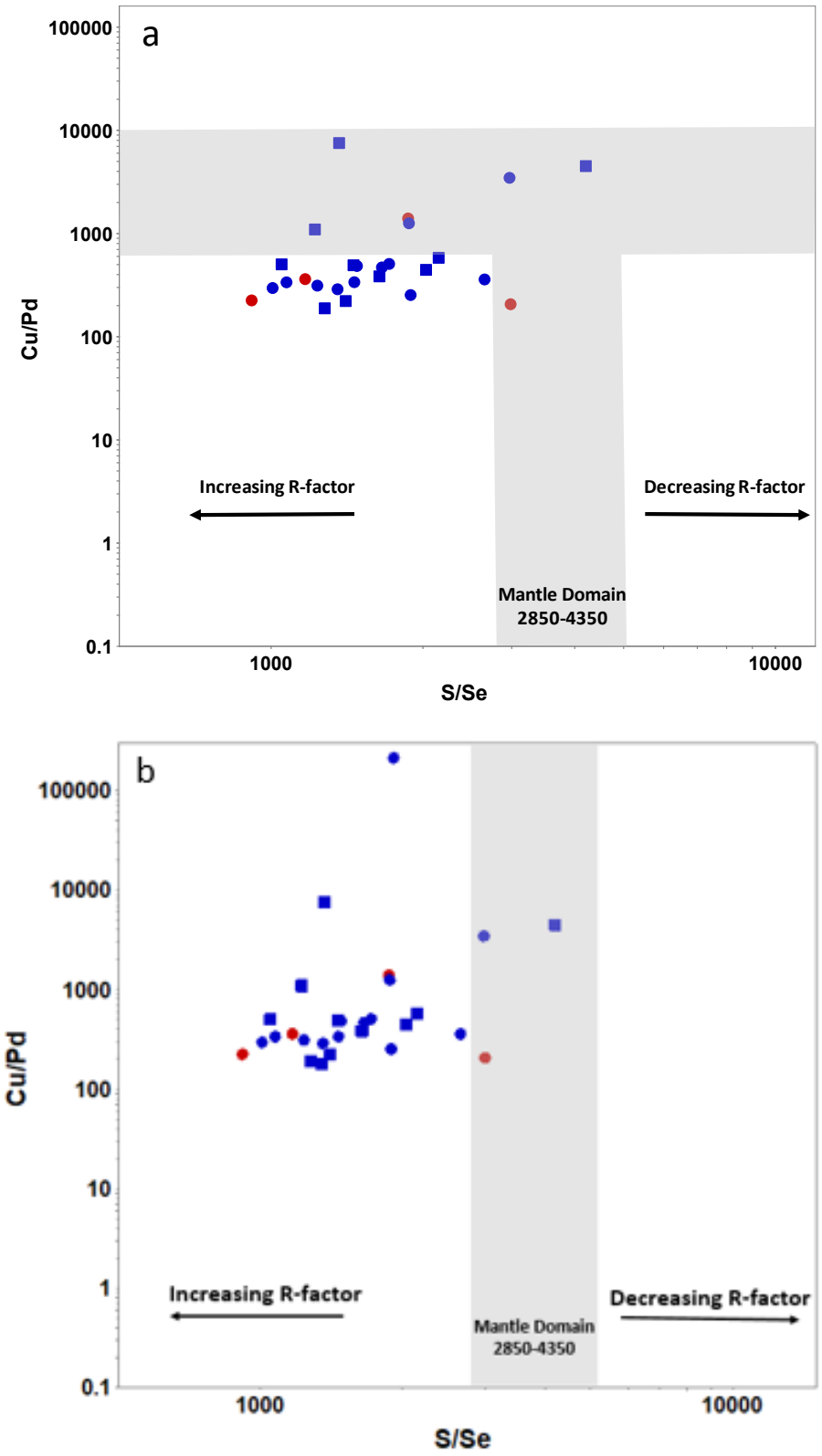

Figure 5.16– a) Distribution of Cu/Pd ratios in samples from the Camp Lake Zone; b) S/Se vs. Pd (ppb) Diagram of Camp Lake samples. Light grey box is mantle range Cu/Pd (from Barnes et al., 1993) and S/Se (from Eckstrand and Hulbert, 1987).

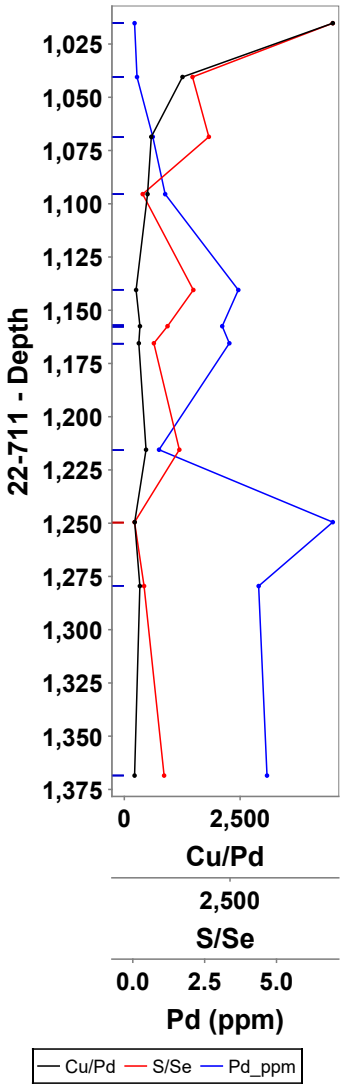

Figure 5.17 – Vertical variation of the Cu/Pd ratio in drill hole 22-711, highlighting its inverse relationship with Pd concentration between 1225 and 1275 m depth.

The absence of a relationship between LOI and Pd at the Camp Lake zones suggests a minimal effect of hydrothermal processes in Pd enrichment, this is consistent with petrographic observations where PGE abundance or PGE minerals are rarely associated with secondary hydrothermal phases such as chlorite, actinolite-tremolite. Previous studies in the SLDIC have attributed the Pd enrichment in the Roby and Offset zone to remobilization influenced by successive magma injections which may have favored the concentration of Pd in geological traps (Barnes et al. 1993; Hinchey et al., 2005). At Camp Lake this hypothesis may also be the driving factor for Pd enrichment due to the similarities in term of rock type, sulfide assemblages, Pd/Pt, and Cu/Pd ratio.

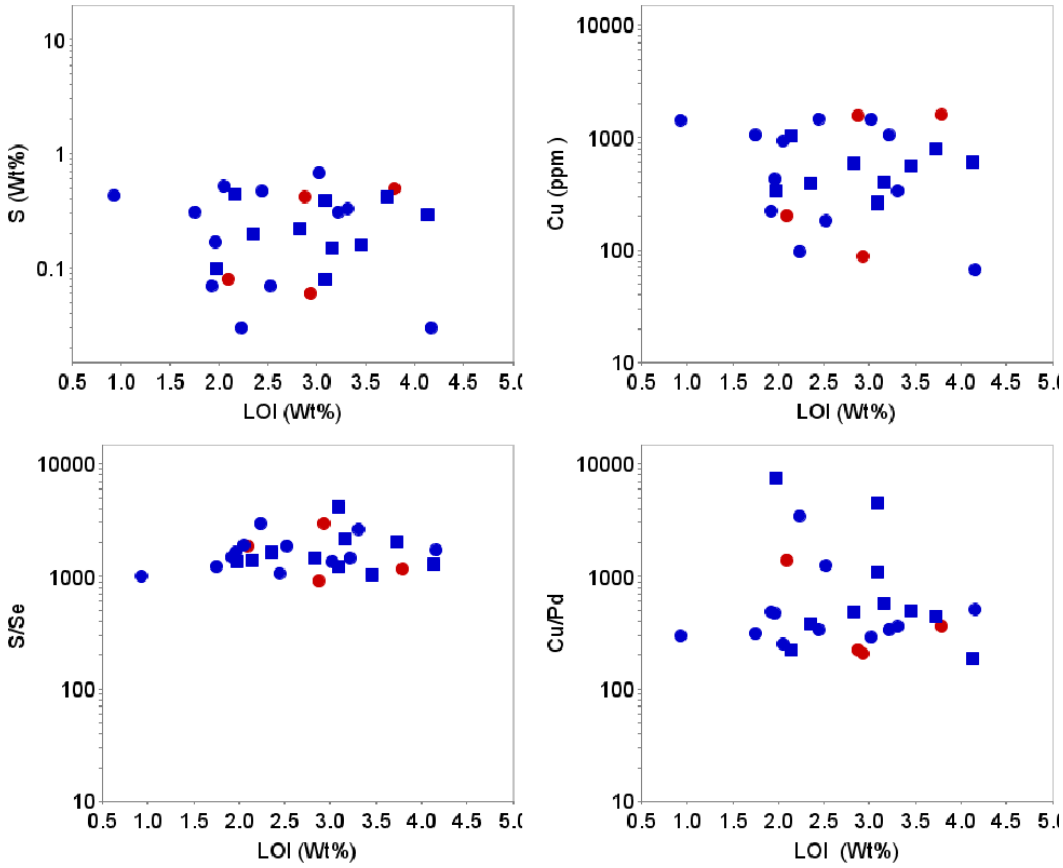

Figure 5.18– Bivariate plots of loss on ignition (LOI) vs. S (%), Cu (ppm), S/Se, and Cu/Pd in all samples.

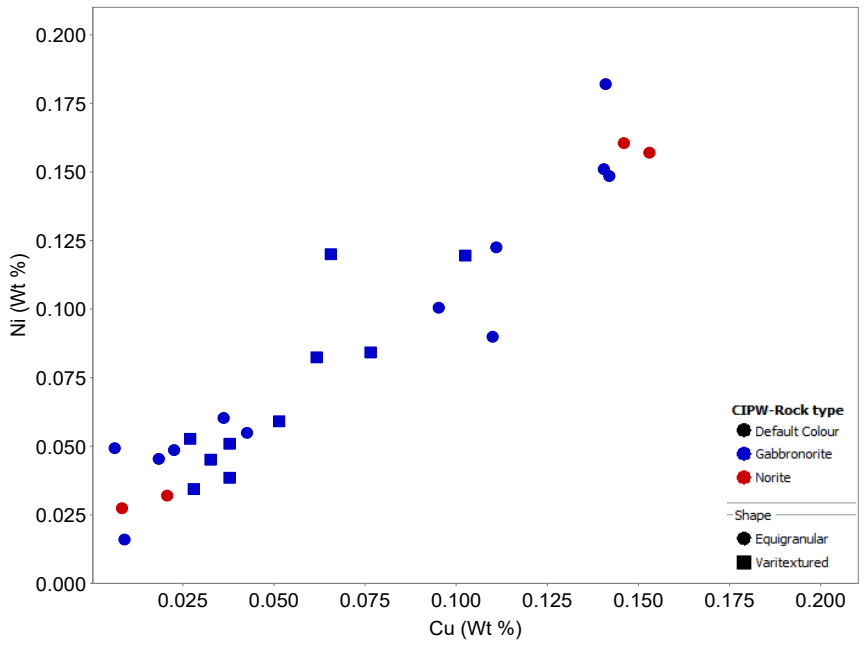

Figure 5.19 – Bivariate plot of Cu (Wt%) Vs Ni (Wt%) for Camp Lake Samples.

5.4. Summary and Comparison of Camp Lake Results with Other Parts of South Lac Des Iles complex Complex

The U-Pb age of 2690.56 ± 0.80 Ma, dominant lithologies (gabbronorites and norite), and geochemical signatures characterized by low concentrations of incompatible elements and high sulfide content of the Camp Lake Zone are broadly consistent with the data from previous studies at other zones of the SLDIC (Djon, 2018, Jonsson, 2023), this suggests a similar petrogenetic origin for the entire SLDIC. These similarities suggest that Camp Lake can be integrated into the overall genetic model of the complex, as proposed by Stone (2010), Barnes and Gomwe (2011), and Jonsson (2023), however, there are some differences including the degree of alteration, isotopic variations and mineralization style.

At Camp Lake alteration of the host rocks is mainly weak to moderate, and Sm-Nd isotopic data and trace element ratios indicate that crustal contamination remains limited and localized, whereas in the other zones there is evidence of higher degrees of alteration with the presence of the chlorite actinolite schist (Gomwe, 2008). Likewise, the Sm/Nd isotopic data for the other zones show a slightly more negative εNd values, particularly at the South Lac Des Iles complex Complex where εNd ranges from -0.5 to -3.5 compared to +0.30 to +1.12 for Camp Lake, suggesting a stronger signature of crustal contamination at the Roby and Offset zones.

High Pd/Pt ratios, sulfide assemblages, and textural associations between PGMs and sulphides are observed in Camp Lake and are similar to observations from the other zones of the SLDIC (Table 5.1). These observations suggest an effective dynamic of chalcophile element retention, favoring Pd enrichment. Camp Lake's sulfur isotope values ($\delta^{34}S$) ranging from –1 ‰ to +0.3 ‰ suggest a dominant mantle origin for the sulfides, with negligible crustal contribution. When compared with sulfur isotopic data from the other zones (Roby and Offset), the Camp Lake sulfur ($\delta^{34}S$) is the only purely mantle sulfur seen in the SLDIC. This homogeneous isotopic signature reinforces the hypothesis of a minimally contaminated magmatic system, in which early sulfide segregation played a key role in concentrating platinum group elements (PGEs) at the Camp Lake Zone, whereas at

other zones there may have a more significant crustal and/or secondary element to the sulfide and PGE enrichment.

Overall, the Camp Lake Zone exhibits geochemical and isotopic features that are consistent with a predominantly primary magmatic origin and distinguish it from the other intrusions of the SLDIC, reinforcing its significance within the broader metallogenic framework of the Lac des Iles Complex.

Table 5.1 – Comparative summary table of the South Lac Des Iles Complex. (Data from Michaud, 2001; Gomwe,2008, Lac Des Iles Mine Ltd 2023, Jonsson, 2023).

Feature	Camp Lake	Robby Zone	Offset Zone
Type of Mineralization	Dominant Pd stratiform, located in gabbronorite	Stratiform and magmatic breccia (multiple zones)	Dominant magmatic breccia
Age U-Pb	2690.56 ± 0.80 Ma	~2690 Ma	~2690 Ma
Dominant lithology	Gabbronorite, Norite	Gabbronorite, Norite, Pyroxenite	Gabbronorite, Norite, Pyroxenite
Location depth	~1.8 km (deepest area of SLDIC)	Shallower (~1.2 km)	Intermediate (~1.5 km)
Dominant Alteration	Uralitization, chloritization, seritization	Uralitization, chloritization, seritization	Uralitization, chloritization, seritization
Dominant sulphides	Pyrrhotite, pentlandite, chalcopyrite, pyrite	Pyrrhotite, chalcopyrite, pentlandite	Pentlandite, chalcopyrite, pyrite
Ni/Cu ratio in sulphides	Variable, but correlated with Pd concentration	High Ni/Cu in Pd-rich areas	Moderate Ni/Cu, influence of fluids
PGM dominants	Merenskyite, Moncheite, Michenerite, Kawazulite	Moncheite , Merenskyite , Kawazulite	Sperrylite , Moncheite , Merenskyite , Michenerite
Pd/Pt ratio	~7.50	~12	~13.6
S/Se ratio	915–4207 (often < mantle)	1200–4500 (variability with depth)	1000–4300 (influence of Se-enriched fluids)
Sulphur isotopes ($\delta^{34}S$)	–1 ‰ to +0.3 ‰: homogeneous mantle origin	– 0.5 ‰ to +2 ‰: slight crustal contribution	– 0.37‰ to +3.28‰: mantle-crustal mixture
Incompatible elements	Weak (Zr, Nb, Th, La); Differentiated and depleted magma	Medium to high; More marked crustal influence	Variables; sometimes enriched by remobilization
Crustal contamination	Localized, detected by Th/Yb, Nb/Yb, (La/Sm)PM > 4.03; and εNd (+0.30 to +1.12)	Moderate; εNd weakly negative (–0,52 to +2,14)	Moderate to strong; εNd negative (–3.472 to 0.384)
Source of Sulphur	Mantellic, not very fractionated	Mantellic with crustal influence	Magmatic breccia, structural trapping
Pd Enrichment	Controlled by early sulphide segregation	Influenced by successive magmatic injections	Controlled by trapping and remobilization

Feature	Camp Lake	Robby Zone	Offset Zone
Type of Mineralization	Dominant Pd stratiform, located in gabbronorite	Stratiform and magmatic breccia (multiple zones)	Dominant magmatic breccia

Chapter 6 - Conclusions

The Camp Lake Zone represents a distinct magmatic domain within the South Lac Des Iles complex Complex (SLDIC), exhibiting similarities and differences with the Roby–Offset Zones at the SLDIC. The integration of petrographic, geochemical, and isotopic data indicates that Camp Lake magmatism was primarily controlled by fractional crystallization of mantle-derived magma, followed by localized crustal contamination and late-stage hydrothermal alteration (Barnes and Gomwe, 2011; Jonsson, 2023).

The Sm–Nd isotopic compositions (εNd = 0.30 to +1.12) indicate derivation from a subduction-modified lithospheric mantle source, slightly enriched through limited assimilation of crustal components. In contrast, the $\delta^{34}S$ values (–1.1 to +0.3 ‰) primarily constrain the origin of sulfur rather than the magma itself, and their restricted range—together with the generally low S/Se ratios—supports a dominantly mantle-derived sulfur component with only minor external contributions. This combination of Nd and S isotope systematics suggests that Camp Lake magmas evolved in a semi-open system where mantle-derived melts experienced limited interaction with felsic country rocks during ascent and emplacement (DePaolo, 1981; Faure & Mensing, 2005).

Geochemically, the Camp Lake rocks exhibit calc-alcaline to komatiitic basalt compositions with variations in La/Sm, Th/Nb, and Cu/Zr ratios. These variations are consistent with fractional crystallization of pyroxene and Fe–Ti oxides, as well as sulfide segregation at moderate to high R-factors, which enhanced the selective partitioning of Pd into immiscible sulfide melts (Naldrett, 2004; Barnes, 2006). The vertical distribution of Pd within drill holes 22-711 and 22-712—where Pd peaks coincide with minima in Cu/Pd and S/Se, further supports the interpretation that Pd enrichment is magmatic in origin, governed by high metal-silicate partitioning efficiency rather than secondary remobilization (Stone et al., 2003; Jonsson, 2023).

Petrographic evidence, including the replacement of primary pyroxene by tremolite–actinolite and pervasive sericitization of plagioclase, suggests that the intrusion underwent post-magmatic alteration under lower amphibolite to greenschist facies conditions. However, the primary cumulate textures and mineralogical relationships remain preserved,

demonstrating that the system retained much of its original magmatic signature (Gomwe, 2008).

Overall, the Camp Lake Zone reflects a hybrid magmatic system, derived from a subduction-modified mantle source with limited crustal assimilation. The combination of isotopic homogeneity, trace element patterns, and PGE distribution indicates that the Camp Lake Zone represents an intermediate geochemical domain compared to crustally influenced Roby–Offset intrusions. This transitional character provides key evidence for a continuum of magmatic processes within the South Lac Des Iles complex Complex, highlighting the role of magma–sulfide interaction, variable R-factors, and subtle crustal contamination in generating the Pd mineralization observed at Camp Lake (Barnes and Gomwe, 2011; Jonsson, 2023; Duran, 2022).

References

Abbey, A.L., Barker, S.L.L., and Fiorentini, M.L., 2024. Transient hydrothermal circulation during cooling of mafic intrusions: Microstructural controls on fluid pathways and alteration intensity. Journal of Petrology, v. 65, article egaa123.

Ahmed, A.H., 2022. Magmatic sulfide mineralization in mafic–ultramafic intrusions: Textures, processes, and implications for metal enrichment. Ore Geology Reviews, v. 144, article 104840.

Backeberg, N., 2014. Damaged goods: Regional deformation history and structural controls on the Hammond Reef gold deposit, Atikokan, Ontario. MSc thesis, McGill University, Montréal, Québec, 210 p.

Barnes, S.-J. and Gomwe, T.S., 2010. Composition of the Lac des Iles magma and implications for the origin of the ore. 10th International Platinum Symposium, Program Abstracts, Ontario Geological Survey, Miscellaneous Release, Data 269.

Barnes, S.J., and Gomwe, T. 2011. The Pd deposits of the Lac des Îles Complex, Ontario: Magmatic and hydrothermal processes in the formation of the world's most Pd-rich intrusion-hosted deposit. Mineralium Deposita, v. 46(8), p. 933–954.

Boudreau, A., Djon, M.L., Tchalikian, A., and Corkery, J., 2014. The Lac des Iles palladium deposit, Ontario, Canada part 1: The effect of variable alteration on the Offset Zone. Mineralium Deposita, v. 49, p. 625–654.

Brown, M., Johnson, T.E., and Gardiner, N.J., 2022. Secular evolution of the continental crust and lithospheric mantle. Earth-Science Reviews, v. 231, article 104065.

Brugmann, G.E., Naldrett, A.J., and Macdonald, A.J., 1989. Magma mixing and constitution zone refining in the Lac des Iles Complex, Ontario; genesis of platinum-group element mineralization. Economic Geology, v. 84, p. 1557–1573.

Brügmann, G.E., Reischrnann, T., Naldrett, A.J., and Sutcliffe, R.H., 1997. Roots of an Archean volcanic arc complex; the Lac des îles area in Ontario: Canada. Precambrian Research, v. 81, p. 223–239

Card, K. D., 1990. A review of the Superior Province of the Canadian Shield, a product of Archean accretion. Precambrian Research, v. 48, p. 99–156.

Card, K.D. and Ciesielski, A., 1986. Subdivisions of the Superior Province of the Canadian Shield. Geoscience Canada, v. 13(1), p. 5–13.

D. Peck, and L. Djon, LDI Deposit, Comprehensive Review, Sept 2020. North American Palladium, p. 11–19.

Dare, S. A. S., Barnes, S.-J., Beaudoin, G., Méric, J., Boutroy, E., and Potvin-Doucet, C. 2014. Trace elements in magnetite as petrogenetic indicators. Mineralium Deposita, v. 49(6), 785–796.

Decharte, D., Hofton, T., Marrs, G., Olson, S., Peck, D., Perusse, C., Roney, C., Taylor, S., Thibodeau, D., and Young, B., 2018. Feasibility study for Lac des Iles mine incorporating underground mining of the Roby Zone. North American Palladium, NI 43-101 Technical Report, 435p.

Denis. D et al., 2018. Feasibility Study for Lac des Iles Mine Incorporating Underground Mining of the Roby Zone, North American Palladium Ltd. Thunder Bay, Ontario, Canada p. 31–35

Djon, M. L. N., & Barnes, S.-J. 2012. Changes in sulfides and platinum-group minerals with the degree of alteration in the Roby, Twilight, and High Grade Zones of the Lac des Iles Complex, Ontario, Canada. Mineralium Deposita, v. 47, p, 875–896.

Djon, M.L., 2017. Petrogenesis and metallogenesis of the ultramafic layered North Lac des Iles intrusion in the Lac des Iles Complex, Ontario, Canada. Unpublished doctoral thesis, Queen's University, p. 1–297.

Djon, M.L., Olivo, G.R., Miller, J.D., and Peck, D.C., 2017, Stratiform Platinum-Group Element Mineralization in the Layered Northern Ultramafic Center of the Lac des Iles Intrusive Complex, Ontario, Canada. Ore Geology Review, OI.org/10.1016/j.oregeorev.2017 .03.011

Djon, M.L., Peck, D.C., Olivo, G.R., Miller, J.D., and Joy, B., 2018. Contrasting styles of Pd-rich magmatic sulfide mineralization, Lac des Iles Intrusive Complex, Ontario, Canada. Economic Geology, v. 113, p. 741–767.

Dubé, B., Mercier-Langevin, P., Hannington, M., Lafrance, B., and Creaser, R., 2010. The Hammond Reef gold deposit, Superior Province, Ontario: An example of Archean orogenic gold mineralization in tonalitic host rocks. Economic Geology, v. 105(6), p. 1147–1169.

Duran, C.J., Barnes, S.-J., and Corkery, J.T., 2016. Geology, petrography, geochemistry, and genesis of sulfide-rich pods in the Lac des Iles palladium deposits, western Ontario, Canada. Mineralium Deposita, v. 51, p. 509–532.

Fiorentini, M.L., Mole, D.R., Barnes, S.J., et al., 2021. Refertilization of the lithospheric mantle and its role in the generation of metal-fertile magmas. Ore Geology Reviews, v. 133, article 104210.

Fouillard, G., 2023. The Archean Hammond Reef deposit: The formation of an orogenic gold deposit in a contractional step-over zone along a major strike-slip fault system. MSc thesis, Laurentian University, Sudbury, Ontario, 187 p.

Gerstenberger, H., and Haase, G., 1997. A highly effective emitter substance for mass spectrometric Pb isotope ratio determinations. Chemical Geology, v. 136(3–4), p. 309–312.

Gomwe, T. 2008. Geology and Mineralization of the Lac des Iles Complex. In: Platinum-Group Elements in Magmatic Ore Deposits. Springer, p. 123–145.

Goodwin, A., 1978. Archean crust in the Superior Geotraverse area: Geologic overview, in Smith, I.E.M. and Williams, J.G., eds, Proceedings Archean Geochemistry Conference. University of Toronto press, p. 73–106.

Good, D.J., Crocket, J.H., and Watkinson, D.H. 2000. Petrology, Geochemistry, and Origin of the Lac des Iles Palladium Deposit, Northwestern Ontario. Economic Geology, v. 95(5), p. 1027–1066.

Grützner, T., Fonseca, R.O.C., Ballhaus, C., Münker, C., and Weyer, S., 2021. Experimental investigation of Ru isotope fractionation between metal, silicate and sulfide melts. Geochimica et Cosmochimica Acta, v. 293, p. 1–18.

Hawkesworth, C.J., Cawood, P.A., Dhuime, B., and Kemp, A.I.S., 2017. Earth's continental lithosphere through time. Nature Geoscience, v. 10, p. 521–527.

Heaman, L.M., and Easton, R.M., 2006. Preliminary U/Pb geochronology results: Lake Nipigon Geoscience Initiative. Ontario Geological Survey, Miscellaneous Release – Data 191.

Hinchey, J.G. and Hattori, K.H., 2005. Magmatic mineralization and hydrothermal enrichment of the High-Grade Zone at the Lac des Iles palladium mine, northern Ontario, Canada. Mineralium Deposita, v. 40, p. 13–23.

Impala Canada, 2017. Technical Report on the Lac des Iles Palladium Mine. Impala Canada.

Impala Platinum Holdings Limited, 2022. Mineral Resource and Mineral Reserve Statement as of 30 June 2022. Impala Platinum Holdings Limited.

Jahn, B.-M., Capdevila, R., Liu, D., Vernon, A., and Zhang, J. 2001. The Archean Dongshan greenstone belt in the northern Hebei Province, China: Nd isotopic evidence for early continental crustal growth. Precambrian Research, v. 107(3–4), p. 253–273.

Jian, J., Li, C., Ripley, E.M., and Maier, W.D., 2024. Hydrothermal modification of magmatic sulfides in mafic–ultramafic intrusions: Textural re-equilibration and redistribution of chalcophile elements. Ore Geology Reviews, v. 170, article 105512.

Johnson, T.E., Brown, M., Gardiner, N.J., et al., 2019. The Archean lithospheric mantle: A composite of depleted and refertilized domains. Nature Reviews Earth & Environment, v. 1, p. 1–17.

Jonsson, J, 2023. Petrogenesis of mineralized horizons in the Offset and Creek zones, Lac des Iles Complex, N. Ontario, p. 146–168.

Karykowski, B.T., and Maier, W.D., 2017. Platinum group element partitioning and fractionation in mafic–ultramafic magmatic systems: Controls on Pd-rich mineralization. Ore Geology Reviews, v. 90, p. 1020–1040.

Krogh, T.E., 1973. A low-contamination method for hydrothermal decomposition of zircon and extraction of U and Pb for isotopic age determinations. Geochimica et Cosmochimica Acta, v. 37(3), p. 485–494.

Lavigne, M.J. and Michaud, M.J., 2001. Geology of North American Palladium Ltd.'s Roby Zone deposit, Lac des Iles. Exploration and Mining Geology, v. 10, p. 1–17.

Lesher, C. M., Burnham, O. M., Keays, R. R., Barnes, S. J., & Hulbert, L. 2001. Trace-element geochemistry and petrogenesis of barren and ore-associated komatiites. The Canadian Mineralogist, v. 39(2), p. 673–696

Liu, J., Li, C., Maier, W.D., Ripley, E.M., and Yang, S., 2023. Copper isotope evidence for sulfide fractionation and lower crustal foundering in continental crust formation. Nature Communications, v. 14, article 1234.

Locmelis, M., Fiorentini, M.L., and Barnes, S.J., 2020. Partitioning and redistribution of chalcophile and highly siderophile elements during magmatic and hydrothermal processes in mafic–ultramafic systems. Ore Geology Reviews, v. 118, article 103338.

Ludwig, K.R., 2009. Isoplot 3.71: A geochronological toolkit for Microsoft Excel. Berkeley Geochronology Center, Special Publication No. 4, 77 p.

Maier, W.D., Barnes, S.-J., and de Waal, S.A. 1998. Exploration for magmatic Ni-Cu-PGE sulphide deposits: a review of recent advances in the use of geochemical tools, and their application to some South African ores. South African Journal of Geology, v. 101(3), p. 237–253.

Mansur, E.T., Holwell, D.A., McDonald, I., and Boyce, A.J., 2020. Fractionation of platinum group elements during crystallization of magmatic sulfides: Insights from experimental and natural systems. Chemical Geology, v. 553, article 119803.

Mattinson, J.M., 2005. Zircon U–Pb chemical abrasion ("CA-TIMS") method: Combined annealing and multi-step partial dissolution analysis for improved precision and accuracy of zircon ages. Chemical Geology, v. 220(1–2), p. 47–66.

McCracken, T., Kanhai, T., Bridson, P., McBride, W.R., Small, K., and Penna, D.N, 2014. Technical Report on the Lac des Iles Mine, Ontario, Canada. Prepared for North American Palladium Ltd. in accordance with National Instrument 43-101 Standards of Disclosure for Mineral Projects.

Metallogeny, the Evolution of Geological Provinces, and Exploration Methods. Geological Association of Canada, Mineral Deposits Division, Special Publication No. 5, p. 903–928.

Mole, D.R., Fiorentini, M.L., Thebaud, N., et al., 2020. Archean mantle metasomatism and its role in the generation of enriched mafic magmas. Earth and Planetary Science Letters, v. 547, p. 116–468.

Peck, D., Houle, M. G., and Smith, M. P, 2016. Geology, Petrology, and Controls on PGE Mineralization of the Southern Roby and Twilight Zones, Lac des Iles Mine, Canada, 43p.

Peck, D., Houle, M.G., and Smith, M.P, 2016. A review of magmatic Ni-Cu-PGE sulfide deposit models and implications for exploration in the Lake Superior region. Economic Geology, v. 111(4), p. 833–858.

Peck, D.C., Djon, L., McLean, C., DeSchutter, G., Maxwell, J., Privet, K., Descharte, D., Roney, C., Huminicki. M., and Stewart, R., 2016. The Lac Des Iles PGE-Cu-Ni Deposit, Canada: An organized Mega-Breccia Unit? Institute on Lake Superior Geology 62nd Annual Meeting Abstract, 115 p.

Pei, Y., Chen, M., Zhao, Y., et al. 2025. The Evolution of Permian Mafic–Ultramafic Magma of the Yunhai Intrusion in the Northern Tianshan, Northwest China, and Its Implications for Cu-Ni Mineralization. Minerals, v. 15(2), 102.

Percival, J. A., 2007. Geology and metallogeny of the Superior Province, Canada, in Goodfellow, W. D., ed., Mineral Deposits of Canada: A Synthesis of Major Deposit-Types, District

Percival, J. A., Sanborn-Barrie, M., Skulski, T., Stott, G. M., Helmstaedt, H., and White, D. J., 2006. Tectonic evolution of the western Superior Province from NATMAP and Lithoprobe studies. Canadian Journal of Earth Sciences, v. 43, p. 1085–1117.

Percival, J.A., Skulski, T., Sanborn-Barrie, M., Stott, G.M., Leclair, A.D., Corkery, M.T., and Boily, M., 2012. Geology and tectonic evolution of the Superior Province, Canada, in Tectonic Styles in Canada: The Lithoprobe Perspective. Geological Association of Canada, Special Paper 49, p. 321–378.

Pochon, A., Boulvais, P., and Dini, A., 2023. Hydrothermal alteration and fluid–rock interaction in mafic intrusions: Insights from mineral chemistry and microtextural evolution. Lithos, v. 446–447, article 107182.

Ripley, E. M., and Li, C. 2013. Sulfide Saturation in Mafic Magmas: Is External Sulfur Required for Magmatic Ni-Cu-(PGE) Ore Genesis? Economic Geology, v. 108(1), p. 45–58.

Šegvić, B., Slovenec, D., and Badurina, L., 2022. Major and rare earth element mineral chemistry of low-grade assemblages inform dynamics of hydrothermal ocean-floor metamorphism in the Dinaridic Neotethys. Geological Magazine, v. 160(3).

Schisa, P., Boudreau, A., Djon, M.L., Tchalikian, A., and Corkery, J., 2015. The Lac des Iles palladium deposit, Ontario, Canada, Part II: Halogen variations in apatite. Mineralium Deposita, v. 50, p. 339–355.

Skulski, T., Corkery, M.T., Stone, D., Whalen, J.B., and Stern, R. A., 2000. Geological and geochemical investigations in the Stull Lake-Edmund Lake greenstone belt and granitoid rocks of the northwestern Superior Province, in Report of Activities 2000. Manitoba Industry Trade and Mines, Manitoba Geological Survey, p. 117–128.

Smith, W. D., Fay, L., Mungall, J. E., Shahabi Far, M., and Djon, L. 2024. Olivine compositions reveal an andesitic parent magma for the Archean palladium-mineralized Lac des Iles Complex of Ontario, Canada. Mineralium Deposita, p. 11–20.

Stacey, J.S., and Kramers, J.D., 1975. Approximation of terrestrial lead isotope evolution by a two-stage model. Earth and Planetary Science Letters, v. 26(2), p. 207–221.

Stern, R., Hanson, G., and Shirey, S., 1989. Petrogenesis of Mantle-derived, LILE-enriched Archean Monzodiorites and Trachyandesites (Sanukitoids) in Southwestern Superior Province

Stockwell, C. H., 1972. Revised Precambrian time scale for the Canadian Shield. Geological Survey of Canada, Paper 72–52.

Stone, D. and Davis, D.W., 2006. Revised tectonic domains of the south-central Wabigoon subprovince, in Summary of Field Work and Other Activities 2006. Ontario Geological Survey, Open File Report 6192, p. 11–1 to 11–18.

Stone, D., Lavigne, M.J., Schnieders, B., Scott, J., and Wagner, D., 2003. Regional geology of the Lac des Iles area: Ontario Geological Survey Open File Report, 6120, p. 15–25.

Stone, W.E., Archibald, D.A., Barnes, S.-J., and Watkinson, D.H. (2003). Age and Origin of Platinum-Group Element Mineralization in the Lac des Iles Intrusion, Northwestern Ontario. Economic Geology, 98, 195-209.

Stott, G. M., 1997. The Superior Province, Canada, in de Wit, M.J. and Ashwal, L.D., ed., Greenstone Belts. Oxford Monographs on Geology and Geophysics, v. 35, p. 480–507.

Stott, G. M., Corkery, M. T., Percival, J. A., Simard, M., and Goutier, J., 2010. A revised terrane subdivision of the Superior Province. Summary of Field Work and Other Activities 2010, Ontario Geological Survey, Open File Report 6260, p. 20-1 to 20-10.

Suraj, Kabir S., et al. 2024. Ab Initio Investigation of Magnetism and Stability in Nb Doped Magnetite. Journal of Magnetism and Magnetic Materials, v. 594, article 171197.

Sutcliffe, R.H. and Smith, A.R., 1988. Precambrian geology of the plutonic rocks in the Lac des Iles Tib Lake area, district of Thunder Bay. Ontario Geological Survey, Preliminary Map P.3098, 1:50000.

Sutcliffe, R.H. and Sweeny, J.M., 1986. Precambrian geology of the Lac des Iles Complex, district of Thunder Bay. Ontario Geological Survey, Preliminary Map P.3047, 1:15840.

Technical Report Lac des Iles Mine, Ontario, Incorporating Prefeasibility Study Offset Zone Phase I, p. 284.

Thurston, P. C. and Chivers, K. M., 1990. Secular variation in greenstone sequence development emphasizing Superior Province, Canada. Precambrian Research, v. 46, p. 21–58.

Thurston, P.C., 1991. Archean geology of Ontario, in Thurston, P.C., Williams, H.R., Sutcliffe, R.H., and Stott, G.M., eds., Geology of Ontario. Ontario Geological Survey, Special Volume 4, p. 73-78.

Thurston, P.C., Osmani, I.A. and Stone, D., 1991. Northwestern Superior Province: review and terrane analysis. In: Thurston, P.C., Williams, H.R., Sutcliffe, H.R., Stott, G.M. (Eds). Geology of Ontario. Ontario Geological Survey, Special volume 4, part 1, p. 81–141.

Tomlinson, K.Y., Davis, D.W., Stone, D., and Hart, T.R., 2003. U-Pb age and Nd isotopic evidence for Archean terrane development and crustal recycling in the south-central

Wabigoon subprovince, Canada. Contributions to Mineralogy and Petrology, v. 144, p. 684–702.

Tomlinson, K.Y., Stott, G.M., Percival, J. A., and Stone, D., 2004. Basement terrane correlations and crustal recycling in the western Superior Province: Nd isotopic character of granitoid and felsic volcanic rocks in the Wabigoon subprovince, N. Ontario, Canada. Precambrian Research, v. 132, p. 245–274.

Wang, Z., Wilde, S.A., Yang, J.H., et al., 2020. Heterogeneous Archean lithospheric mantle revealed by trace element and isotopic variations in mafic intrusions. Precambrian Research, v. 345, p. 105–757.

Wei, C., Li, C., Ripley, E.M., Maier, W.D., and Liu, J., 2023. Behavior of palladium during fractionation of sulfide liquid: Constraints from the Kalatongke Cu–Ni intrusion, Xinjiang, NW China. Ore Geology Reviews, v. 151, article 105187.

Yang, Q., Li, C., Ripley, E.M., et al., 2022. Mantle heterogeneity and metasomatism recorded in Archean mafic–ultramafic systems. Lithos, v. 418–419, p. 106–652.

Zhang, H., Yang, J., and Li, X., 2024. Trace-element and Nd–Hf isotopic constraints on enriched Archean lithospheric mantle domains. Precambrian Research, v. 392, article 107056.

Appendix I

Petrographic Descriptions of Thin Sections

Thin section:22-711-001 Sample ID: UU22-101534		Drill hole:22-711		Depth:905.56 m
Mineral (Interpreted Pre-alteration)	%	Mineral (actual)	%	Details
Plagioclase	75	Plagioclase	70	0.2-5.0 mm, subhedral to anhedral to anhedral, frequent polysynthetic twins, rare fractures. Low alteration in sericite and chlorite.
		Epidote and sericite	3	Occur as fine inclusions within altered plagioclase grains and as fine-grained aggregates developed along grain boundaries and around altered plagioclase crystals.
Pyroxene	20	Orthopyroxene	14	0.3 –4.0 mm, greyish tint in PPL, oblique extinction in XPL, partially replaced by actinolite-tremolite.
		Clinopyroxene	5	Subhedral to anhedral, inclined extinctions, moderate amphibole and chlorite alteration.
		Tremolite-actinolite	3	Fibrous interstitial aggregates replacing pyroxenes.
Sulfides	3	Pyrrhotite	2	Disseminated grains, anhedral, silicate interstitials.
		Chalcopyrite	1	Fine interstitial grains associated with pyrrhotite.
Oxides	2	Magnetite/Ilmenite	2	Grains subhedral to anhedral, interstitial to silicates.
Comment: Sample shows weak alteration. Plagioclase and pyroxenes form the dominant assemblage, with pyroxenes partially replaced by fibrous actinolite–tremolite. Disseminated pyrrhotite and chalcopyrite occur as fine interstitial grains. Minor magnetite–ilmenite is also present.				

Thin section:22-711-005 Sample ID: UU22-101534		Drill hole:22-711		Depth: 951.71 m
Mineral (Interpreted Pre-alteration)	%	Mineral (actual)	%	Details
Plagioclase	80	Plagioclase	70	The plagioclase grains range from 0.3 to 5. mm in size. The majority of the sample consists of cumulate plagioclase (>90%) with well-developed polygonal triple junctions. Larger grains are subhedral to anhedral, and smaller grains exhibit rounded textures. Weak deformation twinning is present. Alteration is minor, with sericitization visible along fractures and grain boundaries. Some grains are partially replaced by fine-grained white mica and chlorite.
		Sericite	8	Fine-grained occurs as patches developed within altered plagioclase grains and as fine aggregates along grain boundaries and fractures, particularly in more strongly altered zones.
		Epidote	2	Rare patches of very fine-grained epidote occur interstitially and within alteration zones.
Pyroxene	16	Orthopyroxene	12	Grains range from 0.4 to 4.0 mm. Pyroxene is subhedral to anhedral and shows moderate to strong alteration to amphibole and chlorite. Partial uralitization is observed, with amphibole rimming pyroxene grains. Some grains display fractures filled with secondary alteration minerals.
		Amphibole (Tremolite–actinolite)	3	Found as a replacement product of pyroxene, forming fine-grained aggregates along grain boundaries and within fractures.
		Chlorite	1	Occurs in association with amphibole in altered pyroxene. Forms fine-grained rims around pyroxene crystals.
Sulfides	3	Pyrite	2	Pyrite occurs as subhedral to euhedral grains ranging from 0.02 to 0.5 mm. Forms clusters and is interstitial between silicate minerals. Minor replacement textures are visible.
		Chalcopyrite	1	Present in trace amounts, mostly in association with pyrite. Small blebs (0.01–0.2 mm) are interstitial or along grain boundaries.
Oxides	1	Magnetite	1	Very fine- to fine-grained. Interstitial, disseminated.
Comment: Sample consists mainly of plagioclase–pyroxene cumulate–textured rock. The plagioclase framework is well preserved, with slight alteration to fine sericite and minor chlorite. Pyroxenes show moderate replacement by amphibole (tremolite–actinolite) and chlorite. Sulphides are minor and occur as disseminated pyrite with some chalcopyrite.				

Thin section:22-711-010 Sample ID: UU22-101650		Drill hole:22-711		Depth: 1014.7 m
Mineral (Interpreted Pre-alteration)	%	Mineral (actual)	%	Details
Plagioclase	60	Plagioclase	50	Clear to white, subhedral to anhedral grains range from 0.3 to 4 mm in size., mostly millimetric. Polysynthetic twinning locally visible. Fractures and grain margins contain fine sericite and minor epidote.
		Epidote and sericite	3	occur as fine alteration products along plagioclase fractures and grain edges, with sericite forming thin, discontinuous white-mica patches and epidote appearing as very fine grains concentrated at grain margins and within microfractures.
Pyroxene	25	Amphibole (Tremolite-actinolite)	20	Pale to medium green amphibole, subhedral to anhedral. Occurs in irregular patches and aggregates replacing former pyroxene. Moderate birefringence.
		Pyroxene (relict)	3	Partially preserved cores within tremolite–actinolite–chlorite aggregates. Irregular, discontinuous outlines.
		Chlorite	6	Green, low-interference patches between plagioclase and amphibole. Occurs along grain margins and within altered pyroxene zones.
Sulfides	10	Pyrite	3	Bright white, subhedral to anhedral grains (0.02–0.5 mm). Occurs isolated or in small interstitial clusters.
		Chalcopyrite	1	Fine anhedral grains intergrown with pyrite. Yellow-gold reflectance.
		Sphalerite	3	Dark gray to brownish-gray, low-reflectance anhedral patches (0.2–5 mm). Occurs interstitially between magnetite and sulfides.
Oxides	5	Magnetite	10	Dominant opaque phase. Anhedral grains forming irregular to massive patches with light to medium gray reflectance. Sharp contacts with sulfides. Local thin rims of hematite and chlorite.
		Carbonate	1	Fine-grained material filling fractures within the silicate matrix.
Comment: The sample shows a granular to equigranular texture dominated by plagioclase, with tremolite–actinolite, chlorite, and minor relict pyroxene forming irregular mafic aggregates. Magnetite occurs as abundant anhedral opaque patches in sharp contact with pyrite, chalcopyrite, and sphalerite. Plagioclase contains fine sericite–epidote alteration along fractures and grain margins, and carbonate fills narrow fractures within the silicate matrix. Based on modal proportions and texture, the sample corresponds to an varitextured gabbronorite.				

Thin section:22-711-015 Sample ID: UU22-101677		Drill hole:22-711		Depth: 1040.11 m
Mineral (Interpreted Pre-alteration)	%	Mineral (actual)	%	Details
Plagioclase	58	Plagioclase	52	Clear to white, subhedral to anhedral grains range from 0.2 to 3.3 mm in size. Polysynthetic twinning locally visible. Fractures and grain margins contain fine sericite–epidote alteration.
		Sericite + Epidote	6	Fine white mica and very fine epidote grains along plagioclase fractures and grain edges, forming thin discontinuous patches and microfracture fillings.
Pyroxene	38	Actinolite-tremolite	22	Pale to medium-green amphibole forming irregular aggregates, commonly replacing former pyroxene. Subhedral to anhedral grains with moderate birefringence.
		Pyroxene (relict)	4	Discontinuous orthopyroxene cores preserved within tremolite–actinolite–chlorite aggregates, locally showing fine clinopyroxene exsolution lamellae. Irregular outlines.
		Chlorite	5	Green, low-interference patches between plagioclase and amphibole and within altered pyroxene zones.
		Talc	7	Colourless to very pale grains with very low birefringence, occurring as soft, fibrous to platy replacement of mafic minerals along grain margins and fractures.
Sulfides	4	Pyrrhotite	2	Anhedral grains with grey-brown reflectance forming irregular interstitial patches, locally associated with chalcopyrite .
		Chalcopyrite	1	Fine anhedral yellow-gold grains intergrown with pyrite and pyrrhotite.
		Pentlandite	0.5	Pale bronze, weakly reflective anhedral grains, typically occurring as small blebs or flame-like intergrowths within pyrrhotite.
		Pyrite	0.5	Bright, highly reflective subhedral to anhedral grains (0.02–0.5 mm), isolated or in small interstitial clusters.
Comment: Sample exhibits a granular to equigranular texture dominated by plagioclase, with tremolite–actinolite, chlorite, talc, and minor relict pyroxene (locally with clinopyroxene exsolution lamellae) forming irregular mafic aggregates. Sulfides consist of pyrrhotite, pentlandite, pyrite, and chalcopyrite occurring as interstitial grains and small clusters. Plagioclase displays fine sericite–epidote alteration along fractures and grain margins. the sample corresponds to an equigranular gabbronorite.				

Thin section:22-711-022 Sample ID: UU22-101707		Drill hole:22-711		Depth: 1068.61 m
Mineral (Interpreted Pre-alteration)	%	Mineral (actual)	%	Details
Plagioclase	55	Plagioclase	50	Clear to white, subhedral to anhedral grains, generally ~0.5–2 mm; locally more coarse or finer, consistent with a variably textured gabbronorite. Polysynthetic twinning is locally visible.
		Sericite	2	Very fine white mica along plagioclase fractures and grain edges, forming thin, discontinuous patches (<0.1 mm).
		Quartz	5	Colourless, low-relief, anhedral to interstitial grains, generally ~0.2–1 mm, locally with weak undulatory extinction; occurs between plagioclase and mafic minerals.
Pyroxene	35	Tremolite-actinolite	20	Pale to medium-green amphibole forming irregular replacement aggregates of former pyroxene; subhedral to anhedral grains ~0.3–1.5 mm, moderate birefringence.
		Pyroxene (relict)	10	Discontinuous orthopyroxene cores, typically ~0.3–1.2 mm, locally showing fine clinopyroxene exsolution lamellae; irregular outlines within amphibole–chlorite domains.
		Chlorite	3	Green, low-interference patches ~0.2–1 mm, occurring between plagioclase and amphibole and within altered pyroxene zones.
Hornblende	2	Hornblende	2	Green-brown pleochroic amphibole, subhedral grains ~0.3–1 mm, occurring as discrete crystals or small clusters within mafic domains.
Biotite	5	Biotite	5	Grey-brown, anhedral disseminated grains, generally ~0.05–0.3 mm, occurring as small interstitial patches.
Sulfides	3	Pyrrhotite	2	Present as 0.01 to 0.5 mm disseminated grains, often in clusters in altered zones.
		Chalcopyrite	1	Trace fine anhedral yellow-gold grains (<0.1 mm), locally intergrown with pyrrhotite.
		Pentlandite	tr	Minimal present as inclusions in chalcopyrite.
Comment: The thin section shows a variably textured gabbronorite dominated by plagioclase and pyroxene-derived mafic minerals. Plagioclase (generally ~0.5–2 mm) is locally altered to sericite and carbonate along fractures and grain margins, with minor interstitial quartz. Mafic domains (~0.3–1.5 mm) consist of tremolite–actinolite, chlorite, talc, hornblende, biotite, and relict orthopyroxene with local clinopyroxene exsolution lamellae. Sulfides are sparse and occur as disseminated pyrrhotite and chalcopyrite with trace of pentlandite in small interstitial grains.				

Thin section:22-711-024 Sample ID: UU22-101737		Drill hole:22-711		Depth: 1095.12 m
Mineral (Interpreted Pre-alteration)	%	Mineral (actual)	%	Details
Plagioclase	65	Plagioclase	55	Clear to white, subhedral to anhedral laths, typically ~0.5–3 mm long; locally forming strongly aligned, variably textured domains with polysynthetic twinning.
		Sericite	5	Occurs along fractures and grain margins of plagioclase, forming thin, discontinuous patches (<0.1 mm). It also develops as thin films and veinlets within plagioclase grains, generally concentrated from the crystal core toward the grain edges.
Pyroxene	35	Tremolite-actinolite	26	Pale to medium-green amphibole forming irregular replacement aggregates of former pyroxene; subhedral to anhedral grains ~0.3–1.5 mm, moderate birefringence.
		Pyroxene (relict)	8	Discontinuous orthopyroxene cores, typically ~0.3–1.2 mm, locally with fine intergrowth clinopyroxene; irregular outlines within amphibole–chlorite domains.
		Chlorite	5	Green, low-interference patches ~0.2–1 mm, between plagioclase and amphibole and within altered pyroxene zones.
		Biotite	1	Brown pleochroic mica with strong interference colours and perfect cleavage; flakes ~0.2–1 mm, interstitial and along mafic grain margins.
Sulfides		Pyrrhotite	Tr	Pink brown, anhedral disseminated grains, generally ~0.05–0.3 mm, occurring as small interstitial patches.
		Chalcopyrite	Tr	Minor presence as interstitial grains (<0.1 mm), at the edge of the sulphides.
Comment: Varitextured leucogabbronorite, exhibits a massive cumulate texture with dominated by plagioclase laths (~0.5–3 mm) and pyroxene-derived mafic minerals. Plagioclase is locally altered to sericite along fractures and grain margins. Mafic domains (~0.3–1.5 mm) consist of tremolite–actinolite, chlorite, hornblende, biotite, and relict orthopyroxene with local clinopyroxene exsolution lamellae. Sulfides are sparse and occur as disseminated trace of pyrrhotite and chalcopyrite in small interstitial grains.				

Thin section:22-711-029 Sample ID: UU22-101707		Drill hole:22-711		Depth: 1140.31 m
Mineral (Interpreted Pre-alteration)	%	Mineral (actual)	%	Details
Plagioclase	35	Plagioclase	30	Clear to white subhedral to anhedral (~0.5–3 mm), locally forming aligned domains. Polysynthetic twinning is common and generally well preserved. Grains are moderately fractured and show extensive alteration, with sericite along cleavages and inclusions, and interstitial chlorite filling cracks and small patches.
		Sericite	5	Very fine grain (<0.1 mm) along fractures and grain margins, forming thin, discontinuous selvages.
		Quartz	3	Colourless, low-relief, anhedral to interstitial grains ~0.2–1 mm, locally showing weak undulatory extinction.
Pyroxene	50	Tremolite-actinolite	40	The original pyroxene is largely replaced by fine- to medium-grained pale to medium-green tremolite–actinolite forming bladed to fibrous subhedral to anhedral aggregates (~0.3–1.5 mm). Chlorite occurs along grain margins and in interstitial spaces.
		Pyroxene (relict)	12	Discontinuous orthopyroxene cores ~0.3–1.2 mm, locally with fine clinopyroxene exsolution lamellae.
		Chlorite	5	Developed along grain margins and in interstitial spaces.
Biotite	10	Biotite	5	Present in minor amounts as small brown pleochroic (~0.2–1 mm) with strong interference colours, occurring interstitially and along mafic grain margins; crystals are locally altered and rimmed by amphibole and chlorite.
Sulfides	5	Pyrrhotite	3	Disseminated pink-grey anhedral grains (~0.05–0.3 mm) occurring as small interstitial patches and as exsolution features within silicate minerals, locally forming minor clusters within altered silicate domains.
		Chalcopyrite	1.5	Anhedral, yellow-gold grains (<0.5 mm), locally intergrown with pyrrhotite.
		Pyrite	0.5	Very bright, pale yellow reflectance; often euhedral with cubic.
		Pentlandite	tr	Bronze-yellow to pale brownish tint under reflected light , anhedral to subhedral, occurs as granular aggregates (<0.1 mm) or intergrown with pyrrhotite and chalcopyrite.
Comment: In thin section, the rock displays a heterogeneous assemblage of plagioclase (~0.5–3 mm) and pyroxene-derived mafic minerals. Plagioclase is moderately fractured and shows partial alteration to sericite along grain margins and fractures, with minor interstitial quartz present. Mafic domains (~0.3–1.5 mm) are composed mainly of tremolite–actinolite, chlorite, hornblende, biotite, and relict orthopyroxene, locally preserving clinopyroxene exsolution lamellae. These features indicate a moderate hydrothermal overprint superimposed on the primary magmatic assemblage. Sulfides are sparse and occur as disseminated pyrrhotite with trace pentlandite and chalcopyrite. Based on these petrographic characteristics, the thin section is classified as a varietextured mesogabbronorite				

Thin section:22-711-031 Sample ID: UU22-101804		Drill hole:22-711		Depth: 1157.4 m
Mineral (Interpreted Pre-alteration)	%	Mineral (actual)	%	Details
Plagioclase	40	Altered Plagioclase	30	Clear to white subhedral to euhedral laths (~0.5–3 mm), locally forming aligned domains. Polysynthetic twinning common and generally preserved. Grains moderately fractured.
		Sericite	3	Very fine (<0.1 mm) along cleavages, fractures and grain margins, forming thin discontinuous selvages and small patches.
		Epidote	2	Yellow-green, high-relief anhedral grains (~0.1–0.5 mm), commonly along plagioclase fractures and grain boundaries, locally forming small aggregates.
		Carbonate	2	Fine-grained carbonate (<0.2 mm) filling fractures and small interstitial patches within felsic domains.
Pyroxene	42	Pyroxene (relict)	15	Discontinuous orthopyroxene and clinopyroxene cores (~0.3–1.2 mm), locally with fine exsolution. Irregular grain boundaries; partially replaced by amphibole, chlorite and talc.
		Actinolite–tremolite	25	Pale to medium-green amphibole prismatic to forming bladed subhedral to anhedral aggregates (~0.3–1.5 mm), commonly aligned with foliation and replacing former pyroxene; grains are locally fractured.
		Talc	5	Very pale, low-birefringence platy to fibrous aggregates (<0.3 mm) along mafic grain margins and fractures, commonly associated with amphibole and chlorite.
	2	Hornblende	2	Green-brown pleochroic amphibole, subhedral grains (~0.3–1 mm), occurring in small clusters within mafic domains.
	8	Biotite	8	Brown pleochroic flakes (~0.2–1 mm) with strong interference colours; interstitial and along mafic grain margins; locally rimmed and partially replaced by chlorite and amphibole.
Sulfides	8	Pyrrhotite	6	Pink to pink grey, anhedral to subhedral grains (~0.05–0.3 mm), disseminated as small interstitial patches and minor clusters within altered silicates; commonly intergrown with pentlandite.

		Chalcopyrite	2	Yellow, moderate reflectance, anhedral grains (~0.05–0.2 mm), interstitial and along pyrrhotite margins; mostly disseminated.
		Pentlandite	Tr	Bronze-yellow reflectance, granular texture, associated with pyrrhotite.
Oxide		Magnetite	Tr	High reflectance, anhedral grains, minor accessory phase.
Comment: The thin section shows a vari-textured mesogabbronorite form by plagioclase (~0.5–3 mm) and pyroxene. Plagioclase is moderately fractured and partially altered to sericite, epidote and carbonate. Mafic domains (~0.3–1.5 mm) contain relict pyroxene cores overprinted by tremolite–actinolite, hornblende, chlorite, biotite and talc. Opaque phases include minor disseminated traces of magnetite and sulfide assemblage dominated by pyrrhotite with chalcopyrite and trace of pentlandite.				

Thin section: 22-711-032 Sample ID: UU22-101813		Drill hole:22-711		Depth: 1165.65 m
Mineral (Interpreted Pre-alteration)	%	Mineral (actual)	%	Details
Plagioclase	40	Plagioclase	30	Clear to white subhedral to anhedral aggregates (~0.5–3 mm), forming interlocking polygonal clusters rather than discrete laths. Grains moderately fractured.
		Sericite	5	Fine (<0.1 mm) along fractures, cleavages and grain margins, forming thin, discontinuous selvages and patchy replacement.
		Carbonate	2	Fine-grained carbonate (<0.2 mm) filling fractures and small interstitial pockets.
Pyroxene	47	Pyroxene	6	Discontinuous orthopyroxene/clinopyroxene cores (~0.3–1.2 mm), irregular boundaries, locally interloking.
		Tremolite–Actinolite	30	Pale to medium-green amphibole forming bladed subhedral to anhedral aggregates (~0.3–2 mm), commonly aligned with internal fabric and replacing former pyroxene.
		Talc	10	Colourless to very pale grains with very low birefringence, occurring as soft, fibrous to platy replacement of mafic minerals along grain margins and fractures.
		Chlorite	4	Green, low-interference anhedral patches (~0.2–1 mm) along amphibole and biotite margins and in interstitial spaces.
	3	Hornblende	2	Green-brown pleochroic amphibole (~0.3–1 mm), subhedral, occurring in small clusters within mafic domains.
	4	Biotite	2	Brown pleochroic flakes (~0.2–1 mm) with strong interference colours; interstitial and along mafic grain margins; locally rimmed by chlorite.
Sulfides	5	Pyrrhotite	5	Pink grey anhedral to subhedral grains (~0.05–0.4 mm), disseminated and forming small clusters; commonly intergrown with pentlandite.
		Pentlandite	1	Bronze-yellow granular blebs (<0.1 mm), typically flame-like within pyrrhotite.
		Chalcopyrite	2	Yellow, moderate-reflectance anhedral grains (~0.05–0.2 mm), interstitial and along pyrrhotite margins.
Oxide	1	Magnetite	1	Grey to light grey, high-reflectance anhedral grains (~0.05–0.3 mm), disseminated within mafic domains.
Comment: The thin section 22-711-032 displays a fine- to medium-grained, mostly equigranular gabbronorite, consist by plagioclase aggregates (~0.5–3 mm) and amphibole. Plagioclase forms interlocking subhedral to anhedral clusters, is moderately fractured, and shows partial replacement by sericite and minor carbonate. Mafic domains (~0.3–2 mm) contain relict pyroxene cores overprinted by tremolite–actinolite, chlorite, biotite and minor talc, the latter occurring along cleavage planes and grain margins. Opaque phases include disseminated magnetite as anhedral to subhedral grains and a sulfide assemblage dominated by pyrrhotite with pentlandite and subordinate chalcopyrite, occurring as interstitial grains, small clusters, and local veinlets within altered silicate domains.				

Thin section: 22-711-037 Sample ID: UU22-101866		Drill hole:22-711		Depth: 1215.23
Mineral (Interpreted Pre-alteration)	%	Mineral (actual)	%	Details
Plagioclase	36	Plagioclase	30	Clear to white subhedral to anhedral aggregates (~0.5–3 mm) forming tight interlocking clusters, showing polysynthetic twinning and irregular grain boundaries; grains moderately fractured with localized sericite overprint.
		Sericite	3	Very fine white mica (<0.1 mm) occurs along fractures, cleavage planes, and grain margins, forming thin discontinuous layers and patchy replacement zones.
		Carbonate	1	Fine-grained carbonate (<0.2 mm) filling fractures and small interstitial pockets.
Quartz	1	Quartz	1	Anhedral grains; low relief; undulatory extinction; interstitial or vein hosted.
Pyroxene	46	Pyroxene (relict)	6	Discontinuous orthopyroxene/clinopyroxene cores (~0.3–1.2 mm) with irregular boundaries.
		Actinolite-tremolite	34	Pale to medium-green amphibole forming elongate bladed to prismatic subhedral to anhedral aggregates (~0.3–2.5 mm), commonly aligned with internal fabric and replacing moderately to strongly altered pyroxene; cleavage is locally visible and some grains are fractured.
		Chlorite	5	Green, low-interference anhedral patches (~0.2–1 mm) along amphibole and biotite margins and in interstitial spaces.
		Talc	2	Very pale, low-birefringence platy, aggregates (<0.3 mm) along mafic grain margins and fractures.
Hornblende	2	Hornblende	2	Green-brown pleochroic amphibole (~0.3–1 mm), subhedral, occurring in small clusters within mafic domains.
Biotite	4	Biotite	4	Brown pleochroic flakes (~0.2–1 mm) with strong interference colours; interstitial and along mafic grain margins; locally rimmed by chlorite.
Sulfides	10	Pyrrhotite	6	Subhedral to anhedral grains; weak reflectance; intergrowth with pentlandite and chalcopyrite.
		Pentlandite	1	Bronze-yellow granular blebs (<0.1 mm), typically flame-like within pyrrhotite.
		Chalcopyrite	3	Yellow, moderate-reflectance anhedral grains (~0.05–0.3 mm), interstitial and along pyrrhotite margins.
		Pyrite	1	Bright, high-reflectance anhedral cubes to irregular grains (<0.1–0.2 mm), occurring as scattered blebs and small interstitial grains within chalcopyrite.

Oxide	1	Magnetite	1	Grey to light grey, anhedral to subhedral grains (~0.05–0.5 mm), disseminated and forming small clusters within pyrrhotite.
Comment: Fine- to medium-grained equigranular to interlocking gabbronorite, composed of plagioclase aggregates and amphibole-rich mafic domains. Plagioclase forms subhedral to anhedral clusters (~0.5–3 mm) with moderate fracturing and localized sericite and minor carbonate alteration. Mafic domains (~0.3–2.5 mm) contain relict pyroxene replaced by tremolite–actinolite, chlorite, biotite and minor talc. Quartz occurs as minor anhedral grains. Opaque minerals include disseminated magnetite and a well-developed sulfide assemblage dominated by pyrrhotite with pentlandite, chalcopyrite and minor pyrite, occurring as interstitial grains, small clusters within altered silicate domains.				

Thin section: 22-711-041 Sample ID: UU22-101904		Drill hole:22-711		Depth: 1249 m
Mineral (Interpreted Pre-alteration)	%	Mineral (actual)	%	Details
Plagioclase	37	Plagioclase	28	Milky to clear subhedral to anhedral mosaics (~0.4–2.5 mm), forming compact granular clusters; grains show irregular contacts, mild strain features, and scattered polysynthetic twinning.
		Sericite	5	Fine micaceous alteration (<0.1 mm) concentrated along fractures and grain margins, forming diffuse replacement zones.
		Carbonate	2	Pale, fine-grained patches (<0.2 mm) infilling microfractures and small interstitial pockets.
Pyroxene	45	Pyroxene (relict)	10	Residual orthopyroxene/clinopyroxene kernels (~0.3–1.0 mm) with subdued relief and irregular outlines.
		Actinolite–Tremolite	30	Pale green to medium green prismatic to tabular crystals (~0.3–2.5 mm), forming elongate bundles and patchy aggregates; commonly aligned and replacing former pyroxene.
		Chlorite	6	Green, low-interference masses (~0.2–1 mm) occupying cleavage traces and margins of amphibole and biotite.
		Talc	2	Very pale, silky aggregates (<0.3 mm) replacing pyroxene and amphibole along cleavage planes and fractures.
	2	Hornblende	2	Green-brown subhedral grains (~0.3–1.2 mm) occurring in discrete pockets within mafic zones.
	3	Biotite	3	Bronze to brown flakes (~0.2–1 mm) with moderate pleochroism; commonly intergrown with chlorite.
Sulfides	12	Pyrrhotite	6	Pink to pink grey anhedral to subhedral grains (~0.05–0.5 mm), forming clusters and interstitial patches; locally enclosing pentlandite blebs.
		Chalcopyrite	2	Yellow metallic grains (~0.05–0.3 mm), occurring along pyrrhotite margins and in narrow veinlets.
		Pentlandite	3	Pale bronze blebs (<0.1 mm), flame-like within pyrrhotite.
		Pyrite	1	Bright, high-reflectance anhedral grains (<0.1–0.2 mm), scattered as isolated blebs.
Comment: Fine- to medium-grained norite with a predominantly granular to interlocking texture. Plagioclase occurs as subhedral to anhedral aggregates (~0.4–2.5 mm) showing moderate fracturing and localized sericite–carbonate alteration. Mafic domains (~0.3–2.5 mm) contain relict pyroxene partially replaced by actinolite–tremolite, hornblende, chlorite, biotite and minor talc. Opaque minerals include sulfide assemblage dominated by pyrrhotite with pentlandite, chalcopyrite and minor pyrite, occurring as interstitial grains, small clusters and local veinlets within altered silicate domains.				

Thin section: 22-711-048 Sample ID: 101968		Drill hole:22-711		Depth: 1308 m
Mineral (Interpreted Pre-alteration)	%	Mineral (actual)	%	Details
Plagioclase	55	Plagioclase	42	Off-white to clear anhedral to subhedral grains (~0.4–2.5 mm) forming a patchy, granoblastic mosaic; grains show mild undulose extinction, irregular contacts, and scattered twinning.
		Sericite	8	Fine micaceous alteration (<0.1 mm) concentrated along fractures and grain margins, forming diffuse replacement zones.
Pyroxene	35	Pyroxene (relict)	10	Small, discontinuous relics (~0.2–0.8 mm) with subdued relief and irregular outlines, commonly enclosed within amphibole.
		Actinolite-Tremolite, Chlorite, talc	23	Pale green to grey-green subhedral to anhedral (~0.3–2.8 mm), forming elongate bundles and diffuse replacement fronts; grains locally bent or kinked.
		Talc	6	Very pale, silky aggregates (<0.3 mm) replacing pyroxene and amphibole along cleavage planes and fractures.
Biotite		Biotite	2	Bronze to brown flakes (~0.2–0.8 mm) with moderate pleochroism; commonly intergrown with chlorite.
Sulfides	10	Pyrrhotite	5	Bronze-grey anhedral to subhedral grains (~0.05–0.6 mm), forming clusters and interstitial patches; locally enclosing pentlandite blebs.
		Chalcopyrite	3	Yellow metallic grains (~0.05–0.3 mm), occurring along pyrrhotite margins and in narrow veinlets.
		Pentlandite	1	Pale bronze blebs (<0.1 mm), flame-like within pyrrhotite.
		Pyrite	Tr	Present as 0.01 to 0.5 mm disseminated grains, often associated with pyrrhotite and chalcocite.
Comment: Fine- to medium-grained varitextured gabbronorite. Plagioclase forms irregular anhedral to subhedral grain (~0.4–2.5 mm) showing mild strain features and localized sericite–carbonate overprint. The mafic component is dominated by actinolite–tremolite forming elongate bundles and aggregates that overtake small remnants of pyroxene; chlorite, biotite and minor talc occupy cleavage traces and margins, giving the mafic zones a layered, diffuse appearance. Opaque minerals include sulfide form by pyrrhotite as the main phase accompanied by chalcopyrite, pentlandite, and minor pyrite, occurring as disseminated.				

Thin section: 22-711-051 Sample ID: UU22-101994		Drill hole:22-711		Depth: 1333.00 m
Mineral (Interpreted Pre-alteration)	%	Mineral (actual)	%	Details
Plagioclase	68	Plagioclase	50	Light grey anhedral to subhedral grains (~0.4–2.3 mm) forming a loosely interlocking mosaic; uneven grain boundaries, mild undulose extinction, and scattered polysynthetic twinning.
		Sericite	6	Fine micaceous alteration (<0.1 mm) concentrated along fractures and grain margins, forming diffuse replacement halos.
		Carbonate	3	Pale, fine-grained patches (<0.2 mm) infilling microfractures and small interstitial pockets.
Pyroxene	25	Pyroxene (relict)	4	Small, irregular remnants (~0.2–0.7 mm) with subdued relief; commonly enclosed within amphibole.
		Actinolite-Tremolite (20% (within pyroxene zone)	20	Pale green to grey-green prismatic crystals (~0.3–2.6 mm), forming radiating clusters and elongate bundles; grains locally kinked or bent.
		Chlorite	5	Light green, low-interference masses (~0.2–1 mm) occupying cleavage traces and margins of amphibole and biotite.
		Biotite	3	Brown to bronze flakes (~0.2–0.9 mm) with moderate pleochroism; intergrown with chlorite in mafic zones.
		Hornblende	2	Green-brown pleochroic amphibole (~0.3–1 mm), subhedral, occurring in small clusters within mafic domains.
Sulfides	7	Chalcopyrite	3	Yellow metallic grains (~0.05–0.3 mm), occurring along pyrrhotite margins and in narrow veinlets.
		Pyrrhotite	3	Bronze-grey anhedral to subhedral grains (~0.05–0.6 mm), forming clusters and interstitial patches; locally enclosing pentlandite blebs.
		Pentlandite	1	Pale bronze blebs (<0.1 mm), flame-like within pyrrhotite.
		Pyrite	Tr	Bright, high-reflectance anhedral grains (<0.1–0.2 mm), at margin of chalcopyrite and pyrrhotite.
Comment: The thin section shows a fine- to medium-grained varitextured gabbronorite with a loosely interlocking to locally granoblastic texture. Plagioclase forms irregular anhedral to subhedral mosaics (~0.4–2.3 mm) displaying mild strain and localized sericite–carbonate alteration. Mafic zones (~0.3–2.6 mm) are dominated by actinolite–tremolite in radiating clusters and fibrous bundles surrounding small relict pyroxene; chlorite, biotite and minor talc fill cleavage traces and margins, giving these areas a diffuse, layered character. Opaque phases include sulfide network of pyrrhotite, pentlandite, chalcopyrite and minor pyrite, present as dispersed grains, clustered patches and narrow veinlets within altered silicates.				

Thin section: 22-711-055 Sample ID: UU22-102033		Drill hole:22-711		Depth: 1333.00 m
Mineral (Interpreted Pre-alteration)	%	Mineral (actual)	%	Details
Plagioclase	39	Plagioclase	32	Light grey anhedral to subhedral grains (~0.4–2.4 mm) forming a loosely packed granular mosaic; uneven contacts, mild undulose extinction, and scattered polysynthetic twinning.
		Sericite	7	Fine micaceous alteration (<0.1 mm) along fractures and grain margins, forming diffuse replacement films.
		Carbonate	1	Pale, fine-grained patches (<0.2 mm) filling microfractures and small interstitial pockets.
Quartz		Quartz	2	Anhedral grains (~0.2–1 mm) with undulose extinction, occurring as veinlet between plagioclase and amphibole.
Pyroxene		Pyroxene (relict)		Small, irregular remnants (~0.2–0.7 mm) with subdued relief; commonly enclosed within amphibole.
	60	Actinolite-Tremolite (15% (within pyroxene zone)	46	Pale green to grey-green prismatic to tabular crystals (~0.3–2.7 mm), forming elongate bundles and diffuse replacement fronts; grains locally bent or kinked.
		Chlorite	8	Light green, grey, low-interference masses (~0.2–1 mm) occupying cleavage traces and margins of amphibole and biotite.
		Talc	2	Anhedral grains (~0.2–1 mm) with undulose extinction, occurring interstitially between plagioclase and amphibole.
		Biotite	2	Brown to bronze flakes (~0.2–0.9 mm) with moderate pleochroism; intergrown with chlorite in mafic zones.
Sulfides	1	Pyrrhotite	1	Bronze-grey anhedral to subhedral grains (~0.05–0.6 mm), disseminated.
		Chalcopyrite	Tr	Yellow, anhedral grains (~0.05–0.3 mm), disseminated trace in groundmass.
Comment: Fine- to medium-grained varitextured gabbronorite. Plagioclase forms irregular anhedral to subhedral mosaics (~0.4–2.4 mm) displaying mild strain and localized sericite–carbonate alteration. Mafic domains (~0.3–2.7 mm) are dominated by actinolite–tremolite in elongate bundles to tabular and diffuse patches surrounding small relict pyroxene; chlorite, biotite and minor talc fill cleavage traces and margins. Quartz occurs in small anhedral veinlet. The sulfide assemblage is well developed, with pyrrhotite and chalcopyrite occurring as disseminated grained.				

Thin section: 22-712-001 Sample ID: UU22-102358		Drill hole:22-712		Depth: 501.00 m
Mineral (Interpreted Pre-alteration)	%	Mineral (actual)	%	Details
Plagioclase	45	Plagioclase	25	Light grey anhedral to subhedral grains (~0.4–2.4 mm), locally visible polysynthetic twinning; twinning is partly obscured by sericite–chlorite alteration along fractures and grain boundaries, which are in places indistinct.
		Sericite	10	Fine-grained (<0.1 mm) replacing plagioclase along fractures, cleavage traces and grain margins, forming diffuse, patchy replacement zones.
Pyroxene	52	Pyroxene (relict)	6	Discontinuous orthopyroxene/clinopyroxene cores (~0.3–1.2 mm) with irregular boundaries.
		Actinolite-Tremolite	45	Subhedral to anhedral grains replaced pseudomorphically by talc and pale to medium-green amphibole (actinolite–tremolite), forming bladed aggregates (~0.3–2 mm) aligned with internal fabric; grain margins locally overprinted by chlorite.
		Chlorite	8	Fine-grained, light-green low-interference masses (~0.2–1 mm) occurring along margins of plagioclase, pyroxene, amphibole and biotite, filling cleavage traces and forming diffuse alteration halos.
		Talc	4	Very pale, low-birefringence fibrous to platy aggregates (<0.3 mm) forming pseudomorphic replacements of pyroxene, concentrated along mafic grain margins and fractures in strongly altered zones.
Biotite	Tr	Biotite	Tr	Rare subhedral grains, brown to bronze flakes (~0.2–0.9 mm) with moderate pleochroism; intergrown with chlorite in mafic zones.
Sulfides	3	Pyrrhotite Chalcopyrite	2	Disseminated chalcopyrite and pyrrhotite. Anhedral grains, interstitial and locally clustered.
Comment: The thin section shows a fine- to medium-grained equigranular gabbronorite. Plagioclase forms light grey anhedral to subhedral grains (~0.4–2.4 mm) with locally preserved polysynthetic twinning, partly obscured by sericite–chlorite alteration along fractures and margins. Mafic domains contain discontinuous ortho- and clinopyroxene cores (~0.3–1.2 mm) replaced by talc and pale to medium-green actinolite–tremolite forming bladed pseudomorphic aggregates (~0.3–2 mm), with chlorite common along grain edges. Additional light-green low-interference masses (~0.2–1 mm) fill cleavage traces around silicates, forming diffuse alteration halos, while very pale fibrous to platy aggregates (<0.3 mm) replace pyroxene along fractures in strongly altered zones. Biotite occurs only as rare brown to bronze flakes (~0.2–0.9 mm). Sulfides consist of disseminated chalcopyrite and pyrrhotite as anhedral interstitial grains and small clusters.				

Thin section: 22-712-003 Sample ID: UU22-102466		Drill hole:22-712		Depth: 601.9 m
Mineral (Interpreted Pre-alteration)	%	Mineral (actual)	%	Details
Plagioclase	25	Plagioclase	15	Light grey anhedral to subhedral grains (~0.4–2.4 mm) packed granular mosaic, with uneven contacts, grain boundaries are locally obscured by sericite–chlorite alteration, and are interlock.
		Sericite	7	Fine-grained, (<0.1 mm) replacing plagioclase along fractures, and grain margins, forming diffuse, patchy replacement zones.
Pyroxene	65	Pyroxene (relict)	10	Discontinuous orthopyroxene/clinopyroxene cores (~0.3–1.2 mm) with irregular boundaries, few exolution lamellae of clinopyroxene.
		Actinolite/ tremolite	52	Pale green to grey-green subhedral to anhedral grains (~0.3–2.8 mm) forming elongate bundles and diffuse replacement fronts, locally bent or kinked, aligned with internal fabric, with chlorite overprinting grain margins.
		Chlorite	5	Forms rims around pyroxene and plagioclase. Intergrown with altered silicates. (~0.2–1 mm) Present along grain boundaries and fractures.
		Talc	3	Very pale, silky aggregates (<0.3 mm) replacing pyroxene and amphibole along cleavage planes and fractures.
Biotite	5	Biotite	3	Anhedral to subhedral grains (~0.2–0.6 mm), brown, weak pleochroism; interstitial.
Sulfides	5	Pyrrhotite Chalcopyrite Pentlandite	5	Disseminated chalcopyrite and pyrrhotite. Anhedral grains, interstitial and locally clustered.
Comment: The thin section shows a fine- to medium-grained equigranular mesogabbronorite with a packed granular mosaic of light grey anhedral to subhedral plagioclase (~0.4–2.4 mm), displaying uneven contacts and locally obscured grain boundaries due to sericite–chlorite alteration forming diffuse micaceous replacement zones. Mafic domains contain discontinuous ortho- and clinopyroxene cores (~0.3–1.2 mm) with irregular boundaries and minor exsolution lamellae, overprinted by pale green to grey-green actinolite–tremolite forming elongate, locally kinked bundles (~0.3–2.8 mm) aligned with internal fabric; chlorite is common along grain margins. Additional greenish low-interference masses (~0.2–1 mm) form rims around pyroxene and plagioclase and occur along fractures, intergrown with altered silicates. Very pale silky aggregates (<0.3 mm) replace pyroxene and amphibole along cleavage planes and fractures. Biotite appearing as anhedral to subhedral grains altered to chlorite in interstitial zones. Sulfides consist of disseminated chalcopyrite and pyrrhotite as anhedral interstitial grains and small clusters.				

Thin section: 22-712-005 Sample ID: UU22-102574		Drill hole:22-712		Depth: 700.1m
Mineral (Interpreted Pre-alteration)	%	Mineral (actual)	%	Details
Plagioclase	60	Plagioclase	55	Subhedral to anhedral grains (~0.1–3 mm) with polysynthetic twinning. Altered to sericite and chlorite along grain boundaries and fractures. Grain boundaries mostly preserved.
		Sericite	5	Replaces plagioclase along cleavage planes and fractures. Fine-grained, fibrous texture.
Pyroxene	35	Pyroxene (relict)	5	Discontinuous kernels (~0.3–1.0 mm) with subdued relief and irregular, partly tabular outlines.
		Actinolite-Tremolite	20	Pale to grey-green elongate bundles (~0.3–2.8 mm), locally bent or kinked, forming diffuse replacement fronts aligned with internal fabric.
		Chlorite	7	Forms rims around pyroxene and plagioclase. Intergrown with altered silicates. Present along grain boundaries and fractures.
		Talc	3	Pseudomorphic replacement of pyroxene. throughout the pyroxene grains. Common in strongly altered zones.
Oxide	Tr	Magnetite	Tr	Very fine-grained magnetite, interstitial. Sparse and not texturally dominant.
Sulfides	5	Pyrrhotite	3	Bronze-grey anhedral to subhedral grains (~0.05–0.6 mm), disseminated.
		Chalcopyrite	2	Yellow grains (~0.05–0.3 mm), disseminated and occurring along pyrrhotite margins.
		Pentlandite	1	Pale bronze blebs (<0.1 mm), cluster within pyrrhotite and chalcopyrite gains rims.
Comment: Plagioclase is visually dominant in this equigranular gabbronorite, with well-preserved twinned grains and moderate alteration. Pyroxene is present and weak altered altered and volumetrically subordinate. Sulfides are intergrown, with chalcopyrite and pyrrhotite forming coarse grains. Alteration minerals especially amphibole, chlorite, and sericite are pervasive and help define the fabric.				

Thin section: 22-712-013 Sample ID: UU22-102746		Drill hole:22-712		Depth: 858.89 m
Mineral (Interpreted Pre-alteration)	%	Mineral (actual)	%	Details
Plagioclase	73	Plagioclase	60	Subhedral to anhedral grains (~0.1–3.2 mm) with polysynthetic twinning. Subhedral to anhedral grains (~0.1–3.2 mm) with polysynthetic twinning. Altered to sericite within grain and fractures. Grain boundaries mostly preserved.
		Sericite	10	Fine-grained, (<0.1 mm) altered plagioclase within grain and fractures. forming diffuse replacement films.
Pyroxene	25	Pyroxene (relict)	5	Residual orthopyroxene/clinopyroxene kernels (~0.3–1.0 mm) with subdued relief and irregular outlines with tabular texture.
		Actinolite-Tremolite	15	Pale to grey-green subhedral to anhedral grains (~0.3–2.8 mm) forming elongate bundles and diffuse replacement fronts, locally bent or kinked and aligned with internal fabric, bordered or intergrown with chlorite along grain margins.
		Chlorite	8	Light green, low-interference masses (~0.2–1 mm) occupying cleavage traces and margins of amphibole and biotite..
Sulfides	2	Pyrrhotite Chalcopyrite Pentlandite	2	Disseminated pyrrhotite and chalcopyrite. Anhedral grains (~0.2mm), interstitial and locally clustered.
Comment: Varitextured leucogabbronorite, with subhedral to anhedral plagioclase (~0.1–3.2 mm) with polysynthetic twinning, locally altered to fine sericite along fractures and within grains, grain boundaries remain mostly preserved. Overprinted by pale to grey-green amphibole (~0.3–2.8 mm) forming elongate bundles and diffuse replacement fronts, locally bent or kinked and aligned with internal fabric, with chlorite rims or intergrowths along margins. Additional light-green, low-interference masses (~0.2–1 mm) occupy cleavage traces and margins of amphibole and biotite. Sulfides occur as disseminated anhedral pyrrhotite and chalcopyrite (~0.2 mm), interstitial and locally clustered.				

Thin section: 22-712-016 Sample ID: UU22-102766		Drill hole:22-712		Depth: 877.00 m
Mineral (Interpreted Pre-alteration)	%	Mineral (actual)	%	Details
Plagioclase	35	Plagioclase	35	Grey to light grey, subhedral to anhedral grains (~0.5–3 mm) with polysynthetic twinning; irregular grain boundaries; local undulose extinction; tightly interlocking mosaic; sericitized in zones.
		Sericite	3	Trace; fine-grained occurring on the plagioclase grain.
Pyroxene	60	Pyroxene and weak actinolite-Tremolite, talc	55	The crystalline margins, which predate alteration, are generally well-preserved, exhibiting an equidimensional morphology that ranges from subhedral to anhedral. Pyroxene is largely retained, although partially replaced by an alteration assemblage consisting of tremolite–actinolite ± talc ± chlorite. This assemblage is characterized by very fine- to fine-grained crystals, along with aggregates of very fine-grained talc.
		Chlorite	2	Associated with Plagioclase and Pyroxene; along grain rims.
Biotite	-	Biotie	Trace	Dark brown to black lamellae (~0.5–2 mm); elongate; locally aligned; internal cleavage and fractures.
Sulfides	5	Pyrrhotite, Pentlandite, Chalcopyrite	5	Disseminated; subhedral to anhedral grains and mostly dominant by pyrrhotite and chalcopyrite.
Comment: Medium-grained equigranular gabbronorite, dominated by pyroxenes, and mostly preserves the original texture. Pyroxene grains are weakly altered and partially replaced by actinolite–tremolite, with chlorite forming along grain boundaries and in contact zones with plagioclase. Sericite alteration is present within plagioclase domains. Sulfide phases include pyrrhotite, pentlandite, and chalcopyrite, occurring as disseminated grains with subhedral to anhedral shape and associated with trace of magnetite at the rims.				

Thin section: 22-712-017 Sample ID: UU22-102770		Drill hole:22-712		Depth: 881.57 m
Mineral (Interpreted Pre-alteration)	%	Mineral (actual)	%	Details
Plagioclase	60	Plagioclase	43	Grey to light grey, subhedral to anhedral grains (~0.3–3 mm) with polysynthetic twinning, irregular grain boundaries, local sericitization along fractures/margins; intercumulus patches in matrix.
		Sericite	10	Very fine micaceous films (<0.1 mm) along fractures and margins, forming diffuse replacement streaks.
Pyroxene	35	Pyroxene (relict)	5	Irregular subhedral to anhedral fragments (~0.3–1.5 mm), subdued relief, internal fracturing, locally embayed margins
		Actinolite-Tremolite	18	Pale to light-green subhedral to anhedral grains (~0.2–2.8 mm) with variable interference colors; internal fractures; irregular boundaries; elongate to silky aggregates replacing pyroxene along cleavage planes and fractures; diffuse pseudomorphic zones.
		Hornblende	5	Darker green to brownish amphibole (~0.5–1.8 mm) with moderate interference colors; irregular outlines; partial overgrowth around pyroxene relics.
		Talc	6	Weak patches occur beyond the pyroxenes and along fracture zones, occasionally accompanied by actinolite.
		Chlorite	8	Soft green, low-interference flakes (~0.2–1 mm) along grain margins and cleavage traces; diffuse halos around mafic grains.
Sulfides	5	Pyrrhotite	3	Pink to pink grey anhedral to subhedral grains (~0.2–0.8 mm), scattered or forming small clusters; interstitial or fracture-hosted.
		Pentlandite	Tr	Pale brown fine grained (~0.1–0.3 mm), anhedral, intergrowths with chalcopyrite.
		Chalcopyrite	2	Yellow, fine grained grains (~0.2–0.6 mm), intergrown with pyrrhotite margins and occupying small pockets, disseminated.
		Pyrite	Tr	Bright, high-reflectance subhedral grains (~0.2–0.7 mm), occur as small clusters within pyrrhotite grain.
Comment: The section shows a medium-grained norite composed of plagioclase and altered pyroxene. Plagioclase forms a tight mosaic of grey to light-grey grains with polysynthetic twinning, irregular boundaries, and fine sericite along fractures. Pyroxene relics are irregular and fractured, extensively replaced by pale to light-green actinolite–tremolite forming elongate to silky aggregates along cleavage planes, with darker amphibole locally overgrowing the remnants. Talc and chlorite occur along grain margins and cleavage traces, producing diffuse halos and fibrous replacement textures. Sulfides, including chalcopyrite and pyrrhotite, appear as disseminated subhedral to anhedral grains with minor fine intergrowths and bright reflective inclusions.				

Thin section: 22-712-025 Sample ID: UU22-102852		Drill hole:22-712		Depth: 958.12 m
Mineral (Interpreted Pre-alteration)	%	Mineral (actual)	%	Details
Plagioclase	70	Plagioclase	57	Grey to light-grey subhedral to anhedral grains (~0.5–5 mm) forming angular to subangular clasts; polysynthetic twinning; irregular boundaries; crosscutting by fractures.
		Sericite	7	Very fine (<0.1 mm) along fractures and margins, forming diffuse replacement streaks within clasts.
Quartz		Quartz	6	White grey to grey, fine to medium grains (~0.2–2.5 mm) anhedral to rounded, present fracture zones and in the groundmass.
Pyroxene	29	Pyroxene (relict)	7	Irregular, fractured subhedral to anhedral fragments (~0.3–1.5 mm) with subdued relief; locally embayed margins.
		Actinolite–Tremolite	15	Pale to light-green subhedral to anhedral grains (~0.2–2.5 mm) with variable interference colors; elongate to silky aggregates replacing pyroxene along cleavage planes and fractures; diffuse pseudomorphic zones.
		Talc	2	Very pale, silky aggregates (<0.3–0.5 mm) occupying fractures and cleavage traces.
		Chlorite	5	Grey-green, low-interference flakes (~0.2–1 mm) along grain margins and cleavage traces; diffuse halos around mafic clasts.
Sulfides	1	Pyrrhotite	1	Pink-grey euhedral to subhedral grains (~0.2–0.8 mm), Disseminated throughout.
Comment: Varitextured leucogabbronorite, consist by grey to light-grey subhedral to anhedral grains (~0.5–5 mm) form by angular to subangular clasts plagioclase with polysynthetic twinning, irregular boundaries, and crosscutting fractures lined by very fine films and anhedral to subhedral pyroxene. The groundmass contains white-grey to grey anhedral to rounded grains (~0.2–2.5 mm) quartz concentrated in fracture zones and interstitial areas. Mafic fragments appear as irregular, fractured grains (~0.3–1.5 mm) with subdued relief and locally embayed margins. Pale to light-green Actinolite–Tremolite (~0.2–2.5 mm) forms elongate to silky aggregates along cleavage planes and fractures, with very pale silky patches (<0.5 mm) and grey-green flakes (~0.2–1 mm) along margins and cleavage traces. Pink-grey subhedral to euhedral Pyrrhotite (~0.2–0.8 mm) are disseminated throughout.				

Thin section: 22-712-036 Sample ID: UU22-102976		Drill hole:22-712		Depth: 1070.13 m
Mineral (Interpreted Pre-alteration)	%	Mineral (actual)	%	Details
Plagioclase	60	Plagioclase	35	Grey to light-grey anhedral to subhedral grains (~0.3–3 mm); polysynthetic twinning; irregular boundaries; internal fractures; local undulose extinction
		Sericite	6	Very fine micaceous films (<0.1 mm) along fractures and margins; diffuse replacement streaks.
		Quartz	7	Grey to light-grey anhedral to subhedral grains (~0.3–3 mm); irregular boundaries; internal fractures; local undulose extinction; dispersed rounded to lenticular clear domains.
Pyroxene	37	Pyroxene (relict)	5	Irregular, fractured subhedral to anhedral fragments (~0.3–1.5 mm); subdued relief; locally embayed margins.
		Actinolite-Tremolite	30	Pale to light-green subhedral to anhedral grains (~0.2–3 mm); variable interference colors; elongate to silky aggregates replacing pyroxene along cleavage planes and fractures; diffuse pseudomorphic zones.
		Talc	2	Very pale, silky aggregates (<0.3–0.5 mm) occupying fractures and cleavage traces.
		Chlorite	12	Grey-green, low-interference flakes (~0.2–1 mm) along grain margins and cleavage traces; diffuse halos around mafic grains.
	3	Biotite	3	Dark brown to black lamellae (~0.5–2 mm); elongate; locally aligned; internal cleavage and fractures.
Sulfides		Pyrrhotite	Tr	Trace of very fine grained disseminated.
Comment: Medium- to coarse-grained norite composed of grey to light-grey anhedral to subhedral plagioclase (~0.3–3 mm), irregular boundaries, local undulose extinction, and very fine micaceous films along margins. Rounded to lenticular clear patches occur within some felsic grains. Mafic areas consist of irregular, fractured pyroxene fragments (~0.3–1.5 mm) with subdued relief and locally embayed margins, extensively replaced by pale to light-green actinolite–tremolite (~0.2–3 mm) forming elongate to silky aggregates along cleavage planes and fractures, with very pale silky patches (<0.5 mm) in internal traces. Grey-green chloritic flakes (~0.2–1 mm) occur along grain margins and cleavage traces, forming diffuse halos around mafic grains.				

Thin section: 22-712-039 Sample ID: UU22-103008		Drill hole:22-712		Depth: 1100 m
Mineral (Interpreted Pre-alteration)	%	Mineral (actual)	%	Details
Plagioclase	40	Plagioclase	20	Grey to white-grey anhedral to subhedral grains (~0.3–4 mm); irregular boundaries; internal fractures; local undulose extinction; scattered rounded to lenticular clear domains.
		Sericite	10	Very fine micaceous films (<0.1 mm) along fractures and margins; diffuse streaks.
Pyroxene	60	Pyroxene (relict)	5	Irregular, fractured subhedral to anhedral grains (~0.3–1.5 mm); subdued relief; locally embayed margins.
		Amphibole	45	Pale to medium green subhedral to anhedral grains (~0.3–3 mm); variable interference colors; elongate to fibrous aggregates along cleavage planes and fractures; diffuse pseudomorphic zones.
		Talc	4	Very pale silky aggregates (<0.5 mm) occupying fractures and cleavage.
		Chlorite	10	Grey-green low-interference flakes (~0.2–1 mm) along grain margins and cleavage traces; diffuse halos around mafic grains.
		Biotite	6	Dark brown to black lamellae (~0.5–2 mm); elongate; locally aligned; internal cleavage and fractures.
Sulfides		-	-	-
Comment: Equigranular gabbronorite, consist by grey to white-grey anhedral to subhedral grains (~0.3–4 mm) plagioclase, show irregular boundaries, internal fractures, local undulose extinction, and scattered rounded to lenticular clear domains, with very fine micaceous films (<0.1 mm) along fractures and margins forming diffuse streaks, mafic domains consist of irregular, fractured subhedral to anhedral grains (~0.3–1.5 mm) with subdued relief and locally embayed margins, largely replaced by pale to medium-green subhedral to anhedral aggregates (~0.3–3 mm) displaying variable interference colors and elongate to fibrous textures along cleavage planes and fractures, with very pale silky patches (<0.5 mm) occupying internal traces. Grey-green low-interference flakes (~0.2–1 mm) occur along grain margins and cleavage traces, forming diffuse halos around mafic grains. Dark brown to black lamellae (~0.5–2 mm) appear elongate, locally aligned, and show internal cleavage and fractures. No sulfides are observed				

Thin section: 22-712-044 Sample ID: UU22-103059		Drill hole:22-712		Depth: 1147.88 m
Mineral (Interpreted Pre-alteration)	%	Mineral (actual)	%	Details
Plagioclase	25	Plagioclase	15	Grey to white-grey anhedral to subhedral grains (~0.3–2 mm); irregular boundaries; internal fractures; moderate alteration to sericite; weak undulating extinction locally; scattered rounded to lenticular clear domains.
		Sericite	10	Very fine micaceous films (<0.1 mm) replacing plagioclase; fine-grained alteration; diffuse streaks.
Pyroxene	55	Pyroxene (relict)	5	Irregular, fractured subhedral to anhedral grains (~0.3–1.5 mm); subdued relief; locally embayed margins.
		Actinolite-Tremolite	42	Pale to medium-green subhedral to anhedral grains (~0.3–3 mm); variable interference colors; elongate to fibrous aggregates along cleavage planes and fractures; diffuse pseudomorphic zones.
		Talc	2	Very pale silky aggregates (<0.5 mm) occupying fractures and cleavage traces.
		Chlorite	6	Grey-green low-interference flakes (~0.2–1 mm) along grain margins and cleavage traces; diffuse halos around mafic grains.
Biotite	8	Biotite	8	Dark brown to black lamellae (~0.5–2 mm); elongate; locally aligned; internal cleavage and fractures.
Sulfides	10	Pyrrhotite	6	Bronze-grey anhedral to subhedral grains (~0.2–0.5 mm); disseminated and forming irregular clusters; locally intergrown with magnetite.
		Chalcopyrite	3	Yellow grains (~0.1–0.6 mm); disseminated and locally attached to pyrrhotite margins.
		Pentlandite	1	Pale brown anhedral specks (<0.2 mm); irregularly disseminated within sulfide clusters.
Oxides	2	Magnetite	2	Black subhedral to anhedral grains (~0.1–0.8 mm); disseminated and commonly intergrown with pyrrhotite.
Comment: Moderately altered mesogabbronorite with grey to white-grey plagioclase (~0.3–2 mm) showing irregular boundaries, fractures, moderate sericitization, weak undulose extinction, and scattered lenticular clear domains. Mafic grains (~0.3–1.5 mm) are irregular, fractured, and largely replaced by pale to medium-green fibrous aggregates (~0.3–3 mm) with very pale silky patches (<0.5 mm) along internal traces. Chlorite forms grey-green flakes (~0.2–1 mm) along margins and cleavage traces, while dark brown to black biotite lamellae (~0.5–2 mm) appear elongate and locally aligned. Sulfides include disseminated bronze-grey pyrrhotite (~0.2–0.5 mm), yellow chalcopyrite (~0.1–0.6 mm) along pyrrhotite margins, and pale brown pentlandite specks (<0.2 mm). Black oxide grains (~0.1–0.8 mm) occur disseminated and commonly intergrown with pyrrhotite.				

Thin section: 22-712-046 Sample ID: UU22-103078		Drill hole:22-712		Depth: 1164.86 m
Mineral (Interpreted Pre-alteration)	%	Mineral (actual)	%	Details
Plagioclase	55	Plagioclase	45	Grey to white-grey anhedral to subhedral grains (~0.3–3 mm) with polysynthetic twinning; moderately altered to sericite and chlorite; patchy extinction and scattered lenticular clear domains.
		Sericite	2	Fine-grained (<0.1 mm) inclusions and alteration rims within plagioclase, producing cloudy textures.
Pyroxene	37	Pyroxene (relict)	5	Irregular, fractured subhedral to anhedral grains (~0.3–1.5 mm) with low relief and locally embayed grain margins
		Tremolite-actinolite	30	Pale- to medium-green brown subhedral to anhedral grains (~0.3–3 mm) displaying variable interference colors, occurring as elongate to fibrous aggregates along cleavage planes and fractures, and forming diffuse pseudomorphic replacement zones.
		Talc	2	Very pale silky aggregates (<0.5 mm) occupying fractures and cleavage traces.
		Chlorite	8	Grey-green low-interference flakes (~0.2–1 mm) along grain margins and cleavage traces; diffuse halos around mafic grains.
Biotite	5	Biotite	5	Dark brown to black lamellae (~0.5–2 mm); elongate; locally aligned; internal cleavage and fractures.
Sulfides	3	Pyrrhotite	2	Pink grey to bronze-grey anhedral to subhedral grains (~0.2–0.6 mm); disseminated and forming irregular clusters.
		Chalcopyrite	1	Yellow metallic grains (~0.1–0.5 mm); disseminated and locally attached to pyrrhotite margins.
		Pyrite	Tr	Very finely disseminated interstitial anhedral to subhedral
Oxides	Tr	Magnetite	Tr	Grey to light grey, subhedral to anhedral grains (~0.1–0.8 mm) disseminated elongate crystals within silicate alteration aggregates.

Comment: Weakly to moderately altered equigabbronorite composed of grey to white-grey anhedral to subhedral plagioclase (~0.3–3 mm) with polysynthetic twinning, sericite–chlorite alteration, patchy extinction, cloudy fine-grained inclusions, and scattered lenticular clear domains. Mafic grains (~0.3–1.5 mm) are irregular, fractured, low-relief and locally embayed, fully replaced by pale- to medium-green elongate to fibrous aggregates (~0.3–3 mm) forming diffuse pseudomorphic zones with very pale silky patches (<0.5 mm) along fractures. Grey-green chlorite flakes (~0.2–1 mm) occur along margins and cleavage traces, while dark brown to black biotite lamellae (~0.5–2 mm) appear elongate and locally aligned. Sulfides include pink-grey to bronze-grey anhedral to subhedral grains (~0.2–0.6 mm) forming small clusters, yellow metallic grains (~0.1–0.5 mm) attached to sulfide margins, and very fine interstitial disseminations. Grey to light-grey subhedral to anhedral oxide grains (~0.1–0.8 mm) occur disseminated within silicate alteration aggregates.

Thin section: 22-712-048 Sample ID: UU22-103095		Drill hole:22-712		Depth: 1180.29 m
Mineral (Interpreted Pre-alteration)	%	Mineral (actual)	%	Details
Plagioclase	55	Plagioclase	40	Grey to white-grey subhedral to anhedral grains (0.3–3 mm), showing polysynthetic twinning and moderate fracturing; variably altered to sericite.
		Sericite	7	Fine grained (<0.1 mm) inclusions within plagioclase and along fractures, producing a cloudy texture; secondary phase related to late alteration
Pyroxene	43	Pyroxene (relict)	4	Irregular, fractured subhedral to anhedral grains (~0.3–1.5 mm); subdued relief; locally embayed margins.
		Actinolite-Tremolite	30	Original pyroxenes largely replaced by tremolite–actinolite aggregates forming fibrous to bladed textures; alteration locally intense with chlorite and opaque mineral inclusions.
		Chlorite	8	Grey-green low-interference flakes (~0.2–1 mm) replacing amphibole and occurring along cleavage planes and grain boundaries.
Biotite			10	Dark brown to black lamellae (~0.5–2 mm); elongate; locally aligned; internal cleavage and fractures.
Sulfides	2	Pyrrhotite Chalcopyrite	1	Disseminated fine grains (0.02–0.3 mm) scattered throughout altered domains and along microfractures, light pink color dominant of sulfides in reflected light, show the dominance of pyrrhotite.

Comment: Moderately altered leucogabbronorite composed of grey to white-grey subhedral to anhedral plagioclase (0.3–3 mm) with polysynthetic twinning, moderate fracturing, sericite alteration, and fine (<0.1 mm) inclusions producing cloudy textures. Mafic grains (~0.3–1.5 mm) are irregular, fractured, low-relief and locally embayed, with original pyroxenes largely replaced by pale to medium tremolite–actinolite forming fibrous to bladed aggregates containing chlorite and opaque inclusions. Grey-green low-interference chlorite flakes (~0.2–1 mm) occur along cleavage planes and grain boundaries, while dark brown to black biotite lamellae (~0.5–2 mm) appear elongate, locally aligned, and show internal cleavage. Fine disseminated sulfides (0.02–0.3 mm), light pink in reflected light and dominated by pyrrhotite, occur within altered domains and along microfractures, with sparse associated phases along late fractures.

Thin section: 22-712-050 Sample ID: UU22-103110		Drill hole:22-712		Depth: 1193.00 m
Mineral (Interpreted Pre-alteration)	%	Mineral (actual)	%	Details
Plagioclase	50	Plagioclase	35	Grey to white-grey subhedral to anhedral grains (0.5–3 mm) showing polysynthetic twinning; moderately fractured and partly saussuritized; altered to sericite and chlorite, giving cloudy extinction and diffuse grain boundaries.
		Sericite	10	Fine-grained (<0.1 mm) forming rims and diffuse inclusions within feldspar; locally associated with weak carbonate alteration.
Pyroxene	42	Pyroxene (relict)	5	Irregular, fractured subhedral to anhedral grains (~0.3–1.5 mm); subdued relief; locally embayed margins.
		Actinolite-Tremolite	30	Pale to medium-green subhedral to anhedral grains (~0.3–3 mm); variable interference colors; elongate to fibrous aggregates along cleavage planes and fractures; diffuse pseudomorphic zones.
		Talc	2	Very pale silky aggregates (<0.5 mm) occupying fractures and cleavage traces.
		Chlorite	10	Secondary greenish phase replacing amphibole and forming interstitial patches; locally intergrown with tremolite; contributes to schistose texture.
Biotite	2	Biotite	2	Dark brown to black lamellae (~0.5–2 mm); elongate; locally aligned; internal cleavage and fractures.
Oxides	2	Magnetite	2	Grey, subhedral to anhedral grains (~0.1–0.8 mm); disseminated and commonly intergrown with pyrrhotite.
Sulfides	4	Pyrrhotite	3	Bright disseminated grains (0.02–0.5 mm) concentrated along microfractures and intergranular spaces, locally intergrown with magnetite.
		Chalcopyrite	1	Yellow metallic grains (~0.1–0.5 mm); disseminated and locally attached to pyrrhotite margins.
		Pentlandite	Tr	Pale brown anhedral specks (<0.2 mm); irregularly disseminated within sulfide clusters.
Comment: Moderately to strongly altered varitextured gabbronorite consist by g rey to white-grey subhedral to anhedral plagioclase (0.5–3 mm) with polysynthetic twinning, moderate fracturing, diffuse sericite–chlorite alteration, cloudy fine-grained (<0.1 mm) rims and inclusions, and weak carbonate patches. Mafic grains (~0.3–1.5 mm) are irregular, fractured, low-relief and locally embayed, with primary pyroxene almost entirely replaced by pale to medium-green tremolite–actinolite forming elongate to fibrous pseudomorphic zones and very pale silky aggregates (<0.5 mm) along fractures. A secondary greenish phase replaces amphibole and forms interstitial patches. Dark brown to black biotite lamellae (~0.5–2 mm) are elongate and locally aligned. Opaques include grey subhedral to anhedral grains magnetite (~0.1–0.8 mm) intergrown with pink to pink grey disseminated pyrrhotite, grains (0.02–0.5 mm) along microfractures, yellow metallic pyrrhotite grains (~0.1–0.5 mm) on margins, and pale brown specks pentlandite (<0.2 mm) within sulfide clusters.				

Thin section: 22-712-055 Sample ID: UU22-103142		Drill hole:22-712		Depth: 1223.9 m
Mineral (Interpreted Pre-alteration)	%	Mineral (actual)	%	Details
Plagioclase	40	Plagioclase	25	Anhedral to subhedral grains (0.5–3 mm) with polysynthetic twinning; variably saussuritized and partly replaced by sericite and chlorite; cloudy extinction and diffuse grain boundaries common.
		Sericite	10	Fine alteration of plagioclase forming cloudy inclusions and partial rims; locally associated with epidote and minor carbonate.
Pyroxene	45	Pyroxene (relict)	5	Irregular, fractured subhedral to anhedral grains (~0.3–1.5 mm); subdued relief; locally embayed margins.
		Actinolite-Tremolite	35	Pale to medium-green subhedral to anhedral grains (~0.3–3 mm) forming elongate to fibrous aggregates with variable interference colors, occurring along cleavage planes and fractures in diffuse pseudomorphic zones. Primary pyroxene is completely replaced by fibrous to bladed tremolite–actinolite forming radiating clusters and coarse intergrowths that define a weak foliation, with occasional relict pyroxene cores preserved.
		Talc	1	Very pale silky aggregates (<0.5 mm) occupying fractures and cleavage traces.
		Chlorite	9	Grey-green low-interference flakes (~0.2–1 mm) along grain margins and cleavage traces; diffuse halos around mafic grains.
Biotite	2	Biotite	2	Dark brown to brown grained ,elongate (~0.5–2 mm); locally aligned; internal cleavage and fractures.
Magnetite	1	Magnetite	1	Grey, subhedral to anhedral grains (0.1–0.5 mm) commonly intergrown with amphiboles and sulfides; locally forming small aggregates.
Sulfides	12	Pyrrhotite	8	bronze to brownish, irregular anhedral to locally subhedral grains, commonly forming interstitial patches and locally semi-massive aggregates within the silicate matrix, typically show fractured interiors and embayed margins. Hosts fine inclusions and exsolution textures of pentlandite and is locally replaced along grain boundaries and fractures by chalcopyrite
		Chalcopyrite	3	Yellow metallic grains occur as subordinate anhedral grains and irregular patches, commonly located along the margins of pyrrhotite or filling fractures and interstices between sulfide grains. Locally forms replacement textures against pyrrhotite. It

				rarely occurs as isolated grains and is typically associated with altered silicate domains
		pentlandite	1	bright cream-yellow, minor but significant inclusions within pyrrhotite, occurring as fine blebs, flame-like exsolution lamellae, or small subhedral grains along fractures and grain boundaries.
Comment: Moderated to strongly altered varitextured gabbronorite, consist of anhedral to subhedral plagioclase (0.5–3 mm) with polysynthetic twinning, diffuse sericite–chlorite replacement, cloudy extinction, and fine (<0.1 mm) inclusions and partial rims locally associated with minor carbonate. Mafic grains (~0.3–1.5 mm) are irregular, fractured, low-relief and locally embayed, with primary pyroxene completely replaced by pale to medium-green tremolite–actinolite forming elongate to fibrous pseudomorphic aggregates, radiating clusters, and coarse intergrowths defining a weak foliation; rare relict pyroxene cores persist. Very pale silky aggregates (<0.5 mm) occupy fractures, while grey-green chlorite flakes (~0.2–1 mm) occur along margins and cleavage traces. Dark brown to brown elongate lamellae (~0.5–2 mm) are locally aligned with internal cleavage. Opaque phases include grey subhedral to anhedral grains (0.1–0.5 mm) intergrown with amphibole and sulfides, and bronze to brownish anhedral to subhedral pyrrhotite forming interstitial to semi-massive patches with fractured interiors, embayed margins, fine pentlandite inclusions, and local chalcopyrite replacement. Yellow metallic grains (~0.1–0.5 mm) occur along pyrrhotite margins and within fractures, while bright cream-yellow pentlandite blebs and flame-like exsolution appear as minor inclusions along grain boundaries.				

Thin section: 22-712-061 Sample ID: UU22-103210		Drill hole:22-712		Depth: 1286.08 m
Mineral (Interpreted Pre-alteration)	%	Mineral (actual)	%	Details
Plagioclase	45	Plagioclase	30	Grey to white-grey anhedral to subhedral grains (~0.4–3 mm); irregular boundaries; internal fractures; weak to moderate undulose extinction; scattered lenticular clear domains, polysynthetic twinning.
		Sericite	6	Very fine micaceous films (<0.1 mm) along fractures and margins; diffuse streaks; cloudy alteration patches.
Quartz	5	Quartz	5	Anhedral to rouynded (0.1–3 mm), grey to light grey; interstitial between plagioclase and amphibole; weak undulose extinction.
Pyroxene	35	Pyroxene (relict)	5	Irregular, fractured subhedral to anhedral grains (~0.3–1.5 mm); subdued relief; locally embayed margins.
		Actinolite-Tremolite	30	Pale to medium-green subhedral to anhedral grains (~0.3–3 mm); variable interference colors; elongate to fibrous aggregates along cleavage planes and fractures; diffuse pseudomorphic zones.
		Chlorite	10	Grey-green low-interference flakes (~0.2–1 mm) along grain margins and cleavage traces; diffuse halos around mafic grains.
Biotite	3	Biotite	2	Brown, Subhedral to anhedral (~0.2–0.9 mm) with moderate pleochroism; locally aligned; internal cleavage and fractures.
Oxides	2	Magnetite	2	Grey, disseminated opaque grains; locally intergrown with sulfides.
Sulfides	10	Pyrrhotite	6	Medium grey, Irregular anhedral to locally subhedral grains; disseminated interstitial patches and connected aggregates; fractured and embayed.
		chalcopyrite	3	Anhedral interstitial patches; rims and replaces pyrrhotite along margins and fractures.
		Pentlandite	1	Bright cream-yellow, Fine blebs and flame-like exsolution lamellae within pyrrhotite; along fractures and grain boundaries.
		Pyrite	Tr	Bright white, small isolated anhedral to subhedral grains; interstitial to altered silicates.
Comment: Moderately altered varitextured leucogabbronorite with grey to white-grey plagioclase (~0.4–3 mm) showing polysynthetic twinning, fractures, cloudy sericite–epidote alteration, and fine micaceous films. Interstitial grey to light-grey anhedral grains (0.1–3 mm) occur between plagioclase and amphibole. Mafic grains (~0.3–1.5 mm) are irregular and fractured, with pyroxene fully replaced by pale to medium-green tremolite–actinolite forming elongate to fibrous pseudomorphic aggregates. Chlorite (~0.2–1 mm) lines margins and cleavage traces, and brown pleochroic lamellae (~0.2–0.9 mm) occur locally aligned. Opaques include grey disseminated grains, medium-grey fractured interstitial patches, and bright white isolated grains. Sulfides consist of anhedral pyrrhotite with fractured interiors and embayed margins, locally rimmed or replaced, containing bright cream-yellow blebs and flame-like exsolution lamellae, with subordinate yellow grains along margins and fractures.				

Appendix II

Whole-rock Geochemistry data

Sample No	Depth	SiO_2_pct	Al_2O_3_pct	Fe_2O_3_pct	CaO_pct	MgO_pct
22-711-001	905	50.3	21.1	5.54	10.7	7.41
22-711-005	951.44	43	13.9	19.25	11.15	6.62
22-711-010	1014.7	49.6	15.85	9.86	8.28	9.68
22-711-015	1040	49.3	15.3	8.26	9.38	11.4
22-711-022	1068	50.1	16.95	7.8	9.78	9.38
22-711-024	1095	49.2	15.95	7.95	9.01	11.75
22-711-029	1140	48.4	13.15	12.8	8.82	11.15
22-711-031	1157	48.7	17.15	8.45	9.39	9.94
22-711-032	1165	51.8	10.35	11.2	7.09	14.25
22-711-037	1215	49.9	14.2	11	9.38	10.4
22-711-041	1249	49.4	15.4	8.94	7.92	11.85
22-711-045	1279	49.7	17.85	8.15	9.35	9.21
22-711-048	1308	49.6	22	5.17	11.3	6.92
22-711-055	1368	51.3	16.45	9.68	9.66	9.54
22-712-001	501	50.9	11.25	10.25	6.86	14.8
22-712-003	600	49.8	6.41	15.6	8.53	14.05
22-712-005	700	50.9	16.4	8.48	9.23	11.8
22-712-013	858	44.7	19.5	5.23	10.3	7.31
22-712-016	877	51.5	10.5	13	6.69	17.35
22-712-017	881	49.2	14.25	10.95	7.39	12.5
22-712-025	958	54.2	19.75	5.77	9.72	6.39
22-712-036	1070	61.6	12.2	6.74	4.85	8.87
22-712-039	1100	49.6	10	10.45	5.96	16.95
22-712-044	1147	50.1	11.4	11.8	7.38	14.6
22-712-046	1164	51	17.75	7.06	9.52	10.15
22-712-048	1180	50.4	17.6	6.49	9.39	11.15
22-712-050	1193	50.1	14.2	9.83	8.5	12.6
22-712-055	1223	49.3	12.5	9.12	7.66	14.3
22-712-061	1286	54	16.6	6.65	8.42	7.77

Sample No	Na_2O_pct	K_2O_pct	Cr_2O_3_pct	TiO_2_pct	MnO_pct	P_2O_5_pct	SrO_pct
22-711-001	2.02	0.13	0.026	0.07	0.08	0.005	0.03
22-711-005	1.78	0.12	0.003	1.59	0.16	0.01	0.02
22-711-010	2.12	0.48	0.023	0.45	0.13	0.005	0.03
22-711-015	1.65	0.14	0.031	0.13	0.12	0.005	0.02
22-711-022	1.82	0.18	0.027	0.12	0.12	0.01	0.02
22-711-024	1.26	0.15	0.047	0.08	0.12	0.005	0.01
22-711-029	1.4	0.1	0.036	0.34	0.17	0.01	0.02
22-711-031	1.53	0.21	0.036	0.12	0.13	0.005	0.02
22-711-032	1.12	0.28	0.058	0.16	0.18	0.005	0.01
22-711-037	1.62	0.16	0.032	0.3	0.16	0.02	0.01
22-711-041	1.58	0.34	0.044	0.1	0.14	0.005	0.02
22-711-045	1.84	0.25	0.031	0.1	0.11	0.01	0.03
22-711-048	2.28	0.34	0.022	0.08	0.08	0.01	0.03
22-711-055	2.1	0.47	0.03	0.19	0.14	0.01	0.02
22-712-001	1.24	0.34	0.041	0.13	0.17	0.005	0.01
22-712-003	0.38	0.08	0.048	0.3	0.24	0.04	0.005
22-712-005	1.68	0.28	0.044	0.13	0.14	0.01	0.02
22-712-013	1.82	0.19	0.027	0.06	0.08	0.005	0.02
22-712-016	0.93	0.13	0.058	0.14	0.19	0.01	0.01
22-712-017	1.35	0.23	0.043	0.12	0.16	0.005	0.02
22-712-025	2.65	0.7	0.01	0.1	0.09	0.02	0.03
22-712-036	2.62	0.33	0.036	0.15	0.1	0.01	0.03
22-712-039	0.71	0.47	0.073	0.15	0.17	0.01	0.01
22-712-044	0.91	0.09	0.052	0.16	0.19	0.01	0.01
22-712-046	2.06	0.11	0.028	0.11	0.11	0.01	0.02
22-712-048	1.72	0.2	0.046	0.08	0.11	0.01	0.02
22-712-050	1.33	0.31	0.04	0.14	0.14	0.01	0.01
22-712-055	1.14	0.29	0.075	0.1	0.15	0.01	0.01
22-712-061	2.35	0.55	0.034	0.14	0.1	0.01	0.02

Sample No	BaO_pct	LOI_pct	Total_%_TOT	C_pct	S_pct	Ba_ppm	Ce_ppm
22-711-001	0.005	2.09	99.5	0.05	0.08	44.2	1.6
22-711-005	0.01	1.18	98.79	0.16	0.62	41.4	3.8
22-711-010	0.01	3.08	99.59	0.05	0.39	72.1	1.8
22-711-015	0.005	2.52	98.25	0.15	0.07	38.7	1.6
22-711-022	0.01	3.16	99.48	0.16	0.15	47.3	1.9
22-711-024	0.005	3.45	98.98	0.06	0.16	38.6	1.9
22-711-029	0.005	2.05	98.45	0.17	0.52	35.7	1.6
22-711-031	0.01	3.21	98.9	0.12	0.31	56.1	2.1
22-711-032	0.01	1.75	98.26	0.16	0.31	68.6	3.8
22-711-037	0.01	1.96	99.15	0.19	0.17	48	4.7
22-711-041	0.01	2.87	98.61	0.09	0.42	124	2.9
22-711-045	0.01	2.44	99.08	0.08	0.47	57.1	2.1
22-711-048	0.01	2.55	100.39	0.08	0.16	55	2
22-711-055	0.01	2.15	101.75	0.03	0.44	73.2	2.7
22-712-001	0.01	3.82	99.82	0.16	0.08	51.5	1.8
22-712-003	0.005	3.31	98.79	0.13	0.33	15.4	6.6
22-712-005	0.005	1.92	101.03	0.16	0.07	48.4	2.4
22-712-013	0.005	1.97	91.21	0.1	0.1	34.9	1
22-712-016	0.005	0.93	101.44	0.16	0.43	27.4	1.6
22-712-017	0.005	3.79	100	0.07	0.5	43.4	1.6
22-712-025	0.01	2.23	101.67	0.06	0.03	128.5	6.7
22-712-036	0.02	2.93	100.49	0.04	0.06	169	9.4
22-712-039	0.01	4.16	98.72	0.19	0.03	86.4	2
22-712-044	0.005	3.02	99.72	0.05	0.68	26	3.4
22-712-046	0.005	2.83	100.76	0.04	0.22	40.2	1.6
22-712-048	0.005	3.08	100.3	0.04	0.08	49.5	1.3
22-712-050	0.01	3.72	100.94	0.04	0.42	45.7	1.4
22-712-055	0.005	4.13	98.79	0.04	0.29	41.5	1.8
22-712-061	0.02	2.35	99.01	0.06	0.2	160	8.5

Sample No	Cr_ppm	Cs_ppm	Dy_ppm	Er_ppm	Eu_ppm	Ga_ppm	Gd_ppm
22-711-001	206	1.52	0.21	0.13	0.17	13.6	0.18
22-711-005	31	0.77	1.18	0.74	0.35	19.6	1
22-711-010	189	4.01	0.36	0.22	0.17	13.8	0.29
22-711-015	238	1.52	0.41	0.24	0.16	12	0.29
22-711-022	211	1.67	0.32	0.25	0.16	13	0.31
22-711-024	369	1.61	0.32	0.21	0.11	10.2	0.18
22-711-029	290	0.46	0.44	0.42	0.19	12.8	0.4
22-711-031	292	2.17	0.41	0.24	0.16	11.8	0.4
22-711-032	455	1.57	0.44	0.28	0.12	9.8	0.35
22-711-037	253	1.05	0.56	0.45	0.25	13.1	0.69
22-711-041	343	2.63	0.24	0.2	0.07	11.6	0.22
22-711-045	234	1.52	0.33	0.2	0.16	12.6	0.17
22-711-048	175	3.63	0.25	0.17	0.18	13.9	0.23
22-711-055	230	4.5	0.44	0.34	0.18	13.7	0.33
22-712-001	306	2.49	0.49	0.34	0.16	9.9	0.36
22-712-003	359	1.29	1.16	0.75	0.31	9.9	1.21
22-712-005	335	1.33	0.42	0.27	0.16	10.4	0.32
22-712-013	187	0.91	0.2	0.13	0.13	9.8	0.12
22-712-016	440	1.09	0.36	0.32	0.06	8.5	0.27
22-712-017	330	2.51	0.3	0.18	0.11	11.2	0.25
22-712-025	76	4.01	0.43	0.22	0.18	13.1	0.36
22-712-036	262	2.15	0.32	0.24	0.19	10.4	0.29
22-712-039	547	5.33	0.46	0.35	0.18	7.6	0.4
22-712-044	387	1.35	0.6	0.37	0.17	8.4	0.46
22-712-046	212	1.31	0.34	0.17	0.14	12.6	0.27
22-712-048	368	2.17	0.28	0.15	0.1	10.8	0.19
22-712-050	293	3.62	0.32	0.24	0.13	10.2	0.32
22-712-055	554	3.12	0.33	0.2	0.14	8.6	0.24
22-712-061	252	3.62	0.49	0.32	0.23	12.3	0.54

Sample No	Ge_ppm	Hf_ppm	Ho_ppm	La_ppm	Lu_ppm	Nb_ppm	Nd_ppm
22-711-001	0.9	0.07	0.05	1	0.02	0.09	0.8
22-711-005	1.4	0.4	0.21	1.7	0.08	0.42	2.8
22-711-010	1.1	0.14	0.07	0.9	0.03	0.18	0.9
22-711-015	1.2	0.13	0.09	0.9	0.05	0.09	1
22-711-022	1	0.17	0.08	1	0.06	0.23	1.1
22-711-024	1	0.1	0.07	2	0.02	0.14	0.9
22-711-029	1.2	0.14	0.11	0.7	0.06	0.1	1
22-711-031	1	0.15	0.09	1.1	0.04	0.16	1.3
22-711-032	1.2	0.37	0.08	1.9	0.06	0.71	1.6
22-711-037	1.4	0.4	0.14	2	0.09	0.58	2.5
22-711-041	1.1	0.2	0.06	1.5	0.05	0.24	1.1
22-711-045	0.9	0.31	0.04	1.2	0.05	0.18	1
22-711-048	0.9	0.09	0.06	1.1	0.04	0.15	0.8
22-711-055	1.2	0.17	0.09	1.4	0.04	0.29	1.5
22-712-001	1.2	0.16	0.11	1	0.06	0.07	1.2
22-712-003	1.5	0.52	0.28	2.7	0.12	0.47	4
22-712-005	1.1	0.21	0.11	1.7	0.05	0.22	1
22-712-013	0.8	0.05	0.05	0.6	0.02	0.025	0.5
22-712-016	1.3	0.16	0.08	0.8	0.06	0.12	0.9
22-712-017	1	0.17	0.08	0.9	0.05	0.025	0.9
22-712-025	1	0.52	0.09	4	0.05	0.95	2.5
22-712-036	0.8	2.1	0.08	5.6	0.07	1.58	3
22-712-039	1.2	0.17	0.11	1.1	0.08	0.11	1.1
22-712-044	1.4	0.26	0.12	1.8	0.08	0.36	2
22-712-046	0.8	0.14	0.07	0.9	0.05	0.025	0.9
22-712-048	1	0.1	0.06	0.9	0.04	0.025	0.4
22-712-050	1.1	0.14	0.07	0.7	0.05	0.06	0.9
22-712-055	1.4	0.14	0.08	0.9	0.05	0.06	0.7
22-712-061	1	0.63	0.11	4.5	0.07	1.22	3.6

Sample No	Pr_ppm	Rb_ppm	Sm_ppm	Sn_ppm	Sr_ppm	Ta_ppm	Tb_ppm
22-711-001	0.15	3.7	0.25	0.25	272	0.05	0.03
22-711-005	0.6	1.9	0.84	0.25	196	0.05	0.17
22-711-010	0.25	18.2	0.36	0.25	258	0.05	0.05
22-711-015	0.21	2.6	0.24	0.25	187.5	0.05	0.05
22-711-022	0.26	4.5	0.23	0.25	206	0.05	0.06
22-711-024	0.2	3.5	0.26	0.25	156.5	0.05	0.04
22-711-029	0.2	1.6	0.35	0.25	170	0.05	0.09
22-711-031	0.24	5.9	0.21	0.25	209	0.05	0.04
22-711-032	0.44	7.7	0.4	0.25	113.5	0.05	0.07
22-711-037	0.64	3.5	0.6	0.25	183	0.05	0.1
22-711-041	0.3	10.6	0.24	0.25	199.5	0.05	0.05
22-711-045	0.24	8.2	0.2	0.25	229	0.05	0.03
22-711-048	0.23	13.7	0.28	0.25	261	0.05	0.05
22-711-055	0.33	14.8	0.24	0.25	210	0.05	0.07
22-712-001	0.21	13.3	0.22	0.25	148	0.05	0.08
22-712-003	0.94	1.6	1.09	0.25	35.9	0.05	0.19
22-712-005	0.26	8.6	0.3	0.25	204	0.05	0.04
22-712-013	0.08	5	0.05	0.25	211	0.05	0.02
22-712-016	0.19	2.9	0.23	0.25	113	0.05	0.04
22-712-017	0.17	9.7	0.21	0.5	202	0.05	0.05
22-712-025	0.77	24.6	0.35	0.6	254	0.1	0.07
22-712-036	0.95	10.2	0.48	0.25	310	0.1	0.06
22-712-039	0.22	16.4	0.31	0.25	86.6	0.05	0.06
22-712-044	0.38	2.6	0.37	0.25	99.9	0.05	0.09
22-712-046	0.21	3.4	0.2	0.25	225	0.05	0.04
22-712-048	0.13	8.1	0.19	0.25	213	0.05	0.04
22-712-050	0.16	12.1	0.24	0.25	152.5	0.05	0.06
22-712-055	0.19	11.2	0.23	0.25	127.5	0.05	0.05
22-712-061	0.93	18	0.69	0.25	213	0.1	0.09

Sample No	Th_ppm	Tm_ppm	U_ppm	V_ppm	W_ppm	Y_ppm	Yb_ppm
22-711-001	0.08	0.02	0.025	64	1.3	1.5	0.17
22-711-005	0.15	0.11	0.025	1030	1.1	5.9	0.65
22-711-010	0.08	0.03	0.025	297	1.8	2.1	0.23
22-711-015	0.06	0.03	0.025	115	0.7	2.4	0.29
22-711-022	0.09	0.04	0.025	113	0.9	2.1	0.32
22-711-024	0.08	0.04	0.025	142	0.9	1.8	0.2
22-711-029	0.05	0.06	0.025	290	0.9	3	0.35
22-711-031	0.14	0.04	0.025	115	0.9	2.2	0.33
22-711-032	0.38	0.05	0.1	153	0.6	2.5	0.41
22-711-037	0.29	0.08	0.11	206	0.8	4.2	0.45
22-711-041	0.17	0.03	0.07	100	0.7	1.9	0.26
22-711-045	0.13	0.03	0.06	96	1.1	1.6	0.25
22-711-048	0.08	0.03	0.025	67	0.7	1.5	0.2
22-711-055	0.22	0.06	0.14	145	1	3.1	0.39
22-712-001	0.05	0.06	0.025	115	0.25	3	0.39
22-712-003	0.31	0.13	0.33	208	0.6	7.3	0.85
22-712-005	0.14	0.05	0.34	111	0.6	2.9	0.33
22-712-013	0.025	0.02	0.07	55	0.6	1.1	0.12
22-712-016	0.07	0.05	0.025	142	0.25	2.2	0.36
22-712-017	0.08	0.04	0.025	127	0.5	2.1	0.26
22-712-025	4.82	0.04	0.92	77	0.8	2.6	0.31
22-712-036	1.3	0.04	0.48	82	0.7	2.2	0.34
22-712-039	0.13	0.06	0.025	128	1.1	3.1	0.39
22-712-044	0.21	0.07	0.05	142	0.8	3.9	0.39
22-712-046	0.06	0.03	0.025	90	0.7	1.9	0.25
22-712-048	0.025	0.03	0.025	86	0.9	1.8	0.19
22-712-050	0.06	0.05	0.025	119	0.8	2.3	0.32
22-712-055	0.06	0.03	0.05	103	0.6	1.9	0.26
22-712-061	1.24	0.05	0.3	93	0.6	3.3	0.3

Sample No	Zr_ppm	As_ppm	Bi_ppm	Hg_ppm	In_ppm	Re_ppm	Sb_ppm
22-711-001	2	0.1	0.03	0.0025	0.0025	0.0005	0.025
22-711-005	12	0.2	0.08	0.0025	0.007	0.003	0.025
22-711-010	5	0.1	0.15	0.0025	0.0025	0.0005	0.025
22-711-015	5	0.1	0.03	0.0025	0.0025	0.0005	0.025
22-711-022	6	0.05	0.4	0.0025	0.0025	0.0005	0.025
22-711-024	4	0.5	0.08	0.0025	0.005	0.001	0.05
22-711-029	5	0.7	0.11	0.0025	0.009	0.002	0.22
22-711-031	5	0.8	0.32	0.005	0.009	0.001	0.11
22-711-032	16	0.2	0.11	0.0025	0.008	0.001	0.025
22-711-037	12	0.2	0.07	0.0025	0.007	0.0005	0.025
22-711-041	7	2.1	0.22	0.0025	0.012	0.002	0.13
22-711-045	16	0.2	0.19	0.0025	0.008	0.002	0.025
22-711-048	4	0.05	0.18	0.0025	0.0025	0.001	0.025
22-711-055	7	0.3	0.63	0.0025	0.007	0.001	0.025
22-712-001	5	0.2	0.03	0.0025	0.0025	0.0005	0.025
22-712-003	17	0.4	0.13	0.0025	0.007	0.001	0.025
22-712-005	9	0.3	0.02	0.0025	0.0025	0.0005	0.025
22-712-013	1	0.1	0.02	0.0025	0.0025	0.001	0.025
22-712-016	5	0.1	0.13	0.0025	0.008	0.002	0.025
22-712-017	5	0.2	0.16	0.0025	0.011	0.002	0.025
22-712-025	14	0.05	0.04	0.0025	0.0025	0.0005	0.025
22-712-036	80	0.1	0.56	0.0025	0.0025	0.0005	0.025
22-712-039	7	0.05	0.01	0.0025	0.0025	0.0005	0.025
22-712-044	8	0.3	0.19	0.0025	0.011	0.002	0.025
22-712-046	5	0.05	0.1	0.0025	0.0025	0.001	0.025
22-712-048	3	0.05	0.08	0.0025	0.0025	0.0005	0.025
22-712-050	4	0.05	0.22	0.0025	0.006	0.001	0.025
22-712-055	6	0.05	0.39	0.0025	0.005	0.001	0.025
22-712-061	22	0.1	0.1	0.0025	0.0025	0.0005	0.025

Sample No	Te_ppm	Tl_ppm	Ag_ppm	Cd_ppm	Co_ppm	Cu_ppm	Li_ppm
22-711-001	0.06	0.02	0.25	0.25	41	203	20
22-711-005	0.11	0.02	0.25	0.6	102	356	10
22-711-010	0.07	0.03	0.25	0.5	68	270	10
22-711-015	0.1	0.01	0.25	0.25	65	182	10
22-711-022	0.73	0.01	0.5	0.25	56	403	10
22-711-024	0.31	0.01	0.25	0.25	66	565	10
22-711-029	0.55	0.01	0.6	0.5	91	930	10
22-711-031	0.8	0.01	0.6	0.25	66	1050	10
22-711-032	1.16	0.04	0.5	0.25	93	1050	10
22-711-037	0.19	0.02	0.25	0.25	72	428	10
22-711-041	1.59	0.03	0.8	0.25	93	1565	10
22-711-045	0.87	0.06	0.9	0.25	74	1475	10
22-711-048	0.29	0.03	0.25	0.25	40	352	10
22-711-055	1.08	0.13	0.6	0.25	76	1035	10
22-712-001	0.04	0.03	0.25	0.25	78	214	10
22-712-003	0.12	0.03	0.25	0.6	96	339	10
22-712-005	0.07	0.02	0.25	0.25	61	223	10
22-712-013	0.08	0.02	0.25	0.25	41	339	10
22-712-016	1.88	0.03	0.7	0.25	108	1440	10
22-712-017	1.51	0.04	0.7	0.25	91	1590	10
22-712-025	0.03	0.04	0.25	0.25	40	97	10
22-712-036	0.13	0.02	0.25	0.25	47	89	10
22-712-039	0.03	0.03	0.25	0.25	78	67	10
22-712-044	0.98	0.03	0.8	0.25	100	1460	10
22-712-046	0.51	0.03	0.25	0.25	58	596	10
22-712-048	0.09	0.01	0.25	0.25	55	255	10
22-712-050	0.41	0.05	0.5	0.25	81	787	20
22-712-055	0.73	0.02	0.25	0.25	84	601	20
22-712-061	0.17	0.05	0.25	0.25	50	388	10

Sample No	Mo_ppm	Ni_ppm	Pb_ppm	Sc_ppm	Zn_ppm	Se_ppm	Recvd Wt._kg
22-711-001	0.5	315	1	12	37	0.428	0.12
22-711-005	0.5	384	2	51	92	1.075	0.1
22-711-010	0.5	330	1	20	57	0.927	0.15
22-711-015	0.5	441	1	22	54	0.373	0.12
22-711-022	0.5	399	1	20	53	0.698	0.13
22-711-024	0.5	751	1	19	47	1.525	2.21
22-711-029	0.5	933	3	32	65	2.75	2.25
22-711-031	0.5	845	1	18	47	2.12	0.1
22-711-032	0.5	1125	2	39	69	2.51	0.12
22-711-037	0.5	537	1	28	65	1.025	0.11
22-711-041	0.5	1545	3	19	66	4.59	0.11
22-711-045	0.5	1505	3	16	46	4.38	0.1
22-711-048	0.5	527	1	12	28	1.185	0.14
22-711-055	0.5	1170	4	23	58	3.13	0.12
22-712-001	0.5	475	1	27	71	0.418	0.13
22-712-003	0.5	579	2	51	115	1.245	2.12
22-712-005	0.5	478	1	23	53	0.473	0.14
22-712-013	0.5	448	1	15	30	0.733	0.11
22-712-016	0.5	1890	1	37	75	4.27	0.13
22-712-017	0.5	1740	1	18	65	4.28	0.1
22-712-025	1	166	1	17	34	0.101	0.11
22-712-036	0.5	292	1	20	45	0.201	1.99
22-712-039	0.5	509	1	36	71	0.175	2.26
22-712-044	0.5	1545	1	33	67	5.02	0.12
22-712-046	0.5	649	1	19	40	1.51	2.02
22-712-048	0.5	497	1	18	37	0.655	0.1
22-712-050	0.5	840	1	23	53	2.07	0.1
22-712-055	0.5	1100	1	30	54	2.27	1.98
22-712-061	0.5	517	1	18	41	1.22	0.11

Sample No	FeO*_pct	$Fe2O_3$*_pct
22-711-001	4.9849474	0.5550526
22-711-005	17.3213425	1.9286575
22-711-010	8.8721266	0.9878734
22-711-015	7.4324306	0.8275694
22-711-022	7.018518	0.781482
22-711-024	7.1534895	0.7965105
22-711-029	11.517568	1.282432
22-711-031	7.6033945	0.8466055
22-711-032	10.077872	1.122128
22-711-037	9.89791	1.10209
22-711-041	8.0443014	0.8956986
22-711-045	7.3334515	0.8165485
22-711-048	4.6520177	0.5179823
22-711-055	8.7101608	0.9698392
22-712-001	9.2230525	1.0269475
22-712-003	14.037036	1.562964
22-712-005	7.6303888	0.8496112
22-712-013	4.7060063	0.5239937
22-712-016	11.69753	1.30247
22-712-017	9.8529195	1.0970805
22-712-025	5.1919037	0.5780963
22-712-036	6.0647194	0.6752806
22-712-039	9.4030145	1.0469855
22-712-044	10.617758	1.182242
22-712-046	6.3526586	0.7073414
22-712-048	5.8397669	0.6502331
22-712-050	8.8451323	0.9848677
22-712-055	8.2062672	0.9137328
22-712-061	5.9837365	0.6662635

Appendix III

Geochronology

Fraction	Description	U (ppm)	Pb^T (Pg)	Pb_c (Pg)	Th/U	$^{206}Pb/^{204}Pb$
22-711-GC-001*						
Z1§	**1 clr, cls, el, partly fctd short pr**	174	219.16	5.12	0.83	2281
Z2†	**1 cls, skel, frag**	270	166.22	1.10	0.73	8125
Z3†	**1 clr, cls, skel, frag**	159	199.89	0.45	0.82	23372

Fraction	Description	$^{206}Pb/^{238}U$	±2σ	$^{207}Pb/^{235}U$	±2σ
22-711-GC-001*					
Z1§	**1 clr, cls, el, partly fctd short pr**	0.519035	0.000983	0.184136	0.000167
Z2†	**1 cls, skel, frag**	0.516121	0.001036	0.184148	0.000166
Z3†	**1 clr, cls, skel, frag**	0.518321	0.000969	0.184152	0.000145

Ages (Ma)						
Fraction	**Description**	$^{207}Pb/^{206}Pb$	±2σ	$^{207}Pb/^{235}U$	±2σ	$^{207}Pb/^{206}Pb$
22-711-GC-001*						
Z1§	**1 clr, cls, el, partly fctd short pr**	2695.1	4.2	2692.5	2.1	2690.5
Z2†	**1 cls, skel, frag**	2682.7	4.4	2687.2	2.3	2690.6
Z3†	**1 clr, cls, skel, frag**	2692.1	4.1	2691.2	2.2	2690.6

Ages (Ma)			
Fraction	**Description**	**±2σ**	**Disc(%)**
22-711-GC-001*			
Z1§	**1 clr, cls, el, partly fctd short pr**	1.5	-0.2
Z2†	**1 cls, skel, frag**	1.5	0.4
Z3†	**1 clr, cls, skel, frag**	1.3	-0.1

Notes:

All analyzed fractions represent best optical quality (crack-, inclusion-, core-free), fresh (least altered) grains of zircon. Zircons were chemically abraded (modified after Mattinson, 2005).

Abbreviations: Z - zircon; clr - clear; cls - colourless; el - elongate; fctd - faceted; pr - prism/prismatic; skel - skeletal; frag - fragment.

§ - spiked with EARTHTIME 535 (^{205}Pb-^{233}U-^{235}U) isotopic tracer; † - spiked with JSGL (ROM) ^{205}Pb-^{235}U isotopic tracer.

Pb^T is total amount (in picograms) of Pb.

Pb_C is total measured common Pb (in picograms) assuming the isotopic composition of laboratory blank: 206/204 - 18.49±0.4%; 207/204 - 15.59±0.4%; 208/204 - 39.36±0.4%

Pb/U atomic ratios are corrected for spike, fractionation, blank, and, where necessary, initial common Pb; ^{206}Pb/^{204}Pb is corrected for spike and fractionation.

Th/U is model value calculated from radiogenic ^{208}Pb/^{206}Pb ratio and ^{207}Pb/^{206}Pb age, assuming concordance.

Disc. (%) - per cent discordance for the given ^{207}Pb/^{206}Pb age.

Uranium decay constants are from Jaffey et al. (1971).

Appendix IV

Nd-Sm isotopes

Sample Number	**22-711-005**	**22-711-022**	**22-711-032**	**22-711-037**	**22-712-001**
From	951.71	1068.45	1165.65	1215.23	501.00
To	951.84	1068.61	1165.80	1215.39	501.2
AGE	2690.56	2690.56	2690.56	2690.56	2690.56
Nd (ppm)	2.7360914	1.1241550	1.5776772	2.8337335	1.1718889
^{143}Nd/^{144}Nd (current)	0.5124799	0.5118800	0.5114569	0.5117377	0.5120537
Sm (ppm)	0.8430939	0.2845789	0.3343800	0.6802295	0.3136332
^{147}Sm/^{144}Nd	0.1862916	0.1530468	0.1281357	0.1451257	0.1618019
^{143}Nd/^{144}Nd initial	0.5091728	0.5091632	0.5091823	0.5091614	0.5091814
143Nd/144Nd initial_2σ	0.0000343	0.0000287	0.0000247	0.0000274	0.0000302
Eps Nd (CHUR)T	0.5093804	0.3294234	0.7103156	0.2969196	0.6848676
Sample Number	**22-712-005**	**22-712-017**	**22-712-044**	**22-712-048**	**22-712-061**
From	700.1	881.47	1147.88	1223.9	1286.08
To	700.25	881.57	1148.00	1224	1286.19
AGE	2690.56	2690.56	2690.56	2690.56	2690.56
Nd (ppm)	0.9931794	0.7697837	1.8447770	0.5022112	2.9215336
^{143}Nd/^{144}Nd (current)	0.5118713	0.5118313	0.5117686	0.5118900	0.5111371
Sm (ppm)	0.2474429	0.1884763	0.4449394	0.1271349	0.5315949
^{147}Sm/^{144}Nd	0.1506244	0.1480253	0.1458159	0.1530475	0.1100064
^{143}Nd/^{144}Nd initial	0.5091974	0.5092036	0.5091801	0.5091731	0.5091843
^{143}Nd/^{144}Nd initial_2σ	0.0000283	0.0000279	0.0000275	0.0000287	0.0000218
Eps Nd (CHUR)T	1.0027012	1.1244711	0.6637557	0.5253096	0.7517871

Appendix V

CIPW normative calculation table, Mineral Comparative table, and photomicrographs for the least altered and most altered samples.

Sample no(LDI)	Sample Study no	CIPW-Rock type	Quartz (%Vol)	Orthoclase(%Vol)	Albite(%Vol)
UU22-101534	**22-711-001**	NOR	1.3	0.9	19.1
UU22-101650	**22-711-010**	Leuco-GBNR	0.0	3.4	20.7
UU22-101677	**22-711-015**	Meso-GBNR	0.0	1.0	16.3
UU22-101707	**22-711-022**	Meso-GBNR	0.8	1.3	17.7
UU22-101737	**22-711-024**	Meso-GBNR	0.4	1.1	12.5
UU22-101785	**22-711-02G**	Meso-GBNR	0.0	0.7	14.1
UU22-101804	**22-711-031**	Meso-GBNR	0.0	1.5	15.0
UU22-101813	**22-711-032**	Meso-GBNR	3.0	2.1	11.5
UU22-101866	**22-711-037**	Meso-GBNR	0.0	1.1	16.2
UU22-101904	**22-711-041**	NOR	0.0	2.4	15.6
UU22-101936	**22-711-045**	Leuco-GBNR	0.0	1.7	17.9
UU22-101968	**22-711-048**	Leuco-GBNR	0.0	2.3	21.3
UU22-102033	**22-711-055**	Meso-GBNR	0.0	3.3	20.4
UU22-102358	**22-712-001**	Meso-GBNR	0.5	2.5	12.7
UU22-102466	**22-712-003**	Mela-GBNR	3.4	0.6	4.0
UU22-102574	**22-712-005**	Meso-GBNR	0.0	2.0	16.5
UU22-102746	**22-712-013**	Leuco-GBNR	0.0	1.3	17.2
UU22-102766	**22-712-016**	Meso-GBNR	0.0	1.0	9.7
UU22-102770	**22-712-017**	NOR	0.0	1.7	13.6
UU22-102852	**22-712-025**	Leuco-GBNR	3.8	4.7	24.8
UU22-102976	**22-712-036**	NOR	19.4	2.2	24.9
UU22-103008	**22-712-039**	Meso-GBNR	0.0	3.5	7.4
UU22-103059	**22-712-044**	Meso-GBNR	0.7	0.7	9.4
UU22-103078	**22-712-046**	Leuco-GBNR	0.0	0.8	20.0
UU22-103095	**22-712-048**	Meso-GBNR	0.0	1.4	16.8
UU22-103110	**22-712-050**	Meso-GBNR	0.0	2.2	13.3
UU22-103142	**22-712-055**	Meso-GBNR	0.0	2.1	11.6
UU22-103210	**22-712-061**	Leuco-GBNR	6.4	3.7	22.3

Sample Study no	Anorthite(%Vol)	Diopside(%Vol)	Hypersthene(%Vol)	Olivine(%Vol)	Magnetite(%Vol)
22-711-001	51.1	3.6	20.9	0.0	0.5
22-711-010	35.6	6.6	25.1	4.1	0.8
22-711-015	37.5	9.5	27.9	2.7	0.7
22-711-022	41.0	8.1	26.6	0.0	0.7
22-711-024	41.6	5.5	33.7	0.0	0.7
22-711-02G	33.1	11.2	31.7	4.0	1.1
22-711-031	43.1	5.4	28.7	1.0	0.7
22-711-032	25.7	10.0	43.0	0.0	1.0
22-711-037	34.7	11.9	31.6	0.3	1.0
22-711-041	37.6	4.0	32.7	2.4	0.8
22-711-045	43.2	4.9	27.7	0.3	0.7
22-711-048	51.2	5.2	13.6	3.7	0.4
22-711-055	37.2	10.3	23.6	3.7	0.8
22-712-001	27.7	7.7	43.9	0.0	0.9
22-712-003	18.5	21.7	45.2	0.0	1.4
22-712-005	40.1	7.0	29.3	3.2	0.7
22-712-013	47.1	4.8	14.0	4.4	0.4
22-712-016	28.1	7.2	48.1	5.0	1.2
22-712-017	36.2	3.5	38.0	2.2	1.0
22-712-025	41.9	5.9	17.8	0.0	0.5
22-712-036	21.9	2.5	25.9	0.0	0.6
22-712-039	26.5	5.4	49.6	0.9	0.9
22-712-044	30.9	7.7	46.0	0.0	1.1
22-712-046	42.3	6.2	27.5	0.4	0.6
22-712-048	43.4	5.0	29.2	0.7	0.6
22-712-050	35.8	7.9	35.4	1.5	0.9
22-712-055	32.0	7.6	39.0	1.5	0.8
22-712-061	35.3	6.3	21.9	0.0	0.6

Sample Study no	Ilmenite(%Vol)	Apatite(%Vol)	Zircon(%Vol)	Plagioclase(%Vol)	Pyroxene(%Vol)
22-711-001	0.1	0.0	0.0	71.1	24.4
22-711-010	0.5	0.0	0.0	59.4	31.7
22-711-015	0.2	0.0	0.0	54.8	37.4
22-711-022	0.2	0.0	0.0	60.0	34.7
22-711-024	0.1	0.0	0.0	55.1	39.2
22-711-02G	0.4	0.0	0.0	48.0	43.0
22-711-031	0.2	0.0	0.0	59.6	34.2
22-711-032	0.2	0.0	0.0	39.2	53.0
22-711-037	0.4	0.1	0.0	52.0	43.5
22-711-041	0.1	0.0	0.0	56.0	36.7
22-711-045	0.1	0.0	0.0	63.0	32.7
22-711-048	0.1	0.0	0.0	75.0	18.8
22-711-055	0.2	0.0	0.0	60.9	33.9
22-712-001	0.2	0.0	0.0	42.8	51.6
22-712-003	0.4	0.1	0.0	23.2	66.9
22-712-005	0.2	0.0	0.0	58.6	36.4
22-712-013	0.1	0.0	0.0	65.6	18.8
22-712-016	0.2	0.0	0.0	38.7	55.3
22-712-017	0.2	0.0	0.0	51.4	41.4
22-712-025	0.1	0.0	0.0	71.4	23.6
22-712-036	0.2	0.0	0.0	49.0	28.4
22-712-039	0.2	0.0	0.0	37.4	55.0
22-712-044	0.2	0.0	0.0	41.0	53.7
22-712-046	0.1	0.0	0.0	63.1	33.7
22-712-048	0.1	0.0	0.0	61.6	34.3
22-712-050	0.2	0.0	0.0	51.3	43.3
22-712-055	0.1	0.0	0.0	45.6	46.5
22-712-061	0.2	0.0	0.0	61.4	28.1

Mineral / Phase	Observed % (22-712-016)	CIPW % (22-712-016)	Observed % (22-712-039)	CIPW % (22-712-039)
Alteration Level	Least altered	Least altered	Most altered	Most altered
Plagioclase	35.0	38.7	20.0	37.4
Sericite	3.0	–	10.0	–
Pyroxene (total)	55.0	55.3	5.0	55.0
Amphibole	Trace–minor	–	45.0	–
Talc	trace	–	4.0	–
Chlorite	2.0	–	10.0	–
Biotite	Trace	–	6.0	–
Olivine	–	5.0	–	0.9
Magnetite	Trace	1.2	Trace	1.1
Ilmenite	–	0.2	–	0.2
Sulfides	5.0	–	0.0	–
Quartz	–	0.0	–	0.0
Orthoclase	–	1.0	–	3.5
Albite	–	9.7	–	7.4
Anorthite	–	28.1	–	26.5
Diopside	–	7.2	–	5.4
Hypersthene	–	48.1	–	49.6
Ilmenite	–	0.2	–	0.2
Apatite	–	0.0	–	0.0
Zircon	–	0.0	–	0.0
LOI (%)	0.93	–	4.16	–

LOI values indicate significantly higher volatile content in the most altered sample (4.13%) compared to the least altered sample (1.96%).

Observed mineralogy includes secondary hydrous phases replacing primary pyroxene and plagioclase.

Normative minerals (CIPW) represent anhydrous, calculated primary mineral proportions and are listed in full to allow complete comparison between the two samples.

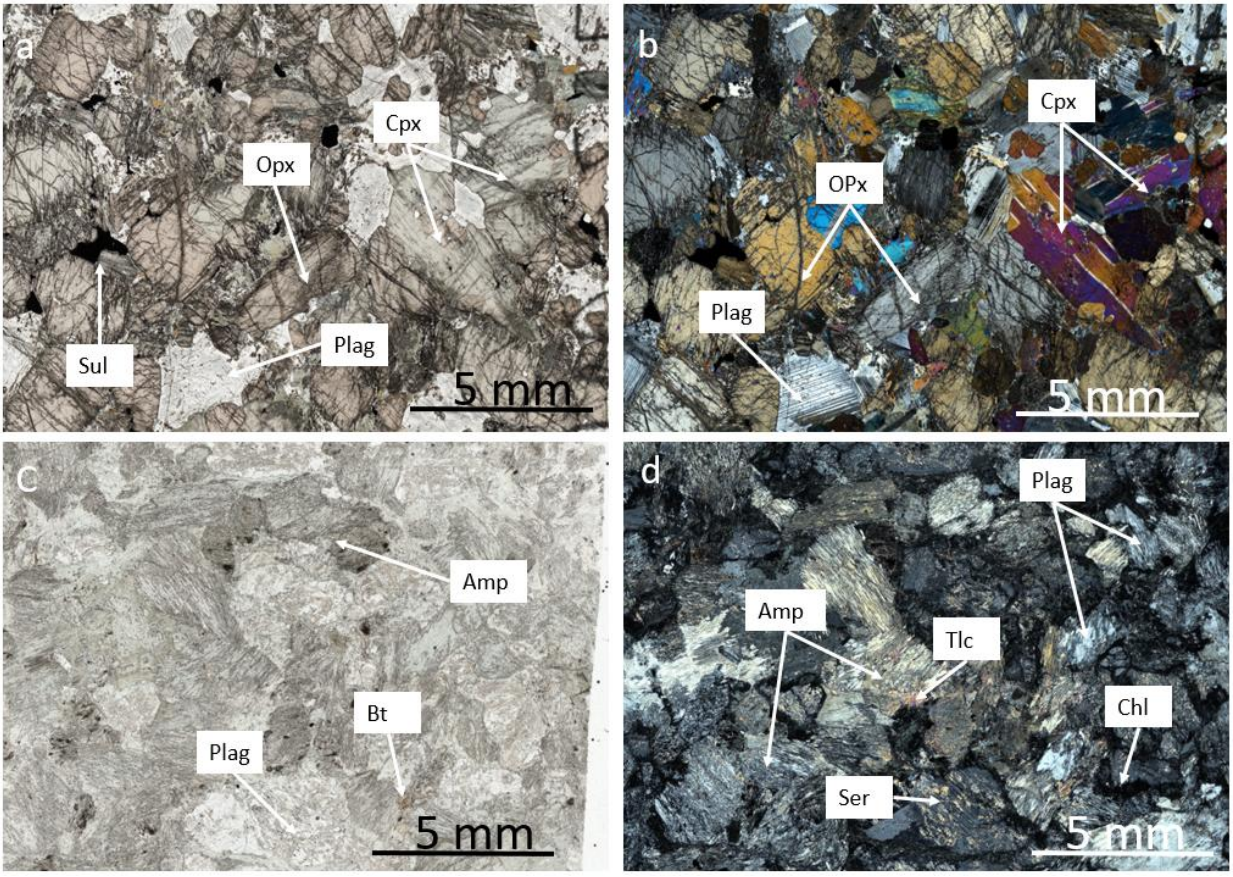

Comparative Photomicrographs (PPL and XPL) of Observed Mineralogy for Least and Most Altered Samples (22-712-016 and 22-712-039). Photomicrographs (a) and (b) show the least altered sample 22-712-016 in PPL and XPL, respectively, illustrating preserved orthopyroxene, clinopyroxene, plagioclase and disseminated sulfides, (c) and (d) show the most altered sample 22-712-039 in PPL and XPL, highlighting extensive replacement of primary pyroxenes by amphibole, sericite, chlorite and talc, with minor biotite and partially preserved plagioclase.